COMPARISON OF ML AND MAP PARAMETER ESTIMATION TECHNIQUES
FOR THE SOLUTION OF INVERSE ELECTROCARDIOGRAPHY PROBLEM

A THESIS SUBMITTED TO
THE GRADUATE SCHOOL OF NATURAL AND APPLIED SCIENCES
OF
MIDDLE EAST TECHNICAL UNIVERSITY

BY

TAHA ERENLER

IN PARTIAL FULFILLMENT OF THE REQUIREMENTS
FOR
THE DEGREE OF MASTER OF SCIENCE
IN
ELECTRICAL AND ELECTRONICS ENGINEERING

SEPTEMBER 2018

Approval of the thesis:

**COMPARISON OF ML AND MAP PARAMETER ESTIMATION
TECHNIQUES FOR THE SOLUTION OF INVERSE
ELECTROCARDIOGRAPHY PROBLEM**

submitted by **TAHA ERENLER** in partial fulfillment of the requirements for the degree of **Master of Science in Electrical and Electronics Engineering Department, Middle East Technical University** by,

Prof. Dr. Halil Kalıpçılar
Dean, Graduate School of **Natural and Applied Sciences**   _____

Prof. Dr. Tolga Çiloğlu
Head of Department, **Electrical and Electronics Engineering**   _____

Assoc. Prof. Dr. Yeşim Serinağaoğlu Doğrusöz
Supervisor, **Electrical and Electronics Eng. Dept., METU**   _____

Examining Committee Members:

Prof. Dr. Nevzat Güneri Gençer
Electrical and Electronics Engineering Department, METU   _____

Assoc. Prof. Dr. Yeşim Serinağaoğlu Doğrusöz
Electrical and Electronics Engineering Department, METU   _____

Prof. Dr. Murat Eyüboğlu
Electrical and Electronics Engineering Department, METU   _____

Prof. Dr. İlkay Ulusoy
Electrical and Electronics Engineering Department, METU   _____

Assist. Prof. Dr. Osman Serdar Gedik
Computer Engineering Department, AYBU   _____

                                          Date: **06/09/2018**

I hereby declare that all information in this document has been obtained and presented in accordance with academic rules and ethical conduct. I also declare that, as required by these rules and conduct, I have fully cited and referenced all material and results that are not original to this work.

Name, Last Name: TAHA ERENLER

Signature   :

ABSTRACT

**COMPARISON OF ML AND MAP PARAMETER ESTIMATION
TECHNIQUES FOR THE SOLUTION OF INVERSE
ELECTROCARDIOGRAPHY PROBLEM**

Erenler, Taha

M.S., Department of Electrical and Electronics Engineering

Supervisor　: Assoc. Prof. Dr. Yeşim Serinağaoğlu Doğrusöz

September 2018, 168 pages

This study aims to determine the cardiac electrical activity from body surface potential measurements. This problem is called the inverse problem of electrocardiography. Reconstruction of the cardiac electrical activity from the body surface potential measurements is not an easy task, since this problem has an ill-posed nature due to attenuation and spatial smoothing inside the medium between the source and the measurement sites, meaning that even small errors in the mathematical model or noise in the measurements may yield unbounded errors or large oscillations in the solutions. One remedy for this ill-posedness is to apply regularization, where one imposes deterministic or statistical constraints on the solution based on available a priori information. In this thesis, Tikhonov regularization, Bayesian maximum a posteriori estimation (BMAP), Kalman filter and regularized Kalman filter approaches are used to solve the inverse problem of electrocardiography. In the context of Kalman filter, maximum likelihood (ML) and maximum a posteriori (MAP) estimation are used to find Kalman filter parameters. By estimating Kalman filter parameters, we aim to find an answer to an open question of how the essential parameters in the state-

space representation are found without claiming strong assumptions in the literature. The results showed that the mean correlation coefficient ranges from 0.99 to 0.66 for MLIF and from 0.97 to 0.72 for MAPIF under 30 dB measurement noise. Our study showed that ML estimation works well when the training set data and test data are similar. However, due to over-fitting nature of the ML estimation, MAP estimation should be preferred in order to improve generalizability of the method.

ÖZ

TERS ELEKTROKARDİYOGRAFİ PROBLEMİNE UYGULANAN ML VE MAP PARAMETRE KESTİRİM METODLARININ KARŞILAŞTIRILMASI

Erenler, Taha

Yüksek Lisans, Elektrik ve Elektronik Mühendisliği Bölümü

Tez Yöneticisi   : Doç. Dr. Yeşim Serinağaoğlu Doğrusöz

Eylül 2018 , 168 sayfa

Bu çalışma, vücut yüzeyinden alınan potansiyel ölçümleri kullanarak kalpteki elektriksel aktivitenin bulunmasını amaçlamaktadır. Bu problem ters EKG problemi olarak adlandırılır. Ters EKG problemi, elektriksel sinyallerin, kalpteki elektriksel kaynaklar ve vücuttaki ölçüm noktaları arasında zayıflaması ve uzaysal düzleşme nedeniyle kötü konumlanmış bir doğaya sahiptir. Kötü konumlanma nedeniyle küçük matematiksel model hataları veya ölçümler sırasında oluşan gürültüler çözümlerde kontrolsüz hatalara veya büyük salınımlara sebep olur. Bu kötü konumlanmanın bir çözümü, probleme önsel bilgiler kullanılarak bazı deterministik veya istatiksel kısıtlamalar getirmek, yani düzenlileştirme uygulamaktır. Bu tezde çözüm yöntemleri olarak Tikhonov düzenlileştirmesi, Bayes en büyük sonsal kestrim, Kalman filtre ve düzenlileştirilmiş Kalman filtre uygulanmıştır. Kalman filtre yaklaşımının bir uzantısı olarak, ML ve MAP kestirim yöntemleri kullanılarak Kalman filtre parametreleri bulunmuştur. Kalman filtre parametrelerini tahmin ederek, durum uzayının oluşturulması için gerekli parametrelerin güçlü varsayımlar kullanılmadan nasıl bulunacağı konusundaki literatürde bulunan açık uçlu soruya yanıt vermeyi hedefledik. Elde ettiğimiz sonuçlar

ortalama ilinti katsayısının 30 dB SNR ölçüm hatası altında MLIF için 0.99 - 0.66 ve MAPIF için 0.97 - 0.72 arasında değiştiğini gösterdi. Çalışmalarımız ML kestirim yönteminin test verisi ile veri seti arasında güçlü benzerlik olduğu durumlarda iyi çalıştığını fakat ML kestirim yönteminin aşırı uyum gösterme doğası nedeniyle genelleştirilebilirlik için MAP kestirim yönetimini kullanmamızın daha iyi olacağını gösterdi.

Anahtar Kelimeler: Tersine elektrokardiyografi, Elektrokardiyografik görüntüleme, Kalman filtre, ML, MAP

To my family

ACKNOWLEDGMENTS

TABLE OF CONTENTS

LIST OF TABLES

LIST OF FIGURES

FIGURES

LIST OF ABBREVIATIONS

BEM   Boundary Element Method

CC   Correlation Coefficient

CT   Computerized Tomography

CVD   Cardiovascular Disease

ECG   Electrocardiography

ECGI   Electrocardiographic Imaging

EEG   Electroencephalography

FEM   Finite Element Method

LE   Localization Error

LSE   Least Squares Estimation

MAP   Maximum a *Posteriori*

MEG   Magnetoencephalography

ML   Maximum Likelihood

MRI   Magnetic Resonance Imaging

PDF   Probability Density Function

RDMS   Relative Difference Measurement Star

SVD   Singular Value Decomposition

TMP   Transmembrane Potential

TSVD   Truncated Singular Value Decomposition

CHAPTER 1

INTRODUCTION

1.1   Motivation of the Thesis

Cardiovascular diseases have been the primary cause of death for the last 15 years. In 2015, there were approximately 15 million deaths due to ischaemic heart disease and stroke [1]. Most of the time, these diseases are curable and deaths are avoidable if only they were detected. Cardiac source distributions, depolarization and repolarization times provide valuable information to detect and prevent the problems about the heart.

Today, in clinics, 12-lead ECG is the primary tool for the assessment of electrical activity of the heart. 12-lead ECG is very efficient, quick and patient friendly method. However, due to attenuation and smoothing within the body between the source and measurement locations, 12-lead ECG can not detect the actual location of the infarction and associated arrhythmias. Furthermore, 12-lead ECG does not measure cellular repolarization and depolarization directly, instead it measures cumulative change in cell membrane potentials [2]. Hence, the details of the electrophysiology of the cardiac cycle are lost. Another disadvantage of 12-lead ECG is that it does not provide cardiac activity directly, usually clinicians interpret the results of electrocardiography assuming that there is abnormality cardiac electrical field [3].

One alternative to 12-lead ECG is invasive electrocardiography. Invasive electrocardiography techniques may be used to increase the resolution but they are very impractical in patient's view point, so these methods are not preferable.

Another alternative approach to 12-lead ECG is electrocardiographic imaging (ECGI). The problem of finding cardiac electrical activity from the body surface potential

measurements is ill-posed. One way to combat this ill-posed nature of the problem is to apply regularization. In the literature, there are different regularization methods that were applied to the inverse electrocardiography problem. One method is Kalman filter. Kalman filter is widely used to solve inverse electrocardiography problem in literature. However, in the literature, there is an open question of how the parameters which are essential to use Kalman are found. In this study, we address this question and propose different methods to handle this issue. To estimate the Kalman filter parameters, we use maximum likelihood estimation and maximum a posteriori estimation and propose a constitute way to use Kalman filter method.

1.2 Scope of the Thesis

In this thesis, inverse problem of electrocardiography is formulated mathematically and six different solution approaches are applied to the problem. Spatial methods Tikhonov regularization and Bayesian maximum a posteriori estimation, and spatio-temporal method Kalman filter and smoother are used in this study. The parameters that are essential to apply Kalman filter are found by using Maximum likelihood (ML) and Maximum a posteriori (MAP) estimation. This study uses very few assumptions to construct the state-space representation of the problem. The solution approaches are compared with each other and, their robustness to measurement noise and geometric errors is evaluated.

1.3 Organization of the Thesis

This thesis is divided into five chapters:

- Chapter 2 covers the heart anatomy and physiology, cardiac electrical activity measurement techniques and the literature review on the forward and inverse electrocardiography.

- Chapter 3 covers the problem definition, inverse problem solution methods and parameter estimation techniques.

- Chapter 4 covers the application of algorithms given in theory section, along with the results and the discussions of these results.

- In Chapter 5, we conclude our work and give the future work.

CHAPTER 2

LITERATURE REVIEW AND BACKGROUND

In this chapter, heart anatomy, action potential generation and electrical activity of the heart are discussed. Then, measurement techniques of cardiac electrical activity are given. Finally, the literature survey on forward problem of electrocardiography and inverse problem of electrocardiography is given.

2.1 Heart Anatomy

The term "heart" is originated from Greek word "kardia". The heart is a vital organ which is located at mediastinum in thoracic cavity, between the lungs. The heart is isolated from the other tissues by pericardium. The weight of the heart is approximately between 250-350 grams. Figure 2.1 shows the heart in detail.

There are four chambers in the heart, each side of the heart has one ventricle and
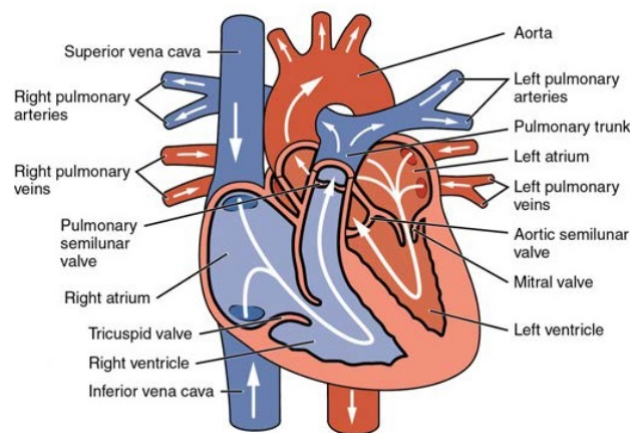
Figure 2.1: Anatomy of the heart [4]

one atrium. The right atrium and the left atrium receive blood and forward it to the right ventricle and the left ventricle [4]. The ventricles are working as pumps, they pump blood to the lungs and the body. Blood circulation system consists of two different circuits, namely pulmonary and systemic circuit. In the pulmonary circuit, deoxygenated blood is transferred from the right ventricle to the lungs and blood gets oxygen from the lungs. Then, oxygen rich blood is returned to the left atrium. In the systemic circuit, oxygen rich blood is pumped from the left ventricle to the body. The cells take oxygen and nutrients from the blood and the blood collects carbon dioxide and waste products from the cells. After that, deoxygenated blood is returned to the right atrium.

There are four layers in the heart wall as shown in Figure 2.2:
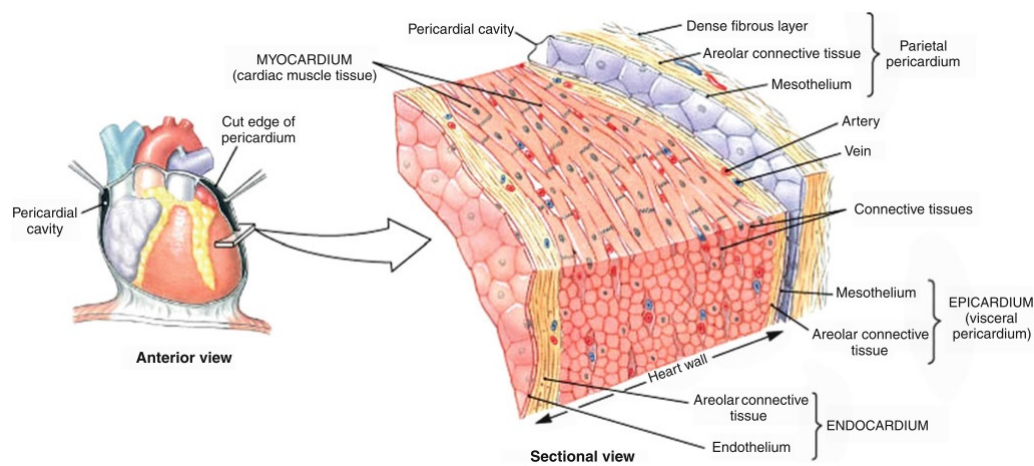
Figure 2.2: Layers of the heart [2]

- **Pericardium**: Pericardium or pericardial sac is the outer layer of the heart that surrounds and isolates the heart from the tissues.

- **Epicardium**: Epicardium is just under the pericardium and in contact with the surface of the heart. The electrical potentials on the epicardium are used as the equivalent cardiac source distribution in inverse and forward problem of electrocardiography.

- **Myocardium**: Myocardium is the middle layer of the heart. Myocardium is made of cardiac muscle and the thickest layer in the heart. This layer is responsible for pumping blood to the body.

- **Endocardium**: Endocardium is the innermost layer of the heart and composed of endothelial cells. This layer is very smooth and allows blood flow.

2.2 Action Potential Generation

Every cell has electrical potential across its membrane. This electrical potential is maintained by ionic concentration difference between inside and outside of the membrane. Most important ions that are contributing to establishment of the transmembrane potential are Na^+, K^+, Cl^-, Ca^{++}. The transmembrane potential, the potential difference across the cell membrane, is defined as:

$$V_m = V_e - V_i \qquad (2.1)$$

where V_e is extracellular potential and V_i is intracellular potential. In a typical cardiac cell, the resting transmembrane potential is -90 mV.

Some cells in the body are called as excitable cells and these type of cells are able to generate action potentials by changing their membrane permeability to certain ions. As seen in Figure 2.3, there are five phases in the action potential:

- Phase 4 is the duration when the cell is at resting potential. The heart is in diastole during this phase. When the cell is stimulated by an external stimulus, phase 4 ends. Some cells are able to depolarize repeatedly without the need of an external stimulus. These cells are called the pacemaker cells and located at the sinoatrial (SA) node.

- Phase 0 is the depolarization phase. A suprathreshold stimulus depolarizes the cell by activating the fast Na^+ channels. Due to inflow of the sodium ions, the transmembrane potential increases since the sodium ions are positively charged.

- Phase 1 is the duration when the fast Na^+ channels are closed and due to the outflow of some potassium and chloride ions, there is a small decrease in the action potential.

- Phase 2 is called the plateau phase. In this phase, there is a balance between the inflow of calcium ions and the outflow of the potassium ions. Hence, a constant action potential is maintained in this region.

- Phase 3 is the repolarization phase. In this phase, the fast calcium channels are closed and there is an outward current due to the movement of potassium ions. This outward current causes the action potential to decrease.
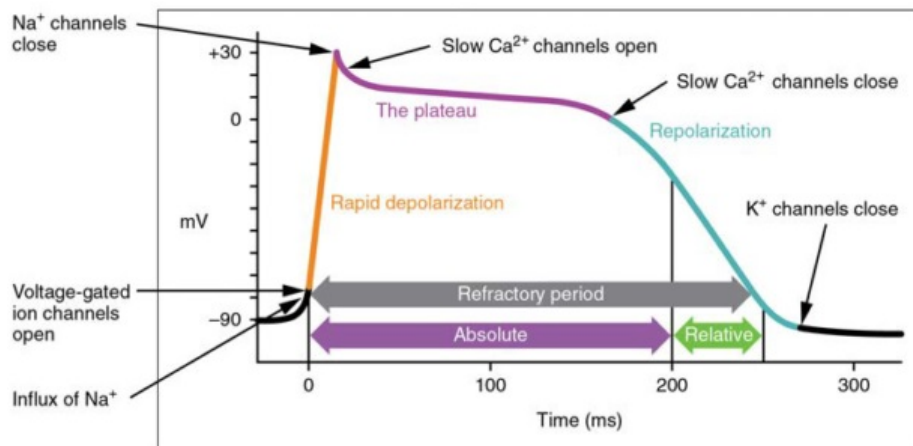
Figure 2.3: Action potential of a cardiac cell [4]

2.3   Electrical Activity of the Heart

In the heart, there are special cells that are adequate to generate their own electrical impulse innately. In cardiac conduction system, the electrical impulse is triggered by the cells who have the fastest inherent firing rate. The following parts of the heart play role in the cardiac conduction system:

- The sinoatrial (SA) node

- The atrioventricular node

- Bundle of his

- The atrioventricular bundle branches

- The Purkinje cells

Cardiac rhythm is initialized by the sinoatrial (SA) node. SA node is composed of myocardial cells and its location is in the right atrium posterior and superior walls. The SA node is called as pacemaker of the heart. Electrical signal initialized by the

8

SA node is transmitted to atriovenctricular node through internodal pathways. The SA node and the atrioventricular node is connected by internodal pathways which consist of three bands. Electrical signal's travel time between the atriovenctricular node and the SA node is approximately 50 milliseconds [4]. During this time, atria pump the blood into the ventricles. Electrical signal continues travelling to the atrioventricular bundle branches and the Purkinje fibres after passing bundle of His. By the help of Purkinje fibres, the ventricles receive the electrical signal and contract. As the ventricles contract, the blood goes to the lungs from the right ventricle. Meanwhile, the left ventricle pumps the blood to the aorta and the blood is distributed to the rest of the body.

2.4 Measurement of Cardiac Electrical Activity

2.4.1 Standard 12-Lead Electrocardiography (ECG)

In clinics, the electrical activity of the heart is measured by using the standard 12-lead electrocardiography noninvasively. The output of the standard 12-lead electrocardiography is called electrocardiogram. As seen in Figure 2.4, there are three main parts in an electrocardiogram:

- Depolarization in the atria is registered as P wave. Atrial abnormalities are detected by observing duration, amplitude and frequency of the P wave. The interval between the beginning of the upslope of the P wave and the beginning of QRS complex is called PR interval. The duration of PR interval is approximately between 120 and 200 ms [5].

- QRS complex reflects the repolarization of atria and depolarization of ventricles. The QRS complex is composed of Q wave, R wave and S wave. The first negative deflection in the QRS complex is called the Q wave, the first positive deflection is called the R wave and the second negative deflection is called the S wave. The QRS complex has sharper form as compared to the P wave due to the fast conduction velocity in bundle of His and the Purkinje cells. The change in duration of the QRS complex may be indication of arrhythmias, ventricular

9

hypertrophy, or myocardial infarction.

- T wave reflects the ventricular repolarization. The duration between the beginning of the QRS complex and the peak of the T wave is referred as absolute refractory period. The duration between the peak of the T wave and the end of the T wave is referred as relative refractory period. During the absolute refractory period, a new action potential cannot be elicited, whereas in the relative refractory period, a new action potential can be elicited under certain conditions.
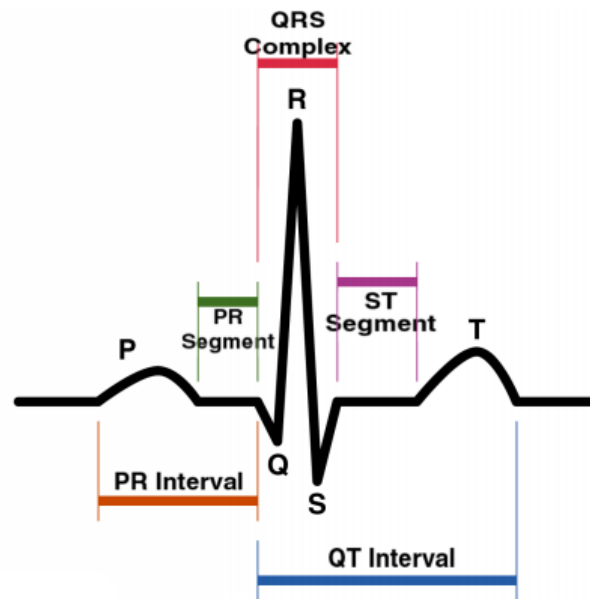
Figure 2.4: The normal electrocardiogram [6]

The standard 12-lead ECG is a patient-friendly and well-established tool but due to limited and fixed lead configuration, many abnormalities such as myocardial infarction, Wolff-Parkinson-White syndrome, left ventricular hypertrophy, and exercise-induced ischemia cannot be detected accurately by using the 12-lead ECG [7]. Abnormalities in the anterior region of the heart can be detected by the 12-lead ECG because of proximity of electrodes on the chest but other abnormalities such as deflection of ST segment during ischemia cannot be detected successfully. In fact, the ECG provides the spatial superposition of many simultaneous events and some of these events may cancel each other, hence the 12-lead ECG may not reflect the extend of physiological abnormalities [8]. One alternative approach to the 12-lead ECG

is Body Surface Potential Mapping (BSPM).

2.4.2 Body Surface Potential Mapping (BSPM)

Body surface potential mapping (BSPM) is superior to the 12-lead ECG that acknowledges the fact that cardiac electrical fields exist everywhere on the body surface. Unlike the 12-lead ECG which relies on interpretation of waveform features including amplitudes, durations, and shapes of the different electrograms, body surface potential mapping focuses on the magnitude, location, and movement of potential extrema as well as the shape and dynamics of isopotential contours throughout the cardiac cycle. BSPM requires 100 to 400 electrodes [9] to record the body surface potentials from a wide region of torso. There are two major advantages of BSPM over the 12-lead ECG [10]:

- Acquisition of the potentials from the entire chest provides all the information on the cardiac electric field available at the body surface.

- BSPM is more sensitive in detecting local electrical events.

One major problem with BSPM is that there is no standard lead configuration as opposed to the 12-lead ECG. Hence, some inconsistencies can arise in different lead configurations. Furthermore, the complexity of processing of the acquired data and their analysis make BSPM impractical as compared to the 12-lead ECG.

BSPM provides high resolution as compared to the 12-lead ECG, however, to fully assess the electrical potential distribution of the heart, we need epicardial potential pattern [11]. Hence, the inverse problem of electrocardiography should be solved to find the epicardial potential distribution.

2.5 Literature Survey on Forward Problem of Electrocardiography

The forward problem of electrocardiography refers to calculation of the body surface potentials from the cardiac electrical activity. The cardiac electrical activity generates time-varying potential signals on the body surface. The relation between the heart's

electrical activity and the body surface potentials is usually formulated by using the bidomain theory under quasi-static approximation of Maxwell's equations [12]. The region Ω bounded by the epicardial surface Γ_e and the torso surface Γ_t is source free, so we write the following Laplace's equation:

$$\nabla \cdot (\sigma \nabla \phi(r)) = 0 \quad \forall r \in \Omega, \tag{2.2}$$

where r stands for the spatial coordinate, ϕ is the potential in the region Ω and σ is the conductivity in the medium. Equation (2.2) is solved by assuming Neumann and Dirichlet boundary conditions. These boundary conditions are given as follows [13]:

$$(\sigma \cdot \nabla \phi) \cdot \hat{a}_n = 0 \quad \text{on } \Gamma_t, \tag{2.3}$$

$$\phi = \phi_e \quad \text{on } \Gamma_e,$$
$$\phi = \phi_t \quad \text{on } \Gamma_t. \tag{2.4}$$

Usually volume or surface methods, Boundary Element Method (BEM) and Finite Element Method (FEM), are used to solve equation (2.2). To employ BEM or FEM, geometric model of the heart and torso surfaces, and the conductivity distribution are needed. Hence, there are two main steps in the forward problem:

- Geometric Model

- Numerical Solution

2.5.1 Geometric Model

As mentioned in the previous section, geometric model is required for the solution of the forward problem. Geometric model includes the surfaces of the heart and the body, the intermediate region between the heart and the body, and the conductivity in the intermediate region. To construct the geometric model, we first need to acquire individual-specific anatomical information. There are two methods for acquiring anatomical information: MRI and CT [8]. This procedure is probably the most major drawback of ECGI as compared to standard 12-lead ECG since usage of MRI or CT increases the cost and the time. By discretization and segmentation of MRI

or CT images, the anatomical structures of the heart and the torso are represented by a group of nodes which form mesh of polygons (triangle meshes for the surfaces, tetrahedra or hexahedra meshes for the volumes) [14, 15].

Organs that are included in the model are assumed to have piecewise homogeneous conductivity. Conductivity of the organs in the intermediate region is usually found by electrical impedance tomography (EIT) [16]. EIT imaging was used in vivo and in vitro in the literature [17].

2.5.2 Numerical Solution

After obtaining patient-specific anatomical and conductivity information, Laplace's equation is solved in the source-free volume between the surfaces of the heart and the body. FEM and BEM are widely used numerical solution techniques in the literature to solve Laplace's equation [18]. There are advantages and disadvantages of these two methods:

- FEM method requires volume meshing, on the other hand, BEM method requires only surface meshing [8]. For the same level of accuracy, BEM uses a lesser number of nodes and elements (but a fully populated matrix), i.e., to achieve comparable accuracy, FEM meshes would need more boundary divisions than the equivalent BEM meshes. Hence, BEM requires less computer time and storage [19].

- Since FEM method uses volume meshes, anisotropic conductivities can be handled easily by the FEM method. BEM method is also capable of considering anisotropic conductivities but the accuracy in FEM method is higher [20].

- BEM is suitable and more accurate for linear problems [19].

- The solution matrix resulting from the BEM formulation is unsymmetric and fully populated with non-zero coefficients, whereas FEM solution matrices are usually much larger but sparsely populated. This means that the entire BEM solution matrix must be saved in the computer core memory. However, this is not a serious disadvantage because to obtain the same level of accuracy as the

FEM solution, BEM method needs only a relatively modest number of nodes and elements [19].

In this thesis, we use BEM based on Barr *et al.*'s article [21] due to its advantages. Solving equation (2.2) using BEM, the forward transfer matrix H is found. H matrix determines the relation between the heart potentials and the body surface potentials.

On the other hand, mesh construction is not an easy task, especially when irregular surfaces are presented. To overcome the difficulties introduced by mesh based methods, meshless methods are also used in the literature of ECGI. One of the meshless methods is Method of Fundamental Solutions (MFS) [22]. In a study, Wang *et al.* [23] compared MFS and BEM methods and concluded that they show similar performances. Using meshless methods may be advantageous since their performances are comparable to other traditional methods and they eliminate the requirement of mesh construction.

2.5.3 Selection of the Number and Positions of Measuring Locations for Electrocardiography

Optimum number of measuring electrodes and their positions on the torso are two important subjects in the forward problem. Barr *et al.* [24] are among the first researchers who focused on these two topics. Their intent was to select the most signal information containing leads and reduce the number of the body surface measurement leads. They used principal component analysis to find a coefficient matrix which is made up of the eigenvectors and a generator matrix which represents the variations in time of the surface voltages. To locate the best recording sites, they adopted a method of iteratively varying the individual chosen surface positions. The study concluded that for an acceptable level of reconstruction accuracy, a minimum of 24 properly located recording positions were required.

Lux *et al.* [9] are another researchers who focused on the lead reduction. In [9], they introduced the notion of an "information index" which provided a method to quantify how well one measurement site correlated with the rest of the sites taking into consideration signal variation. Information index formed the basis of their sequential

selection algorithm. The sequential algorithm picks the lead with the highest information index and takes this to form the first lead in the limited lead set. The information index is then calculated for the remaining leads, and the best lead is again taken. The process is repeated until some stopping criteria is reached. Lux *et al.* concluded that using 20 to 30 leads out of 192 leads can provide the information content of the 192 lead-system.

2.6 Literature Survey on Inverse Problem of Electrocardiography Heart Source Configurations

During the last two decades, inverse problem of electrocardiography or ECGI has been a popular emerging topic among the researchers. There are different solution approaches for solving the inverse problem of electrocardiography. Before giving the literature survey on the algorithms that are used for ECGI, we will give the literature summary on equivalent cardiac source models. The electrical sources in the heart cannot be determined uniquely if the active region is not accessible [25] since the electric field generated by these sources may be replaced by a double or single layer on a closed surface enclosing entirely all of the sources [26].

In the literature, different equivalent cardiac source models such as single dipole, multiple dipoles and multipole approach are used in inverse problem of electrocardiography. These representation types are very basic approximations of the cardiac electrical activity and often fall short for representing the heart's entire electrical activity since according to a study by Hyttinen *et al.*, there should be at least 678 dipole sources in order to simulate the electrical activity of the heart by a relative mean square error less than 1% [27]. Therefore, other source configurations such as transmembrane potentials, epicardial potentials and activation time based models are being used widely.

2.6.1 Dipole, Multiple Dipole and Multipole Source Configuration

Dipole source configuration was first applied to electrocardiography by Einthoven *et al.* [28]. In their research, Einthoven *et al.* represented equivalent source generator

15

as a single dipole. Following Einthoven's study, Yeh and Martinek [29] investigated dipole source configuration in mathematical detail. In their article, Yeh and Martinek assumed torso as prolate spheroid and cardiac source as dipole, then they found the electrical potential on this prolate spheroid [29]. In some cases, using a single dipole as an equivalent cardiac source generator is a good approximation [30–32]. However, many researchers find this approach inadequate since in most cases, dipole source presentation does not yield accurate results and cannot handle current singularities.

Another approach that has been used as equivalent source cardiac generator is multipole source configuration [33–36]. Multipole approach is used in order to take into account the current singularities. Multipole expansion assumes that there are n multipole sources (dipole, quadrupole, etc.) at a fixed location.

Multiple dipoles are also used as equivalent cardiac generators [37–39]. In the multiple dipole approach, the dipole sources are not necessarily at fixed locations.

2.6.2 Epicardial Potential Source Configuration

Dipole, multipole and multiple dipole approaches could be useful for solving the forward problem of electrocardiography, since they provide unique body surface potential distributions. However, in the inverse problem of electrocardiography, the uniqueness of the inverse solution is not mathematically guaranteed [40].

Most of the researchers use epicardial potentials as equivalent source generator due to its numerous advantages. This approach has an advantage over the other methods such as dipole, multipole and multiple dipole since the uniqueness of the inverse solution is mathematically guaranteed [40] and Yamashita proved this fact in his research [26]. According to Martin and Pilkington's work [41], other than unique solution advantage, epicardial source configuration provides two important advantages. First advantage is that there is no need to make restrictive assumptions about the physiologic nature of the cardiac sources, e.g., number of dipoles. Second advantage is that the intracavity blood mass is included in the problem formulation as a result of using epicardial source configuration. Hence, the most important inhomogeneity is implicitly taken into account [41]. Other works related to epicardial source configu-

16

ration are [21, 42–47].

2.6.3 Transmembrane Potential Source Configuration

Transmembrane potential (TMP), the potential difference between the intracellular and extracellular space, is another type of representation that is being used for cardiac source modelling. TMP source configuration is defined as a macroscopic quantity and is the average potential over small volume of tissue including several cells. Although transmembrane source configuration is not widely used as compared to epicardial potential source configuration, it has been used by some researchers [48–50]. Formulating the problem using TMPs results in a linear problem as shown in [50]. Reducing the problem formulation to a linear problem is the main advantage of transmembrane source configuration. Another advantage of TMP source configuration is that three dimensional representation of cardiac sources by TMPs may provide a better understanding of the mechanisms of cardiac pathophysiology. However, as mentioned in Messnarz *et al.*, the solution is not unique and that's why TMP source configuration is not used widely [48].

2.6.4 Activation Time Based Source Configuration

As an alternative approach, myocardial activation time sequence is preferred by some researchers [51–54]. Retrieving myocardial activation time sequence from the body surface potentials has advantages over epicardial source configuration approach since activation time based approach is directly related to physiological mechanism that lies behind the heart depolarization and repolarization. However, the complexity of the problem is increased with this approach since one needs to model the heart fully rather than just the epicardial surface because myocardial activation times rather than just epicardial potentials are being related to body surface potentials [53]. The major drawback of activation time based source configuration as compared to TMP is that in this method, the problem becomes nonlinear and the calculations are very complex due to nonlinearity.

2.7 Literature Survey on Inverse Problem of Electrocardiography Solution Algorithms

Unfortunately, the coefficient matrix which relates the heart potentials and the body surface potentials, so-called the forward transfer matrix, is ill-conditioned and rank-deficient [55]. The inversion of the forward transfer matrix, i.e., solving the inverse problem, is therefore ill-posed and straightforward inversion would lead to unphysiological solutions. Consequently, more advance solution techniques, i.e., regularization techniques, should be introduced to the problem. The underlying idea of regularization is to impose constraints on the solution. Due to space-time nature of the sources, regularization can be applied in both domains. In this section, we present the techniques that have been used to solve the inverse electrocardiography problem.

2.7.1 Spatial Regularization Methods

In this section, we present deterministic approaches that have been used in the literature. There are many deterministic methods to deal with ill-posedness nature of inverse electrocardiography. In general, these methods introduce some constraints to regularize the problem. We organized these methods into three groups according to their regularization techniques:

- Tikhonov regularization is a widely used technique in the literature [56–59]. Wang *et al.*'s [60] study is a good and recent example of Tikhonov regularization. In their study, Wang *et al.* used ECG imaging and phase mapping to 3D reconstruct re-entry circuit and its dynamics, which is important in ventricular tachycardia (VT). In the analysis, Wang *et al.* used homogeneous volume conductor as a torso model. As a heart model, they used the epicardial and endocardial surfaces for both ventricles. In order to solve the inverse problem, they used second-order Tikhonov regularization. To detect re-entry circuit structure, they used phase mapping approach [61] and took Hilbert Transform of reconstructed electrograms and found the phase map. When the phase crossed zero from negative to positive, the depolarization wave front was found. Wang *et al.* investigated three different VT re-entry circuits. They concluded that recon-

struction of both epicardial and endocardial layers were essential in this study, and phase mapping could reveal the regions of slow conduction.

- Iterative Methods: truncated singular value decomposition (TSVD) [55], minimum residual method (MINRES) [62] and conjugate gradient [62]

- Non-quadratic Methods: total variation [63,64] One good example of total variation technique in the context of the inverse electrocardiography is the study of Xu *et al.* [64]. Spatial gradient of cardiac intramural action potential is a good indicator to differentiate viable and necrotic tissue. During ST region of ECG cycle, spatial gradient of intramural action potential should be close to zero. Therefore, observation of the gradient map provides information about arrhythmogenic region [64]. Since the gradient of cardiac intramural action potential carries important information, Xu *et al.* [64] used total variation minimization technique to constrain the problem of the inverse electrocardiography. In order to this, they included total variation function as a penalty term. Total variation function was L1 norm of the gradient of intramural action potential. To calculate total variation function, instead of using the gradient operator, Xu *et al.* used numerical integration over *N* Gaussian quadrature points in the myocardium region. After formulating total variation function, they adopted Rodriguez and Wohlberg's [65] iteratively re-weighted norm approach to solve the optimization problem. Xu *et al.* compared their algorithm performance with zero order and first order Tikhonov regularization and, in general, their approach performed better in detecting cardiac infarct.

An important and open question in inverse ECG literature is whether to choose L1-norm penalty function or L2-norm penalty function. In [59], Ghosh *et al.* pointed out that using L1-norm better suited for localization of epicardial pacing sites. On the other hand, Rahimi *et al.* [66] stated that these solution methods provide too focal or too smooth solutions which often do not fulfil our purpose to find cardiac source distribution. Hence, they proposed Lp norm regularization to find a balance between focal and smooth solutions. In order to solve Lp norm regularization, Rahimi *et al.* used p-order cones programming (p-OCP). They concluded that L1 norm performs well when the cardiac source distribution is sparse and focal, and L2 norm performs

well when the cardiac source distribution is more scattered. Lp norm regularization performed better in the general sense since it is designed to fill the gap between the L1 norm and L2 norm.

In another study, Coll-Font *et al.* [67] compared L1-norm solution and L2-norm solution. In their article, Coll-Font *et al.* [67] combined spatial and temporal regularization techniques. As the space regularization, they used L1-norm and L2-norm of the gradient of the heart potentials for the penalty term. Coll-Font *et al.* combined these two spatial regularization techniques with a temporal regularization technique and compared them to each other. In order to regularize the heart potentials temporally, Coll-Font *et al.* used B-spline function [68]. B-spline function finds best knot points and these points' temporal mixing. Using the temporal mixing obtained before, they approximated the heart's temporal sequence. In this study, Coll-Font*et al.* aimed to find the first activation area in the heart. Dataset for this study was obtained from three patients who underwent cardiac surgery. During the surgery, the heart was paced from different locations and the potentials were collected. To find the forward transfer matrix, CT scans and BEM were used. Most of the cases, L2-norm regularization showed better performance. However, when the initial pacing site is in the right ventricle, L1-norm regularization showed better performance.

2.7.2 Spatio-Temporal Regularization Methods

Traditional regularization methods, or spatial regularization methods, ignore the temporal aspect of the cardiac electrical activity and solve the problem at each time instant separately. Spatio-temporal regularization methods take advantage of the temporal dynamics of the system and solve the inverse problem of electrocardiography jointly in space and time as in Coll-Font *et al.* [67]'s study. We organized these methods into three groups:

1. Structural Constraints: The studies of Greensite, one of the pioneer researchers in inverse electrocardiography literature, are the examples of this group [69,70].

   In his article, Greensite [69] built a mathematical background and showed that under the isotropy assumption, the temporal correlation could be included to

the problem by a Kronecker product. In [70], Greensite continued his study and investigated multivariate spatio-temporal linear inverse problem. By presenting several assumptions on the covariance matrix, he was able to estimate temporal correlation from the measurements and found the solution by using orthogonal transformations.

Structural constraints method had been used by our research group. Onal *et al.*'s study [71] was one example of this approach. In their study, Onal *et al.* followed Greensite's approach and applied a temporal whitening filter to the original problem. By applying the temporal whitening filter, the problem became temporally decorrelated and they solved this new problem by using Tikhonov regularization and Bayesian maximum a posteriori approach. Then, they transformed the results back to the original domain and the desired solution was obtained. Onal *et al.* compared spatio-temporal approaches with spatial approaches and concluded that the solutions improved when the temporal relations were taken into account.

2. Kalman Filter: Joly *et al.* [72] are among the first researchers who applied Kalman filter to inverse problem of electrocardiography. They used state-space approach for modelling the inverse electrocardiography problem and modelled the state transition matrix as a constant times identity matrix where the constant was calculated by the least-squares approach. The forward transfer matrix was found by using FEM in their study. Using these parameters, they applied Kalman filter to the problem.

The relation between the state variables was ignored in Joly *et al.*'s [72] study and clearly, this assumption was not realistic. Based on Joly *et al.*'s study, El-Jakl *et al.* [73] proposed another method and used maximum likelihood (ML) method to estimate the state transition matrix, the measurement noise covariance matrix and the process noise covariance matrix. They assumed the process noise and the measurement noise are white noise. After the ML step, they applied Kalman filter to find epicardial potentials.

More recent studies on Kalman filter application in the inverse problem of electrocardiography were conducted by Wang *et al.* [74, 75].

In [74], Wang *et al.* implemented an algorithm to:

- Construct non-linear state transitions and a priori information using the electrophysiological model that describes the spatio-temporal behavior of TMP distributions,

- Estimate the 3D TMP distributions based on the abovementioned a priori information and using Unscented Kalman filter (combines the advantages of Kalman filter updates and Monte Carlo methods),

- Evaluate the performance of the proposed method for potential clinical usability.

They used segmented medical images to obtain geometric models; fiber orientations from a previous experimental study were registered onto the heart geometry for modelling the cardiac anisotropy. Meshless BEM method was used to solve the forward problem under the assumption of isotropic and homogeneous torso model. Two sets of data were used in this study:

- Simulated TMP potentials and the corresponding body surface potentials (BSP): Two-variable reaction-diffusion model were used for simulating TMPs. From these TMPs, BSPs are obtained by solving the forward problem,

- Data from a patient with myocardial ischemia.

They tested their algorithm based on robustness to different data error models, robustness to reaction-diffusion model parameters, electrode misplacement, geometric modelling errors and ability to localize ectopic foci. Overall, Wang *et al.*'s approach yielded better results in terms of estimated transmembrane potentials when compared to zero order Tikhonov regularization and TSVD.

In [75], Wang *et al.* applied their framework, which was explained before in [74], to post myocardial infarction patients to detect 3-D scar mass noninvasively. They asserted that their algorithm provided the infarct size, the extent of the infarct and 3-D infarct geometry. Some of these information could not be provided by the previous works done by [76, 77]. Wang *et al.* used unscented Kalman filter with a feedback in order to find the parameters which determine the size and the location of the infarct.

Another Kalman filter based approach was conducted by Schulze *et al.* [78].

In their study, Schulze *et al.* first applied second order Tikhonov regularization to the forward transfer matrix to deal with its ill-posedness nature. Then, they modified Kalman filter equations to integrate pseudo-inverse of the forward transfer matrix. They compared the real and the reconstructed epicardial potentials by using Kalman filter and modified Kalman filter. Schulze *et al.* concluded that modified Kalman filter approach yielded better results in terms of correlation coefficients.

Kalman filter also had been used by our research group [79–82]. In [79], Aydin *et al.* stated that in order to use Kalman filter, one needs to know the state transition matrix that models the time evolution of the epicardial potentials. They proposed three different approaches to find the state transition matrix under the assumption of epicardial potential at one lead is related to:

- Only the leads in its neighbourhood,

- The leads that are activated at around the same time,

- Both the leads with close activation times and its first order neighbours.

Aydin *et al.* used the modified Kalman filter equations suggested by Joly *et al.* [72] and found the state transition matrix. They concluded that the assumption of one lead is related to both the leads with close activation times and its first order neighbours yielded better results.

Aydin *et al.* [80] continued their study and proposed another approach. In their previous study [79], they used true epicardial potential distributions to estimate the state transition matrix. In [80], they estimated the state transition matrix by using epicardial potential distributions obtained from Tikhonov regularization and Bayesian MAP estimation solutions. The results of this study showed that the state transition matrix calculated by using Bayesian MAP approach yielded better results.

In [82], Aydin *et al.* focused on reducing the effects of the geometric errors in inverse electrocardiography problem. They followed Kaipio *et al.*'s approach [83] and modelled the geometric errors as additive Gaussian noise and their noise variance was added to the measurement noise variance. To estimate the measurement noise variance and the process noise variance, Aydin *et al.* used

two different algorithms:

- An algorithm based on residuals,

- Expectation maximization algorithm.

They concluded that the algorithm based on residuals produced better results.

Until now, we have given the literature review on regular Kalman filter. As mentioned before, if activation time sequence is used as the source configuration, the relation between the sources and the body surface potentials is nonlinear. Hence, to handle the nonlinearity, extended Kalman filter (EKF) must be used. The following two studies are important in this regard:

In [84], Ghodrati *et al.* proposed a novel algorithm to noninvasively estimate the epicardial activation wavefront curve employing the EKF. They modelled the nonlinear relationship between the epicardial activation wavefront curve and the BSPMs, and set up the state-space model by incorporating general physiological knowledge, e.g., conduction velocity.

In [85], Liu *et al.* formulated the problem by using cardiac activation sequence. Since the relation between the cardiac activation sequence and body surface potentials is nonlinear, they used EKF. They handled ill-posedness nature of the problem by introducing a cost-efficient regularization method in the EKF. The EKF-based algorithm showed good performance in simulation under single-site pacing and dual-site pacing with correlation coefficients between the estimated activation sequences and true values 0.95 and 0.93, respectively.

3. Regularization Using Multiple Constraints: Brooks *et al.* [57] proposed a joint regularization scheme which incorporated both spatial and temporal regularization constraints (JTS), and a joint regularization scheme which incorporated two different spatial regularization constraints. They compared these two regularization schemes and concluded that JTS regularization yielded better results.

   Regularization parameter selection is an important issue in regularization using multiple constraints approach. In [86], Serinagaoglu *et al.* addressed this issue and suggested a genetic algorithm based approach to select the regularization parameter.

4. Admissible Solution: This method was proposed by Ahmad *et al.* [87]. In their study, Ahmad *et al.* used spatial constraints, temporal constraints and weighted constraints together to regularize the problem. This method differs from regularization using multiple constraints approach since no regularization parameter is selected in this method, instead, regularization parameters are replaced with direct bounds.

2.7.3 Bayesian Approach

Spatial and spatio-temporal methods are widely used to deal with the ill-posed nature of the inverse problem of electrocardiography. In addition to these regularization techniques, statistical approaches are also used effectively in the literature. Statistical approaches enable the researchers to evaluate the performances of their algorithms quantitatively since these approaches can provide more information such as error covariance [88].

Bayesian MAP algorithm is one of the most widely applied solution approaches among the statistical algorithms. Bayesian based approaches have been applied to inverse ECG problems as well as inverse EEG/MEG problems. In Bayesian MAP method, as the name implies, the goal is trying to maximize the posterior probability density function.

In the context of EEG/MEG studies, Schmidt *et al.* [89] is one of the researchers who applied Bayesian inference approach to EEG/MEG problem. Schmidt *et al.* used Markov Chain Monte Carlo (MCMC) to sample the a posteriori distribution given measurement data and a priori information. Instead of giving a single best estimate, they gave whole range of likely solutions as well as their reliability.

Another research conducted by Russell *et al.* [90] in the context of the inverse problem of EEG/MEG is important. Russell *et al.* developed a framework in order to estimate the error of imaging modality. To do this, first, they modelled the relation between the brain sources and the scalp measurements as linear. By assumption of Gaussian distribution for the prior and independent, identically distributed noise, they were able to write the prior, and the likelihood using chi-square statistic. After finding the

prior and the likelihood, it was easy to find the evidence by using Bayes' formula. They asserted that if different prior models are compared in the sense of explaining the measurements, the best prior model is the one which maximizes the evidence. In order to apply this idea, they set the gradient of the posterior to zero and found dipole moment vector.

Bayesian MAP algorithm was first applied to the inverse problem of electrocardiography by Martin *et al.* [91]. They solved the inverse ECG problem by using the framework developed for the optimum estimate of the epicardial potential vector by Foster [92]. Martin *et al.* used epicardial potentials as source, assumed Gaussian distribution with zero mean. Using an activation-time based formula which utilizes the work done by Pilkington *et al.* [93], Martin *et al.* found the epicardial and torso potentials.

Barr *et al.* [45] followed Martin *et al.*'s approach and imposed statistical constraints to the inverse problem of electrocardiography. They used invasive epicardial potentials that were collected from the heart directly and body surface potential measurements assuming that the intervening volume conductor was homogeneous. They modelled epicardial and noise covariances as a constant times identity matrix. Then, they used the formula developed by Foster [92] and Strand *et al.* [94], which minimizes the sum-squared error of the epicardial potentials, assuming Gaussian zero mean distribution for epicardial potentials. Inspection of correlation coefficients and graphical visualization between true and estimated epicardial distributions revealed that the results were not very good and this is somewhat expected due to constant covariance matrices assumption.

van Oosterom [95] is another researcher who applied maximum a posteriori approach to the inverse problem of electrocardiography. In his research, van Oosterom compared different solution techniques with Bayesian MAP algorithm, namely zero-order Tikhonov regularization, second-order Tikhonov regularization and TSVD. Starting from uniform dipole layer (UDL), van Oosterom found epicardial potentials by using boundary element method (BEM). van Oosterom used epicardial potential source configuration which has Gaussian distribution with zero mean similar to the work conducted by Martin *et al.* [91]. Using the inverse method given by Dale *et al.* [96],

van Oosterom proposed a MAP-based solution technique. Bayesian MAP algorithm performed better compared to the other solution approaches in terms of correlation coefficient between estimate epicardial potentials and true epicardial potentials. However, zero mean assumption may yield infeasible results and it is not realistic.

Another research that is important in the context of Bayesian MAP algorithm is conducted by Serinagaoglu *et al.* [97]. Serinagaoglu *et al.* used a database that consists of epicardial potentials collected from previous experiments and a set of catheter-based electrical measurements, and modelled epicardial potentials as Gaussian. They used BEM method to find the forward transfer matrix. Their intent to use invasive but sparse potential measurements was to increase the resolution of the solution. Assuming Gaussian distribution for epicardial potentials, they estimated epicardial potentials based on Bayesian MAP technique [98]. Since, Serinagaoglu *et al.* assumed zero mean Gaussian noise uncorrelated with the epicardial potentials, their Bayesian MAP solution algorithm is equivalent to minimum mean square error (MMSE) estimation. In this formulation, prior probability density function is an important factor that directly affects the solution. In order to find prior probability density function, Serinagaoglu *et al.* chose different epicardial potentials from the database in a manner that the prior model maximizes the evidence and formed a hybrid epicardial potential distribution.

In [88], Serinagaoglu *et al.* continued their previous research on Bayesian approach. In their article, they compared different solution algorithms for different scenarios. Tikhonov regularization and Bayesian MAP algorithms were used in their research. Tikhonov regularization was tested by using only torso potentials, and using torso potentials and sparse epicardial potentials that were collected by catheter-based measurements. Bayesian MAP algorithm was tested by using the following information:

- Torso potentials and the prior information which was explained in [97],

- Torso potentials, the prior information and sparse epicardial potentials directly collected from the heart,

and they concluded that combining different information yields better results.

2.7.4 Modelling Error Studies

Modelling errors directly affect the solution of inverse electrocardiography. The effects of the modelling errors are studied widely in the literature [99].

Statistical approaches can also be used to analyse the effect of the geometric errors on the solution. Heart-torso modelling is very important in solving the inverse problem of electrocardiography and modelling errors directly affect the accuracy of the solution. Rahimi and Wang [100] worked on this topic and proposed a statistical approach to evaluate electrophysiological imaging methods' robustness to the variations in the personalized heart-torso models. They used statistical shape modeling (SSM) [101] and constructed a Gaussian random variable for the variation of personalized heart-torso model. Since the relationship between the anatomical model and the inverse problem solution was complex, thus could not be analytically formulated, they used unscented transform to obtain the inverse problem solution statistics. Due to high dimension of the solution, Monte Carlo analysis and similar approaches could not be used because of their computational cost. In this study, two source configurations were used, namely epicardial potentials and transmural action potentials. Two solution algorithms were used for these two source configurations: zero order Tikhonov regularization was used for epicardial potentials and transmural electrophysiological imaging (TEI) [74] was used for transmural action potentials. Rahimi *et al.* tested their study with synthetic experiments and real data experiments. Before applying their algorithms, they obtained a set of anatomical models. In synthetic experiments, despite the differences between anatomical models, the reconstruction of epicardial potentials showed similar patterns. Real data experiments confirmed the results of synthetic experiments. Therefore, they concluded that the applied solution methods have low sensitivity to anatomical model variations.

In another study, Burton *et al.* [102] investigated uncertainties in the forward and inverse ECG problem. In the forward problem, the authors examined tissue conductivity uncertainty during repolarization phase in an ischemic heart. In the inverse problem, they studied Tikhonov regularization control parameter effect on the reconstructed activation times. For the forward problem part of this study, Burton *et al.* determined a range of conductivity values of the heart and assumed uniform distribu-

tion for the conductivity values. They used generalized polynomial chaos-stochastic collocation methods (gPC-SC) to reduce the stochastic equations and found a finite set of deterministic simulation parameters which govern the stochastic process. This process enabled them to extract the mean and pdf of the solution. In the inverse problem part, they used Erem *et al.*'s approach [103]. Only the Tikhonov regularization parameter was considered as the variable which brought uncertainty to the solution. The spatial mean and standard deviation were found for different Tikhonov regularization parameter values. Uncertainty of both the conductivities and the regularization parameter were visualized.

Another important study was conducted by Zemzemi *et al.* [104]. Zemzemi *et al.* examined the effect of the torso heterogeneities on inverse ECG solution. First, they constructed the heart-torso model using CT scan images. Then, the forward problem was solved by using Laplace equation assuming that the conductivity in torso is heterogeneous. After finding body surface potentials by using the result of forward problem, they added some noise on the simulated body surface potentials and solved the inverse problem by using zero order Tikhonov regularization algorithm. Zemzemi *et al.* solved the same problem by assuming homogeneous conductivity and compared the solution with heterogeneous case. In terms of correlation coefficient and relative error metrics, the heterogeneous case outperformed the homogeneous case.

Inverse electrocardiography procedure often requires accurate patient specific thorax model. Sometimes, getting accurate thorax model is not possible or in order to reduce the negative effects of CT, it is desirable to decrease field of view of CT imaging. In their study, Erem *et al.* [68] aimed to eliminate the need of an accurate model. They used a spline-based method and this method was applied to body surface potentials for the temporal regularization of the heart surface potentials. In order to find the knot points of the heart potentials, Erem *et al.* used Tikhonov regularization combined with transmural gradient regularization. Transmural gradient regularization was used for finding regularization matrix parameter in Tikhonov regularization. In this study, the authors estimated the location of the pacing site. In general, the results were comparable to those which uses accurate throax models.

In [103], Erem *et al.* continued their study and proposed an algorithm to evaluate

parameter sensitivity and model inaccuracy in the inverse ECG problem. The algorithm utilized nonconvex, nonlinear least squares optimization. Source distribution was presented by transmembrane potentials. Transmembrane potential was modelled as unit step function $u(t - \tau_n)$ where τ_n denotes the activation time. Since nonlinear least square optimization algorithms require differentiable objective functions, Erem *et al.* introduced some constraints to the problem, which formulated the abrupt transition from 0 to 1 at the time τ_n and replaced it with a smooth transition, so that they could apply the optimization algorithm. Since the problem was nonconvex, Erem *et al.* replaced the problem with a convex one and solved the problem by using alternating directions method of multipliers (ADMM) method. In order to test the robustness of the algorithm, they used fast route algorithm (FSA). In the FSA algorithm, some initial foci and related wavefront propagation patterns were estimated, and the body surface potential distribution was found. Then, the correlation between real body surface potentials and estimated body surface potential distribution was found. Erem *et al.* were aware of approximating the nonconvex problem by a convex one violates the problem and could be yielding infeasible solutions. However, they stated that one can always find waveforms, in the nearest feasible neighbor region, similar to those found by using convex optimization. The solution algorithms were applied to real data collected from two healthy male subjects and simulation data using the software ECGSim [105]. Overall, Erem *et al.* concluded that their proposed method was fairly robust.

2.7.5 Multiple Measurements Studies

In inverse problem of electrocardiography, often, multiple body surface measurements are available. However, which measurement should be used for the best results is still an important question. In the literature, two standard approaches are being used. One method takes the all measurements one by one and finds the inverse solution for each measurement, then finds ensemble average of the solutions. The second method finds ensemble average of the measurements and solves the inverse problem. These two approaches assume that the measurements are independent realizations of the system, however this is not true since the measurement noises are correlated. Coll-Font *et al.* [106, 107] tried to answer that question. Coll-Font *et al.*

proposed two solution algorithms: pre-averaging method and probabilistic inverse. In pre-averaging method, they proposed an algorithm that uses B-spline method using pseudo-time and knot points as parameters. The difference between the measurement and B-spline model was minimized and Coll-Font *et al.* applied Tikhonov regularization to this model. In the probabilistic part, close inspection of the measurement distribution revealed that the measurement data could be represented as Laplacian distribution. Using zero mean Gaussian distribution for the prior probability, they found the MAP estimate of the posterior probability distribution by applying alternative directions method of multipliers (ADMM) method. Since the dataset was very limited and proposed probabilistic models were simple, Coll-Font *et al.* could not reach any conclusion on which algorithm is better.

In another research, Dallet *et al.* [108] proposed multi-lead signal averaging algorithm to make use of multiple beats. They aimed to eliminate errors due to faulty measurements when single beat is used. In multi-lead signal averaging algorithm, they selected a set of beats and applied reduced-rank principal component analysis (PCA) to the selected beats. Then, they applied spatial averaging on the PCA-filtered beats. Correlation coefficient and root mean square were found between a reference ECG signal and selected beats to choose the most representative beats from the selected set. After finding the most representative beats, they computed average of the beat set.

2.7.6 Other Approaches

In the literature, there are other important solutions methods that are applied to the inverse problem of electrocardiography. One of them is a method that is called "Hierarchical Multiple-Model Bayesian Approach" applied by Rahimi *et al.* [109, 110]. In their study, Rahimi *et al.* investigated the inverse problem of electrocardiography using hierarchical multiple-model Bayesian inference. According to Bayes' formula, the posterior pdf is proportional to the prior pdf multiplied by the likelihood pdf. The prior pdf was modelled as p-generalized Gaussian distribution. In order to establish an adaptive approach, they modelled p as a random variable with uniform distribution between 1 and 2 meaning that if p is 1 then the prior pdf is Laplacian or if p is 2

then the prior pdf is Gaussian. On the other hand, the likelihood pdf was assumed to be Gaussian random variable with zero mean. In this formulation, there were three hyperparameters, namely the noise variance, p value and the source prior variance. The source prior variance and the noise variance were assumed to be uniform random variable and they control the regularization contribution of the source and the data fitting respectively. In order to do a full Bayesian analysis, Rahimi *et al.* found the posterior pdf by using slice sampling Markov Chain Monte Carlo method [111]. They sampled three hyperparameters and found the joint posterior over three hyperparameters. This approach is very advantageous over the fixed model approaches where the noise variance, p value and the source prior variance are fixed. While Rahimi *et al.*'s approach is very flexible to different source distributions, fixed model approaches are only suitable for specific cases.

Another important approach is Variational Bayes method. This method was applied by Xu *et al.* [112]. In this study, Xu *et al.* used variational Bayesian (VB) method for intramural action potential imaging of 3D infarcts. According to Xu *et al.*, Variational Bayes method provides flexible regularization parameters and therefore eliminates disadvantages of fixed regularization parameters. First, they introduced two new parameters to the system, namely inverse variance of the measurement noise and inverse variance of the prior both having Gamma distribution. They formulated the likelihood pdf as Gaussian and derived the pdf as a function of inverse variance of the measurement noise. Furthermore, they formulated the conditional prior model, conditioned on inverse variance of the prior, which resulted in normalized exponential function of inverse variance of the prior multiplied by total variation function where total variation function was found by numerical integration. After finalizing the formulation, they combined all the pdfs, namely the conditional likelihood pdf, the conditional prior pdf, inverse variance of the measurement noise pdf and inverse variance of the prior pdf, to find the joint probability density function of a hyperparameter (variable consists of inverse variance of the measurement noise, inverse variance of the prior and the prior) and the measurement data. The posterior distribution of the hyperparameter involved intractable integral. To overcome this issue, they used minimization of Kullback-Leibler (KL) divergence technique. By using KL divergence, they found the mean and covariance for the posterior distribution of the source. They compared

their approach with total variation regularization and first order Tikhonov regularization. Phantom and human data were used to test the methods. Two following metrics are used to evaluation: correlation coefficient between true and reconstructed action potentials, dice coefficient between true and reconstructed ischemic regions. In the experiments, VB method outperformed first order Tikhonov regularization but its performance was comparable to total variation regularization.

Machine learning algorithms are also used in the literature. There are two important studies by Zemzemi *et al.* [113, 114] on this topic. In [113], they used Reproducing Kernel Hilbert Space (RKHS) method, a machine learning algorithm, to solve inverse ECG problem. They used different pairs of heart potentials and body surface potentials to train their algorithm and found a function that represents the relation between the heart potentials and the body surface potentials. The forward problem was solved by using monodomain model due to its simplicity. The electromagnetic equations were solved by using finite element method (FEM). After finding the function that maps the heart potentials to the body surface potentials, Zemzemi *et al.* tried to reconstruct the heart potentials by using the body surface potentials which were not in the training data set. Stimuli localization error was about 0.5 cm and activation time error was around 6 ms. Zemzemi *et al.* stated that rich training set improves the reconstruction accuracy. Zemzemi *et al.* [114] continued their study and proposed the following algorithms: Tikhonov regularization, statistical reproducing kernel Hilbert space (RKHS) [113], least square algorithm regularized with RKHS, least square algorithm regularized with the nearest solution selected from a database. The results with using these four algorithms were compared. The data set that was used for training the algorithm was taken from 400 simulation cases which have different stimulation points. In terms of potential amplitude, regularization of RKHS method improved the performance of the classical RKHS algorithm. Furthermore, Zemzemi *et al.* observed that nearest solution method yielded shifted potential waveform and Tikhonov regularization yielded over-smoothed solutions. In terms of activation times, the regularized RKHS and the classical RKHS provided accurate location of ectopic stimuli. However, due to the shift in nearest solution algorithm and over-smoothed waveform in Tikhonov regularization, these approaches did not give accurate results.

33

2.8 Novelty of The Presented Work

In experimental and simulation studies of non-invasive electrocardiographic imaging, as mentioned in section 2.7.5, multiple measurements of the body surface and epicardial potentials are available. However, the best way to utilize all available measurements still remains an open question in the current inverse electrocardiography literature. Furthermore, in the state-space approaches of the inverse electrocardiography, there is an open question of how the state transition matrix and the covariance matrices are found. Joly *et al.* [72] attempted to model the state transition matrix as a constant times the identity matrix and this approach is a poor approximation since it ignores the relation between the state variables. Based on Joly *et al.*'s study, El-Jakl *et al.* [73] proposed another method to find the state transition matrix by using maximum likelihood estimation. However, El-Jakl's study also assumed the covariance matrices as a constant times the identity matrix and lacks of providing information on how the multiple measurements was used. Aydin *et al.* also tried to find an answer to the above-mentioned questions in a series of publications [79–82]. In these studies, Aydin *et al.* modified Joly *et al.*'s approach [72] to find the state transition matrix. They assumed epicardial potential at one lead is related only the leads in its neighbourhood or the leads that are activated at around the same time, while finding the state transition matrix. Hence, in their study, it is important how the neighbourhood leads are defined. Furthermore, any errors that are made during the calculation of activation times may yield incorrect state transition matrix.

In this thesis, we propose two new methods which incorporate the multiple measurements by using maximum likelihood and maximum a posteriori estimation. Our approach provides a general way to construct the state-space formulation of the inverse electrocardiography by using very few assumptions.

CHAPTER 3

THEORY

In this section, first, we introduce the problem definition and formulate the relation between body surface potentials and epicardial potentials. Then, we discuss inverse problem solution algorithms used in this study in detail.

3.1 Problem Definition and State-Space Formulation of the Problem

Cardiac electrical activity can be observed noninvasively by measuring the body surface potentials. The relation between body surface potentials and cardiac electrical activity is linear if epicardial potentials are used as the equivalent cardiac source model. Due to this linear relation and other benefits that are explained in section 2.6.2, we used epicardial source configuration in this study. The relation between epicardial potentials and body surface potentials, and the relation between epicardial potentials at different times can be defined mathematically in state-space form as follows:

$$y_k = Hx_k + v_k$$
$$x_{k+1} = Fx_k + w_k \tag{3.1}$$

where

- $x_k \in \mathbb{R}^M$ denotes M dimensional epicardial state vector at time k

- $y_k \in \mathbb{R}^D$ denotes D dimensional body surface potential vector at time k

- $F \in \mathbb{R}^{M \text{x} M}$ is state transition matrix

- $H \in \mathbb{R}^{D \text{x} M}$ is forward transfer matrix

- $w_k \sim \mathcal{N}(w_k; 0, Q)$ is uncorrelated with the state, Gaussian process noise with zero mean and covariance matrix $Q^{M \mathrm{x} M}$

- $v_k \sim \mathcal{N}(v_k; 0, R)$ is uncorrelated with the state, Gaussian measurement noise with zero mean and covariance matrix $R^{D \mathrm{x} M}$

- $x_1 \sim \mathcal{N}(\bar{x}, \Sigma)$ is the initial epicardial potential state

The forward transfer matrix H is found by the procedure given in section 2.5.2. H is an ill-conditioned matrix, meaning that the condition number of H is very large. Small measurement disturbances cause unbounded errors in the epicardial potential distributions due to the high condition number of H. Hence, solving for the epicardial potentials requires regularization [115].

3.2 Inverse Problem Solution Methods

In this section, we explain the inverse problem solution methods. We use both spatial and spatio-temporal methods in this thesis. Spatial methods include Tikhonov regularization and Bayesian maximum a posteriori techniques. Spatio-temporal methods include Kalman filter and regularized Kalman filter approaches. In general, the spatio-temporal methods perform better than the spatial methods since, as Oster *et al.* [116] pointed out, the temporal correlation between the epicardial potentials should also be used to get accurate results.

3.2.1 Tikhonov Regularization

Tikhonov regularization is the most widely used regularization method for the solution of ill-posed inverse problems. Tikhonov regularization was named after the publication of Tikhonov and Arsenin [56]. Since the forward transfer matrix is not directly invertible and the problem is ill-posed, Tikhonov regularization is used for stabilizing the solution. In general, the solution of the inverse problem is found by minimizing a cost function as follows:

$$\hat{x} = \underset{x}{\mathrm{argmin}}(||Hx - y||_2^{\,2} + \lambda^2 ||\mathcal{L}x||_2^{\,2}) \qquad (3.2)$$

where λ is the regularization parameter and $\mathcal{L}$ is the regularization matrix.

The regularization parameter λ controls the contributions of residual error and solution norm. Selection of the regularization parameter is very important because too small λ values cannot eliminate the instability, too large λ values over-smooth the solution and add unnecessary residual error while stabilizing the system [117]. The system diverge from the real solution when too much unnecessary residual error is added. Hence, there is a trade-off between instability and over-smoothing.

After minimization of equation (3.2), the solution is given as follows:

$$\hat{x} = (H^T H + \lambda^2 \mathcal{L}^T \mathcal{L})^{-1} H^T y \tag{3.3}$$

To find the optimal value of λ, we use the **L-curve** method [117]. In this method, we plot $||Hx - y||_2$ vs $||x||_2$ in log-log scale by varying λ parameter. This plot usually has an L-shape, hence the name L-curve method, and we select the point corresponding to the corner of this curve. The value of λ parameter at this point is the optimal one because it satisfies the minimum norm solution and minimum error properties [118]. The only unknown left in equation (3.3) is the regularization matrix $\mathcal{L}$. **Zero order Tikhonov regularization** uses the identity matrix I as the regularization matrix, first order Tikhonov regularization uses the surface gradient matrix G as the regularization matrix and second order Tikhonov regularization uses the surface Laplacian operator $\tilde{\mathcal{L}}$ as the regularization matrix. In this study, we used zero order Tikhonov regularization.

Tikhonov regularization works like a filter. It filters out small singular values of the forward transfer matrix. To see this effect, we apply singular value decomposition (SVD) to the forward transfer matrix and replace H matrix by its decomposed representation in equation (3.3):

$$H = USV^T \tag{3.4}$$

where $S = (s_1, s_2, \ldots, s_D)$ is the singular value matrix which is a diagonal matrix consisting of singular values, U is the left eigenvector and V is the right eigenvector of H. Replacing H with equation (3.4) yields:

$$\hat{x} = \sum_{i=1}^{n} \underbrace{\frac{s_i^2}{s_i^2 + \lambda^2}}_{g(s_i, \lambda)} \frac{U_i^T y}{s_i} V_i \tag{3.5}$$

By inspecting equation (3.5), it can be concluded that $g(s_i, \lambda) \approx 1$ for large singular values and $g(s_i, \lambda) \approx 0$ for small singular values. Therefore, Tikhonov regularization

37

damps the effects of division by the small singular values. However, large singular values still affect the solution.

3.2.2 Kalman Filter and Smoother

Kalman filter is an optimal estimator which is used for estimating the unobserved states of a system by using the observed data. Kalman filter's optimality is due to its minimizing the mean square error of the estimated states when the noise is Gaussian property. Kalman filter is a well known method and being used in many applications such as tracking, signal processing, navigation and many more. Kalman filter based techniques were applied to inverse problem of electrocardiography by a few researchers [73, 82, 119, 120]. Before giving discrete Kalman filter and smoother steps, predicted estimate and the covariance of the estimation error of $x_{k|k-1}$ and $x_{k|k}$ are given as follows:

$$\hat{x}_{k|k-1} = \mathbf{E}[x_k|y_1, y_2, \ldots, y_{k-1}] \tag{3.6}$$

$$P_{k|k-1} = \mathbf{E}[(x_k - x_{k|k-1})(x_k - x_{k|k-1})^T] \tag{3.7}$$

$$P_{k|k} = \mathbf{E}[(x_k - x_{k|k})(x_k - x_{k|k})^T] \tag{3.8}$$

Discrete Kalman filter and smoother steps are as follows (Detailed discussion can be found in [121]):

Step 1. Initialization

For k=1, initialize x_k and P_k

- $\hat{x}_{1|1} = \mathbf{E}[x_1] = \bar{x}$

- $P_{1|1} = \mathbf{E}[(x_1 - \hat{x}_{1|1})(x_1 - \hat{x}_{1|1})^T] = \Sigma$

Step 2. Forward Recursion: Filtering

For k=2, ..., T do

- $\hat{x}_{k|k-1} = F\hat{x}_{k-1|k-1} \longrightarrow$ State Time Update

- $P_{k|k-1} = FP_{k-1|k-1}F^T + Q \longrightarrow$ State Covariance Time Update

- $K_k = P_{k|k-1}H^T(HP_{k|k-1}H^T + R)^{-1} \longrightarrow$ Kalman Gain

- $\hat{x}_{k|k} = \hat{x}_{k|k-1} + K_k(y_k - H\hat{x}_{k|k-1}) \longrightarrow$ State Measurement Update

- $P_{k|k} = (I - K_kH)P_{k|k-1} \longrightarrow$ State Covariance Measurement Update

After giving Kalman filter steps, our next step is Kalman smoother. In this study, we use **Rauch-Tung-Striebel Smoother** (RTS) [122]. RTS is very convenient approach for linear Gaussian models, as in our model.

RTS steps are given as follows (Detailed discussion can be found in [123]):

Step 3. Backward Recursion: Smoothing

For k=T-1, ..., 1 do

- $P_{k+1|k} = FP_{k|k}F^T + Q$

- $G_k = P_{k|k}F^T(P_{k+1|k})^{-1}$

- $\hat{x}_{k|T} = \hat{x}_{k|k} + G_k[\hat{x}_{k+1|T} - F\hat{x}_{k|k}]$

3.2.3 Regularized Kalman Filter and Smoother

As mentioned before, the forward transfer matrix H has high condition number (in our case, the condition number of H is $cond(H) \approx 7.4173 \times 10^{12}$) and is an ill-conditioned matrix. Ill-conditioned nature of the forward transfer matrix may cause instability in ECGI solutions. For stable solutions, H matrix needs to be regularized. In this section, we use Schulze *et al.*'s [78] approach and modify Kalman filter equations that are used in MLIF and MAPIF algorithms to improve these algorithms' performances. In their article, Schulze *et al.* apply second order Tikhonov regularization to the forward transfer matrix and find second order Tikhonov pseudo-inverse of the forward transfer matrix. Then, they modify Kalman gain and Kalman filter measurement update equations to integrate Tikhonov regularization.

We begin with rewriting general Tikhonov regularization solution equation (3.3):

$$\hat{x} = \underbrace{(H^TH + \lambda^2\mathcal{L}^T\mathcal{L})^{-1}H^T}_{H^\dagger}y \qquad (3.9)$$

where $H^\dagger$ is called second order Tikhonov pseudo-inverse of H and $\mathcal{L}$ is surface Laplacian operator. We find the regularization parameter λ by using L-curve method. Next, we replace Kalman gain K with $\tilde{K}_k H^{-1}$ in Kalman gain equation $K_k = P_{k|k-1}H^T(HP_{k|k-1}H^T + R)^{-1}$:

$$\tilde{K}_k H^{-1} = P_{k|k-1}H^T(HP_{k|k-1}H^T + R)^{-1} \tag{3.10}$$

where $\tilde{K}$ is the new Kalman gain. $\tilde{K}$ can be derived as follows:

$$
\begin{aligned}
\tilde{K}_k &= P_{k|k-1}H^T(HP_{k|k-1}H^T + R)^{-1}H \\
&= P_{k|k-1}H^T(H^{-1}HP_{k|k-1}H^T + H^{-1}R)^{-1} \\
&= P_{k|k-1}H^T(P_{k|k-1}H^T + H^{-1}R)^{-1} \\
&= P_{k|k-1}(P_{k|k-1}H^T(H^T)^{-1} + H^{-1}R(H^T)^{-1})^{-1} \\
&= P_{k|k-1}(P_{k|k-1} + H^{-1}R(H^{-1})^T)^{-1} \\
&= P_{k|k-1}(P_{k|k-1} + H^\dagger R(H^\dagger)^T)^{-1} \tag{3.11}
\end{aligned}
$$

Similarly, we replace K_k with $\tilde{K}_k H^{-1}$ in the state measurement update and state covariance measurement update equations:

$$
\begin{aligned}
\hat{x}_{k|k} &= \hat{x}_{k|k-1} + K_k(y_k - H\hat{x}_{k|k-1}) \\
&= \hat{x}_{k|k-1} + \tilde{K}_k H^{-1}(y_k - H\hat{x}_{k|k-1}) \\
&= \hat{x}_{k|k-1} + \tilde{K}_k H^\dagger y_k - \tilde{K}_k \hat{x}_{k|k-1} \tag{3.12}
\end{aligned}
$$

$$
\begin{aligned}
P_{k|k} &= (I - K_k H)P_{k|k-1} \\
&= P_{k|k-1} - \tilde{K}_k H^{-1}HP_{k|k-1} \\
&= P_{k|k-1} - \tilde{K}_k P_{k|k-1} \tag{3.13}
\end{aligned}
$$

We now have modified Kalman filter equations in terms of $\tilde{K}$ and $H^\dagger$.

<div align="center">

Modified Kalman Filter Equations

$$
\begin{array}{|c|}
\hline
\hat{x}_{k|k-1} = F\hat{x}_{k-1|k-1} \\
P_{k|k-1} = FP_{k-1|k-1}F^T + Q \\
\tilde{K}_k = P_{k|k-1}(P_{k|k-1} + H^\dagger R(H^\dagger)^T)^{-1} \\
\hat{x}_{k|k} = \hat{x}_{k|k-1} + \tilde{K}_k H^\dagger y_k - \tilde{K}_k \hat{x}_{k|k-1} \\
P_{k|k} = P_{k|k-1} - \tilde{K}_k P_{k|k-1} \\
\hline
\end{array}
$$

</div>

In order to use Kalman filter and smoother, and regularized Kalman filter and smoother, the state-space parameters F, Q, R and, the initial state's mean and covariance $\hat{x}, \Sigma$ are needed. These parameters are found by using by using parameter estimation techniques.

3.2.4 Bayesian Maximum a Posteriori (BMAP)

In equation (3.1), we stated state-space formulation of the problem. Considering all states together, we rewrite the relation between the body surface potential measurements and epicardial potentials as follows:

$$y = Hx + v \tag{3.14}$$

Bayes' theorem states that posterior pdf of x given y can be found by using the following equation:

$$\underbrace{p(x \mid y)}_{\text{Posterior pdf}} = \frac{\overbrace{p(y \mid x)}^{\text{Likelihood}} \overbrace{p(x)}^{\text{Prior pdf}}}{\underbrace{\int_x p(y \mid x) P(x) dx}_{\text{Evidence}}} \tag{3.15}$$

Bayesian MAP estimation technique maximizes the posterior pdf of x given y. By maximizing the posterior pdf, we find the most probable value of x given observed data y. Maximization of the posterior pdf is given by the following equation:

$$\hat{x} = \underset{x}{\text{argmax}}\, p(x \mid y) = \underset{x}{\text{argmax}}\, \frac{p(y \mid x) p(x)}{p(y)} \tag{3.16}$$

Since $p(y)$ is just a scaling factor and does not depend on x, equation (3.16) simplifies to:

$$\hat{x} = \underset{x}{\text{argmax}}\, p(y \mid x) p(x) \tag{3.17}$$

or equivalently:

$$\hat{x} = \underset{x}{\text{argmax}}[ln\, p(y \mid x) + ln\, p(x)] \tag{3.18}$$

From the previous section, we know that:

- $p(y|x) \triangleq \mathcal{N}(y; Hx, R)$

- $p(x) \triangleq \mathcal{N}(x; \bar{x}, \Sigma)$

41

where $\hat{x} = E[x_k]$ and $\Sigma = E[(x_k - \hat{x}_k)(x_k - \hat{x}_k)^T] \ \forall \ k$.

To maximize equation (3.18), we take the derivative of that equation and find the root by setting the derivative equal to zero. After doing the necessary calculations, the details are given in Appendix C, $\hat{x}$ is found as follows:

$$\hat{x} = \left(H^T R^{-1} H + \Sigma^{-1} \right)^{-1} \left(H^T R^{-1} y + \Sigma^{-1} \bar{x} \right) \tag{3.19}$$

In order to use Bayesian maximum a posteriori technique, the state-space parameter R and, the state's mean and covariance $\hat{x}, \Sigma$ are needed. These parameters are found by using the training set data and the standard deviation of the measurement noise, as shown in section 3.4.4.

3.2.5 Relation Between BMAP and Tikhonov Regularization

We observe that Bayesian MAP method is equivalent to Tikhonov regularization under the following assumptions:

- $R = \beta^2 I$

- $\Sigma = \gamma^2 I$

- $\bar{x} = 0$

Rewriting the equation (3.19) by replacing R, Σ and $\hat{x}$ yields:

$$\hat{x} = \left(\frac{1}{\beta^2} H^T H + \frac{1}{\gamma^2} I \right)^{-1} \left(\frac{1}{\beta^2} H^T y \right) \tag{3.20}$$

$$\hat{x} = \left(\frac{\beta^2}{\beta^2} \frac{1}{\beta^2} H^T H + \frac{\beta^2}{\beta^2} \frac{1}{\gamma^2} I \right)^{-1} \left(\frac{1}{\beta^2} H^T y \right)$$

$$\hat{x} = \left(H^T H + \frac{\beta^2}{\gamma^2} I \right)^{-1} H^T y \tag{3.21}$$

Comparing equation (3.21) with (3.3), we conclude that the regularization parameter λ is equal to $\frac{\beta}{\gamma}$. By this way, the regularization parameter is found without using **L-curve** method.

3.3 Parameter Estimation Techniques

In the state-space formulation of the problem, there are five unknown parameters, namely, $\bar{x}, \Sigma, F, Q, R$. These parameters need to be estimated in order to apply inverse electrocardiography algorithms in the previous sections. In this thesis, Maximum Likelihood (ML) Estimation and Maximum a Posteriori (MAP) Estimation methods are used to estimate the unknown parameters.

3.3.1 Maximum Likelihood Estimation

Parameter estimation problems are usually solved by maximum likelihood estimation. Parameter estimation based on ML method was used extensively in speech signal processing literature [124–127]. In the literature of inverse electrocardiography, ML method was used by El-Jakl *et al.* [73]. El-Jakl *et al.* used maximum likelihood estimation to estimate the state transition matrix, the process and the measurement covariance matrices.

Maximum likelihood estimation finds the best estimate of unknown parameter set $\Theta = \{\bar{x}, \Sigma, F, Q, R\}$ value which maximizes the joint likelihood function so that the observed data is the most probable.

We start by selecting L experiments from epicardial potential database and simulate body surface potentials for each experiment. Then, we compose a training set with epicardial potentials $X = \{x_{1:T}^{\ell}\}_{\ell=1}^{L}$ and simulated body surface potentials $Y = \{y_{1:T}^{\ell}\}_{\ell=1}^{L}$. Mathematically, we find the the value of the parameter set as follows:

$$\hat{\Theta} = \underset{\Theta}{\operatorname{argmax}} \underbrace{p(X, Y \mid \Theta)}_{\Pi(\Theta)} \qquad (3.22)$$

where $\Pi(\Theta)$ is the joint likelihood function. It is usually easier to work with natural logarithm, since there is no difference between maximization of likelihood function and log-likelihood function, the equation (3.22) can be rewritten as follows:

$$\hat{\Theta} = \underset{\Theta}{\operatorname{argmax}} \, ln\Pi(\Theta) \qquad (3.23)$$

where

$$\Pi(\Theta) = \prod_{\ell=1}^{L} p(x_{1:T}^{\ell}, y_{1:T}^{\ell} \mid \Theta) \qquad (3.24)$$

43

under the assumption of independent experiments. Assuming first Markov property [128], $\Pi(\Theta)$ is written as follows:

$$\Pi(\Theta) = \prod_{\ell=1}^{L} \left(p(x_1^\ell|\Theta) \prod_{k=1}^{T} p(y_k^\ell|x_k^\ell, \Theta) \prod_{k=2}^{T} p(x_k^\ell|x_{k-1}^\ell, \Theta) \right) \qquad (3.25)$$

We take the natural logarithm of $\Pi(\Theta)$ and plug the parameter set components into equation (3.25):

$$
\begin{aligned}
ln\Big(\Pi(\Theta)\Big) &= \sum_{\ell=1}^{L} ln\ p(x_1^\ell|\Theta) + \sum_{\ell=1}^{L}\sum_{k=1}^{T} ln\ p(y_k^\ell|x_k^\ell, \Theta) + \sum_{\ell=1}^{L}\sum_{k=2}^{T} ln\ p(x_k^\ell|x_{k-1}^\ell, \Theta) \\
&= \sum_{\ell=1}^{L} ln\ p(x_1^\ell|\bar{x}, \Sigma) + \sum_{\ell=1}^{L}\sum_{k=1}^{T} ln\ p(y_k^\ell|x_k^\ell, R) + \sum_{\ell=1}^{L}\sum_{k=2}^{T} ln\ p(x_k^\ell|x_{k-1}^\ell, F, Q)
\end{aligned}
$$

$$(3.26)$$

where

- $p(x_1^\ell|\bar{x}, \Sigma) \sim \mathcal{N}(x_1^\ell; \bar{x}, \Sigma)$

- $p(y_k^\ell|x_k^\ell, R) \sim \mathcal{N}(y_k^\ell; Hx_k^\ell, R)$

- $p(x_k^\ell|x_{k-1}^\ell, F, Q) \sim \mathcal{N}(x_k^\ell; Fx_{k-1}^\ell, Q)$

To find the parameter set components $\{\bar{x}, \Sigma, F, Q, R\}$, keeping in the mind that the log-likelihood function is concave function of $\bar{x}$, Σ^{-1}, F, Q^{-1} and R^{-1}, i.e., the problem is convex, [129], we take derivative of $ln(\Pi(\Theta))$ with respect to each component and obtain the roots by equating it to zero. Detailed discussion on how we find the parameter set components is given in Appendix A.

We summarize the results below:

Summary of ML Approach Based Estimated Parameters

$$\hat{\bar{x}} = \frac{1}{L}\sum_{\ell=1}^{L} x_1^\ell$$

$$\hat{\Sigma} = \frac{1}{L}\sum_{\ell=1}^{L}(x_1^\ell - \bar{x})(x_1^\ell - \bar{x})^T$$

$$\hat{R} = \frac{1}{LT}\sum_{\ell=1}^{L}\sum_{k=1}^{T}(y_k^\ell - Hx_k^\ell)(y_k^\ell - Hx_k^\ell)^T$$

$$\hat{F} = \left[\sum_{\ell=1}^{L}\sum_{k=2}^{T}x_k^\ell(x_{k-1}^\ell)^T\right] \cdot \left[\sum_{\ell=1}^{L}\sum_{k=2}^{T}x_{k-1}^\ell(x_{k-1}^\ell)^T\right]^{-1}$$

$$\hat{Q} = \frac{1}{L(T-1)}\sum_{\ell=1}^{L}\sum_{k=2}^{T}(x_k^\ell - Fx_{k-1}^\ell)(x_k^\ell - Fx_{k-1}^\ell)^T$$

3.3.2 Maximum a Posteriori Estimation

ML estimation over-fits the training set data and this causes poor performance when the test data and the training set data come from different physiological models [127]. Therefore, instead of ML, we propose MAP based parameter estimation algorithm to estimate the parameter set $\Theta = \{\bar{x}, \Sigma, F, Q, R\}$ in this section.

We begin with writing Bayes' general formula:

$$p(\Theta \mid X, Y) = \frac{p(X, Y \mid \Theta)p(\Theta)}{p(X, Y)} \tag{3.27}$$

where X and Y are epicardial potentials and body surface potentials respectively, which were defined in section 3.3.1. In MAP inference step, we find the estimated value of the parameter set $\hat{\Theta}$ which maximizes the posterior pdf $p(\Theta \mid X, Y)$. Mathematically, the estimated value of the parameter set is given as follows:

$$\hat{\Theta} = \underset{\Theta}{\operatorname{argmax}}\, p(X, Y \mid \Theta)p(\Theta) \tag{3.28}$$

where we dropped the term $p(X, Y)$ since it does not depend on Θ. Equation (3.28) is equivalent to the following equation:

$$\hat{\Theta} = \underset{\Theta}{\operatorname{argmax}}[ln\,\underbrace{p(X, Y \mid \Theta)}_{\Pi(\Theta)} + ln\,p(\Theta)] \tag{3.29}$$

45

where $\Pi(\Theta)$ was defined in equation (3.25).

In this study, we divide the parameter set into two subsets $\Theta = \{\Theta_1, \Theta_2\}$ where $\Theta_1 = \{\bar{x}, \Sigma, R\}$ and $\Theta_2 = \{F, Q\}$. If we assume Θ_1 and Θ_2 are independent, the prior pdf is written as follows:

$$p(\Theta) = p(\Theta_1)p(\Theta_2) \tag{3.30}$$

This work assumes $p(\Theta_1)$ as non-informative prior. Under this assumption, equation (3.29) can be written as follows:

$$\hat{\Theta} = \underset{\Theta}{\operatorname{argmax}}[ln\ \Pi(\Theta) + ln\ p(F, Q)] \tag{3.31}$$

To proceed further, we need to choose the joint prior distribution $p(F, Q)$ or equivalently $p(F|Q)$ and $p(Q)$ since $p(F, Q) = p(F|Q)p(Q)$. In this study, we work with conjugate prior distributions since when conjugate prior distributions are used, it is easy to derive posterior in closed form analytically [130]. The prior distribution $p(F|Q)$ is assumed to be matrix normal distribution and given as follows:

$$p(F \mid Q) \sim \mathcal{N}(F; \zeta, \Phi \otimes Q) \tag{3.32}$$

$$p(F \mid Q) = (2\pi)^{-\frac{M^2}{2}}|\Phi|^{-\frac{M}{2}}|Q|^{-\frac{M}{2}}exp\left(-\frac{1}{2}tr\left[\Phi^{-1}(F-\zeta)^T Q^{-1}(F-\zeta)\right]\right)$$

$$\propto |\Phi|^{-\frac{M}{2}}|Q|^{-\frac{M}{2}}exp\left(-\frac{1}{2}tr\left[\Phi^{-1}(F-\zeta)^T Q^{-1}(F-\zeta)\right]\right) \tag{3.33}$$

where $\otimes$ is Kronecker product operator, ζ is mean matrix, Φ and Q are left and right covariance matrices respectively. Assuming zero mean matrix, equation (3.33) reduces to:

$$p(F \mid Q) \propto |\Phi|^{-\frac{M}{2}}|Q|^{-\frac{M}{2}}exp\left(-\frac{1}{2}tr\left[\Phi^{-1}F^T Q^{-1}F\right]\right) \tag{3.34}$$

The prior distribution $p(Q)$ is assumed to be inverse Wishart distribution and given as follows:

$$p(Q) \sim \mathcal{W}^{-1}(Q; \Psi, v) \tag{3.35}$$

$$p(Q) \propto |Q|^{-\frac{v+M+1}{2}}exp\left(-\frac{1}{2}tr\left[Q^{-1}\Psi\right]\right) \quad \text{(See [130] for full distribution, page 110)} \tag{3.36}$$

where Ψ is scale matrix and v is degrees of freedom.

Putting $p(F|Q)$ and $p(Q)$ together, we find $p(F, Q)$ as follows:

$$p(F, Q) \propto |\Phi|^{-\frac{M}{2}} |Q|^{-\frac{v+2M+1}{2}} exp\left(-\frac{1}{2} tr\left[\Phi^{-1} F^T Q^{-1} F + Q^{-1} \Psi \right] \right) \qquad (3.37)$$

Note that we omitted the constants in the full distributions of both $p(F|Q)$ and $p(Q)$ since the constants have no significance in the solution.

After finding the joint prior distribution, we get back the posterior distribution maximization. Replacing $p(F, Q)$ with the result above in equation (3.29) yields:

$$\hat{\Theta} = \underset{\Theta}{argmax}[ln \, \Pi(\Theta) + ln \, p(F, Q)]$$

$$= \underset{\Theta}{argmax} \left[ln \, \Pi(\Theta) - \frac{M}{2} ln|\Phi| + \frac{v+2M+1}{2} ln|Q^{-1}| - \frac{1}{2} tr\left(\Phi^{-1} F^T Q^{-1} F + Q^{-1} \Psi \right) \right]$$

$$(3.38)$$

As we mentioned before, we take $\Theta_1 = \{\bar{x}, \Sigma, R\}$ as non-informative prior, therefore the estimated values $\hat{\bar{x}}$, $\hat{\Sigma}$ and $\hat{R}$ are the same as in ML estimation. So, we only need to derive $\hat{F}$ and $\hat{Q}$ formulas. To do this, keeping in the mind that equation (3.29) is concave function of $\bar{x}$, Σ^{-1}, F, Q^{-1} and R^{-1}, i.e., the problem is convex, [129], we take the derivative of equation (3.38) with respect to F and Q and then set the derivatives equal to zero.

Detailed discussion on how we find the sub-parameter set $\Theta_2 = \{F, Q\}$ components is given in Appendix B.

We summarize the results below:

<div align="center">Summary of MAP Approach Based Estimated Parameters</div>

$$\hat{\bar{x}} = \frac{1}{L} \sum_{\ell=1}^{L} x_1^{\ell}$$

$$\hat{\Sigma} = \frac{1}{L} \sum_{\ell=1}^{L} (x_1^{\ell} - \bar{x})(x_1^{\ell} - \bar{x})^T$$

$$\hat{R} = \frac{1}{LT} \sum_{\ell=1}^{L} \sum_{k=1}^{T} (y_k^{\ell} - Hx_k^{\ell})(y_k^{\ell} - Hx_k^{\ell})^T$$

$$\hat{F} = \Big[\sum_{\ell=1}^{L} \sum_{k=2}^{T} x_k^{\ell}(x_{k-1}^{\ell})^T \Big] \Big[\sum_{\ell=1}^{L} \sum_{k=2}^{T} \big(x_{k-1}^{\ell}(x_{k-1}^{\ell})^T \big) + \Phi^{-1} \Big]^{-1}$$

$$\Phi^{-1} = \alpha \sum_{\ell=1}^{L} \sum_{k=2}^{T} x_{k-1}^{\ell}(x_{k-1}^{\ell})^T$$

$$\hat{Q} = \frac{\sum_{\ell=1}^{L} \sum_{k=2}^{T} (x_k^{\ell} - Fx_{k-1}^{\ell})(x_k^{\ell} - Fx_{k-1}^{\ell})^T + \big(F^T \Phi^{-1} F + \Psi^T \big)}{L(T-1) + (v + 2M + 1)}$$

$$\Psi = \frac{1}{v} I$$

$$v = L(T-1)$$

3.4 Application of the Algorithms to The Problem

In section, the details of the algorithms that are used in this study are given.

3.4.1 Tikhonov Regularization

1: Load test beat $\rightarrow x^{\ell=1}$

2: Find the measurement matrix $\rightarrow y = Hx^{\ell=1} + n$

3: Perform singular value decomposition of $H \rightarrow$ [U,S,V] = svd(A)

4: Find λ by using L-curve method

5: $\hat{x} = \text{Tikhonov}(U, S, V, y, \lambda) \rightarrow$ Tikhonov 0 (See Section 3.2.1 for how to calculate Tikhonov function)

<div align="center">Algorithm 1: Tikhonov Regularization Algorithm</div>

3.4.2 Maximum Likelihood Inference & Filtering (MLIF) and Maximum a Posteriori Inference & Filtering (MAPIF)

1: Load test beat $\rightarrow x^{\ell=1}$

2: $y = Hx^{\ell=1} + n$

3: **for** $\ell = 2, 3, ...L$ (Include $\ell = 1$ for Scenario 1)

Find $\hat{x}, \Sigma, F, R, Q$ using formulas that are provided in section 3.3.1 $\rightarrow$ MLIF

Find $\hat{x}, \Sigma, F, R, Q$ using formulas that are provided in section 3.3.2 $\rightarrow$ MAPIF

4: Apply Kalman Filter and Smoother (details are given in section 3.2.2) $\rightarrow \hat{x}$

Algorithm 2: MLIF and MAPIF Algorithms

3.4.3 Regularized Maximum Likelihood Inference & Filtering (RMLIF) and Regularized Maximum a Posteriori Inference & Filtering (RMAPIF)

1: Load test beat $\rightarrow x^{\ell=1}$

2: $y = Hx^{\ell=1} + n$

3: **for** $\ell = 2, 3, ...L$ (Include $\ell = 1$ for Scenario 1)

Find $\hat{x}, \Sigma, F, R, Q$ using formulas that are provided in section 3.3.1 $\rightarrow$ RMLIF

Find $\hat{x}, \Sigma, F, R, Q$ using formulas that are provided in section 3.3.2 $\rightarrow$ RMAPIF

4: Apply Regularized Kalman Filter and Smoother (details are given in section 3.2.3) $\rightarrow \hat{x}$

Algorithm 3: RMLIF and RMAPIF Algorithms

3.4.4 Bayesian Maximum a Posteriori (BMAP)

1: Load test beat $\rightarrow x^{\ell=1}$

2: Compose training set $\rightarrow x_{train} = \begin{bmatrix} x^{\ell=2} & x^{\ell=3} & ... & x^{\ell=L} \end{bmatrix}$ (We used Serina-gaoglu *et al.*'s [97] approach to make use of multiple measurements)

3: Find the measurement matrix $\rightarrow y = Hx^{\ell=1} + n$

4: Find the mean and the covariance matrix of $x_{train} \rightarrow \bar{x} = \text{mean}(x_{train})$, $\Sigma = \text{cov}(x_{train})$

5: Find the covariance matrix of added noise $\rightarrow R = \sigma_n^2 I$

6: $\hat{x} = \text{BayesianMAP}(H, \Sigma, \bar{x}, y, R)$

(See Section 3.2.4 for how to calculate BayesianMAP function)

Algorithm 4: Bayesian MAP Algorithm

CHAPTER 4

RESULTS

In this chapter, we investigate the performances of our proposed algorithms. To do this, first, we explain the dataset used for testing the algorithms in this study. Then, we compare the performances of the algorithms by using the dataset.

4.1   Test Data

In this study, University of Utah Nora Eccles Harrison Cardiovascular Research and Training Institute's (CVRTI) epicardial potential database was used [131]. Epicardial potentials were recorded from dog hearts by conducting experiments. To mimic the real physiological situation, the dog's heart was perfused with another dog's circulatory system and placed within a torso shaped tank filled with electrolytic solution (500 $\Omega \cdot$ cm) in the correct anatomical position [132]. Nylon sock electrode with silver wires was placed onto the heart to measure epicardial potentials. Total number of measurement locations on the heart was 490, and the sampling rate was 1000 samples/sec. In the experiments, the heart was paced from different locations. We first classified the experiments with respect to their initial stimulation points. To do this, we examined the experiments and determined their stimulation points on the heart by using *Map3d* software [133]. We divided the heart's anterior, posterior and lateral surfaces into 4 regions (see Figure 4.2). Then, we chose the experiments whose stimulation points fall into these regions. The total number of chosen experiments was 28.
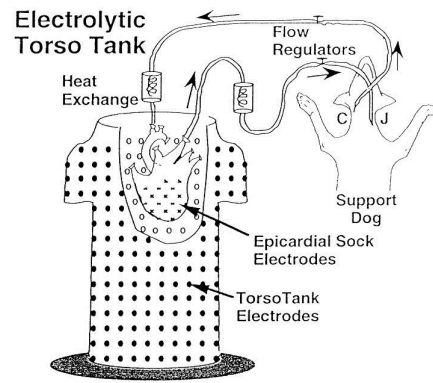
Figure 4.1: Experimental setup of epicardial potential data acquisition system [134]

(a) The heart's anterior view segmentation

(b) The heart's posterior view segmentation

(c) The heart's lateral view segmentation
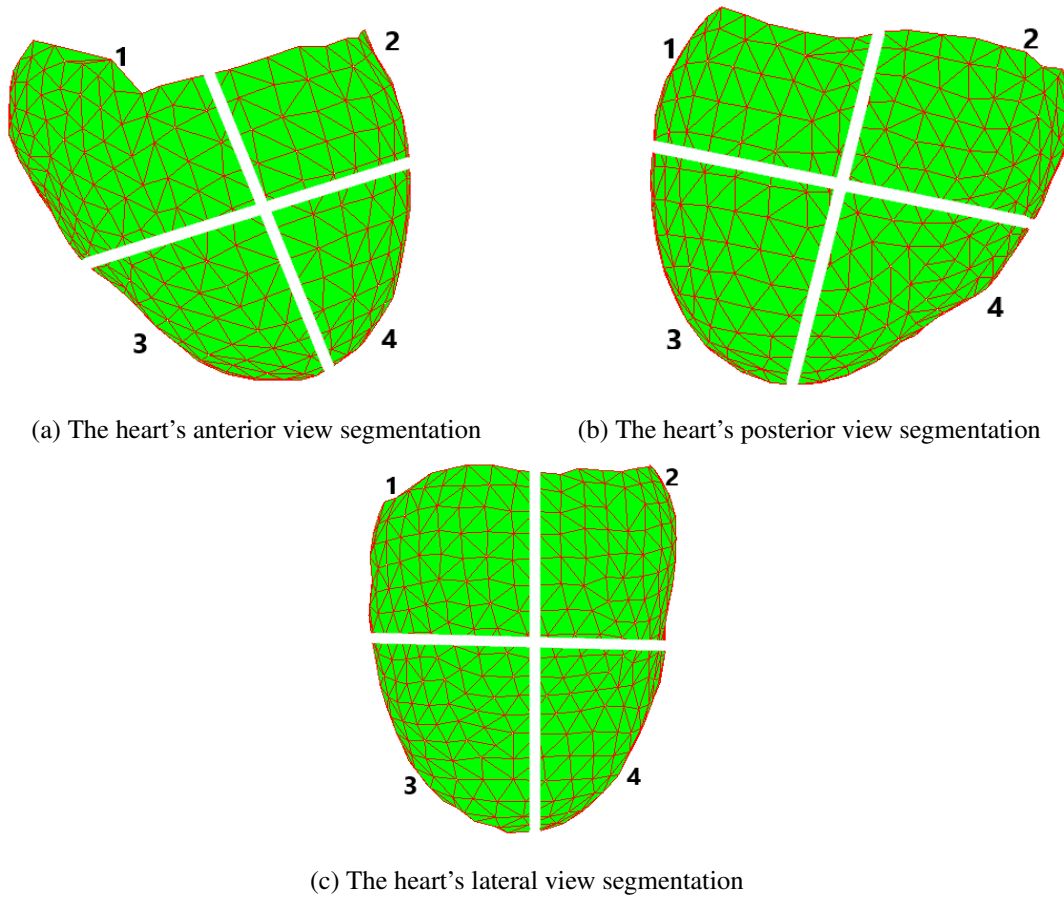
Figure 4.2: The heart segmentation
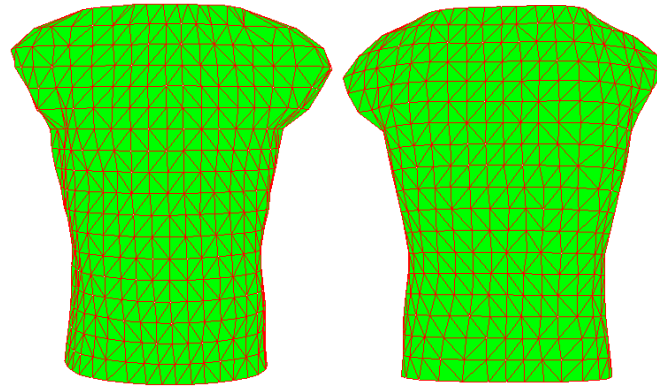
(a) The torso's front view seg-
mentation

(b) The torso's back view seg-
mentation

Figure 4.3: The torso segmentation

We gave a number to each region (Figure 4.2) starting from left to right and top to bottom. We used experiments from Posterior 1, Posterior 2, Posterior 3 and Posterior 4 regions. We used only the QRS intervals of the selected experiments.

We did not have access to the measured body surface potentials, therefore we calculated them by simulation in this study. To find the body surface potentials, first, the forward problem should be solved. We solved equation (2.2) by employing Dirichlet (equation (2.4)) and Neumann (equation (2.3)) boundary conditions. In order to solve equation (2.2), we used Green's second identity under the assumption of no current sources exist between the heart and torso surfaces. The resulting integral equation was then discretized by representing the heart and the body surfaces in triangularized form (see Figures 4.2 and 4.3). By utilizing BEM, the discretized equations were solved and the forward transfer matrix was found [21]. In the forward problem solution, the region between the heart and the torso was assumed to be piecewise homogeneous, i.e., the lungs were included in the geometry.

To find the body surface potentials, we multiplied the epicardial potentials by the forward transfer matrix and then added independent, identically distributed Gaussian noise (30 dB SNR unless stated otherwise). The epicardial potentials were collected from 490 measurement points on the heart surface as shown in Figure 4.4.

The forward transfer matrix used in our study provides electrical potentials at 192 points on the body surface, i.e., the forward matrix size is 192 by 490. Using 192

measurement points is enough to represent nearly all signal information on the body surface as stated in section 2.5.3. The forward transfer matrix translates the epicardial potentials to the body surface potentials with electrode locations as shown in Figure 4.5.

The steps for finding the body surface potentials can be summarized as follows:

1. The heart and the torso geometries, i.e., triangle meshes, were available in this study.

2. Using these geometries, a BEM solver was used to generate the forward transfer matrix.

3. The epicardial potentials were multiplied by the forward transfer matrix and independent, identically distributed Gaussian noise is added to the result. These noisy potentials represent simulated body surface potentials.
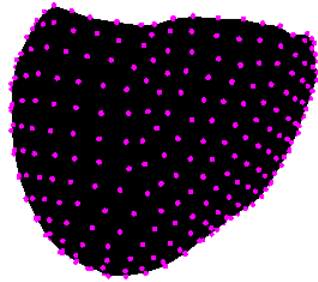
Figure 4.4: The location of 490 nodes on the heart surface

(a) Front view   (b) Back view
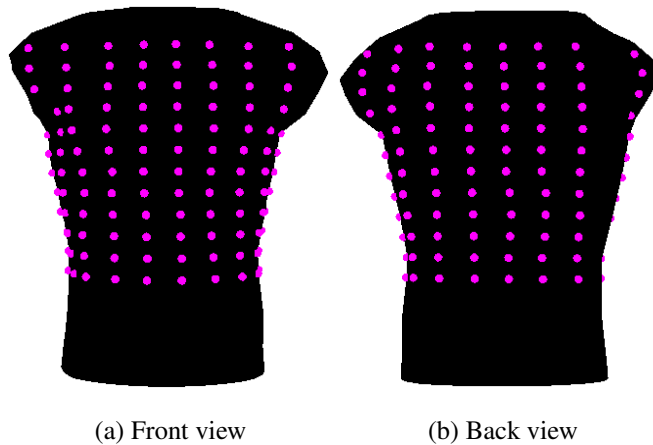
Figure 4.5: 192 lead-set configuration

4.2 Comparison Methods

We use quantitative methods and visualization to assess the performances of the proposed algorithms in this study. Quantitative methods consist of correlation coefficient (CC) and relative difference measurement star (RDMS). CC and RDMS are defined as follows:

$$CC_{x,\hat{x}}(k) = \frac{M \sum_{j=1}^{M} x_k(j)\hat{x}_k(j) \left(\sum_{j=1}^{M} x_k(j) \right) \left(\sum_{j=1}^{M} \hat{x}_k(j) \right)}{\sqrt{\left[M \sum_{j=1}^{M} x_k^2(j) - \left(\sum_{j=1}^{M} x_k(j) \right)^2 \right] \left[M \sum_{j=1}^{M} \hat{x}_k^2(j) - \left(\sum_{j=1}^{M} \hat{x}_k(j) \right)^2 \right]}} \quad (4.1)$$

$$RDMS_{x,\hat{x}}(k) = \left\| \frac{\hat{x}_k}{\|\hat{x}_k\|} - \frac{x_k}{\|x_k\|} \right\| \quad (4.2)$$

where $\| \cdot \|$ is the L2 norm, M is the number of epicardial nodes, $\hat{x}_k$ is the estimated epicardial potential state vector and x_k is the real epicardial potential state vector at time k.

As it can be deduced by intuition, higher CC and lower RDMS values between the estimated epicardial potentials $\hat{x}$ and the real epicardial potentials x are the indications of better results. In this study, CC and RDMS values were calculated at each time instant, and the average and the standard deviation of CC and RDMS values were calculated over the time interval. These results will be compared with each other in the following sections.

We also want to assess the algorithms' performances in terms of the localization error of the initial stimulation. The localization error is the Euclidean distance between the earliest activation time location of the estimated epicardial potentials and the real epicardial potentials. To do this, we compare the activation times of estimated and real epicardial potentials. In order to find the activation times, there are two methods: temporal-only method and spatio-temporal method [135]. The temporal-only method defines the activation time moment as the moment of steepest voltage downslope (maximum derivative of potential $-dV/dt$) during the QRS region [135]. In the spatio-temporal method proposed by Erem *et al.* [136], the propagation pattern represented by the temporal activation times on the surface of the heart is smoothed by using second order Tikhonov regularization. Since the spatio-temporal based method works better in noisy electrograms, we used Erem *et al.*'s approach in this thesis. Besides comparing the activation time distributions, CC value of activation times is also calculated. Activation time vectors yield single CC value.

These quantitative comparison methods, CC, RDMS and localization error, are good but not enough since they do not provide any information on the propagation patterns of activation wave-fronts. These patterns can only be investigated visually, so we use *Map3d* software for inspection the propagation patterns visually [133]. Epicardial potential distributions are displayed on the heart's 3D geometry as equipotential map in *Map3d*. We compare the heart's activated regions and potential wave-front transitions of true and estimated epicardial potentials at different time instants visually by using *Map3d*. Furthermore, activation time isochrones are also displayed by using *Map3d* to visualize which region of the heart activated first.

4.3 Comparison Scenarios

To fully assess the performances of the algorithms used in this study, we proposed different scenarios. In all the scenarios, we composed different training sets for each scenario. By using the training set data, we found the unknown parameters in the state-space representation. Then, the estimated epicardial potentials were found by using Tikhonov 0, MLIF, RMLIF, MAPIF, RMAPIF and BMAP algorithms.

The training sets were constructed as follows:

- Scenario 1:

  - In scenario 1, the beat we used for simulating the measurements (i.e., the test beat) and the training set beats came from the same experiment (the same dog heart). The test beat was included in the training set.

- Scenario 2: Leave-One-Beat-Out Protocol [97]

  - In scenario 2, we used the same training set as in scenario 1, but excluded the test beat.

- Scenario 3: Leave-One-Experiment-Out Protocol [97]

  - In scenario 3, the test beat came from a different experiment (i.e., a different dog heart) than the experiments from which we obtained the training set beats.

For all the scenarios, 100 Monte Carlo runs were used to obtain the results. The average of all these 100 simulations was taken in each case.

Tikhonov 0 is applied independent of these scenarios and does not use the training set data. It uses only the test beat and the results are the same in each scenario. For the sake of completeness, we include the same results for each scenario in Tikhonov regularization.

4.4 Comparison of the Performances Under Moderate Noise Conditions

In this section, we investigate the performances of the proposed algorithms. The body surface potentials were simulated by using 30 dB SNR measurement noise. No geometric error was assumed in this section.

4.4.1 Quantitative Evaluation of Electrograms

CC and RDMS plots for all time instants are shown in Figure 4.7 and Figure 4.8. Mean and standard deviation of CC values, and mean and standard deviations of RDMS values are shown in Tables 4.1 and 4.2. Figure 4.6 is the bar chart representation of Tables 4.1 and 4.2.

	Scenario 1	Scenario 2	Scenario 3
Tikhonov	0.60±0.28	0.60±0.28	0.60±0.28
MLIF	0.99±0.02	0.88±0.10	0.66±0.23
RMLIF	0.99±0.02	0.88±0.11	0.68±0.21
MAPIF	0.97±0.03	0.91±0.12	0.72±0.19
RMAPIF	0.91±0.09	0.89±0.12	0.72±0.20
BMAP	0.82±0.18	0.79±0.19	0.64±0.26

Table 4.1: Mean and standard deviation of CC values for scenario 1, scenario 2 and scenario 3

	Scenario 1	Scenario 2	Scenario 3
Tikhonov	0.55±0.11	0.55±0.11	0.55±0.11
MLIF	0.11±0.05	0.31±0.06	0.58±0.19
RMLIF	0.09±0.04	0.30±0.06	0.56±0.15
MAPIF	0.17±0.06	0.24±0.07	0.49±0.07
RMAPIF	0.26±0.05	0.28±0.07	0.49±0.07
BMAP	0.35±0.10	0.38±0.11	0.53±0.09

Table 4.2: Mean and standard deviation of RDMS values for scenario 1, scenario 2 and scenario 3

Based on Table 4.1 and Table 4.2, and Figure 4.6, the following observations are made:

- Both MLIF and RMLIF methods' performances are degraded by approximately 33% when the training set is changed from scenario 1 to scenario 3.

- MAPIF and RMAPIF methods' performances are degraded by approximately 25% and 20%, respectively, when the training set is changed from scenario 1 to scenario 3.

- BMAP method's performance is degraded by approximately 22% when the training set is changed from scenario 1 to scenario 3.
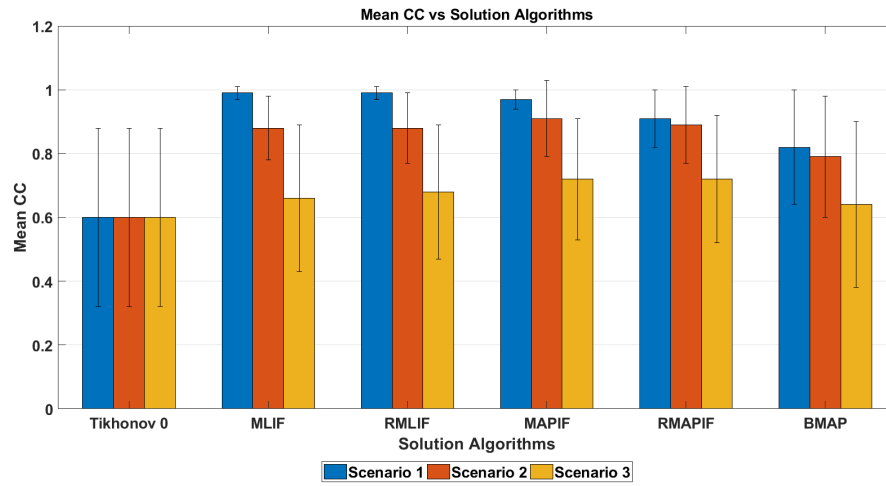
(a) Mean CC vs solution algorithms chart
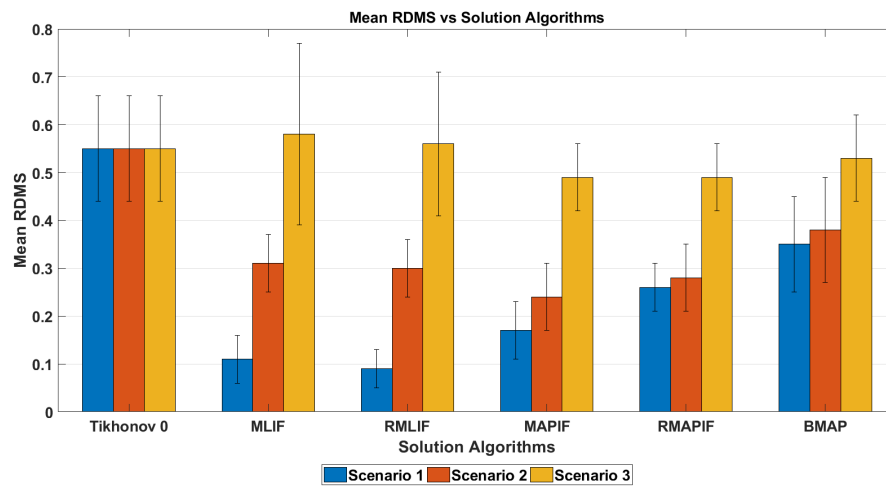
(b) Mean RDMS vs solution algorithms chart

Figure 4.6: Mean CC and mean RDMS vs solution algorithms charts
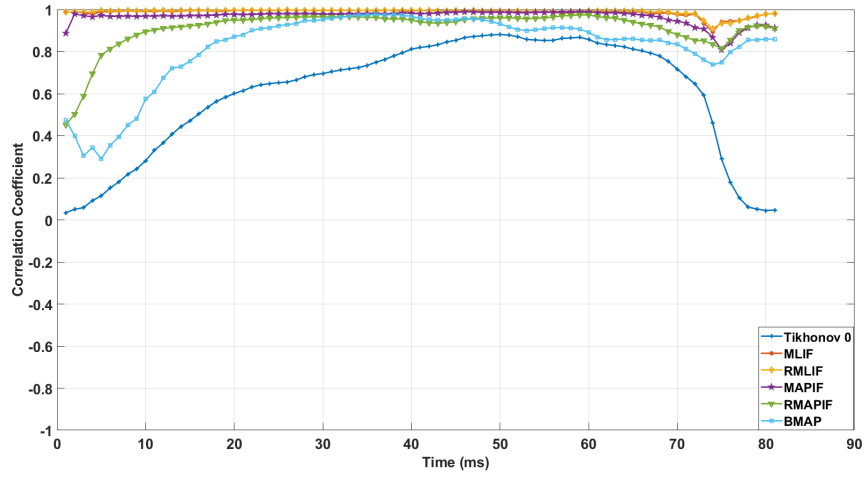
(a) CC vs time plot for scenario 1 under 30 dB SNR
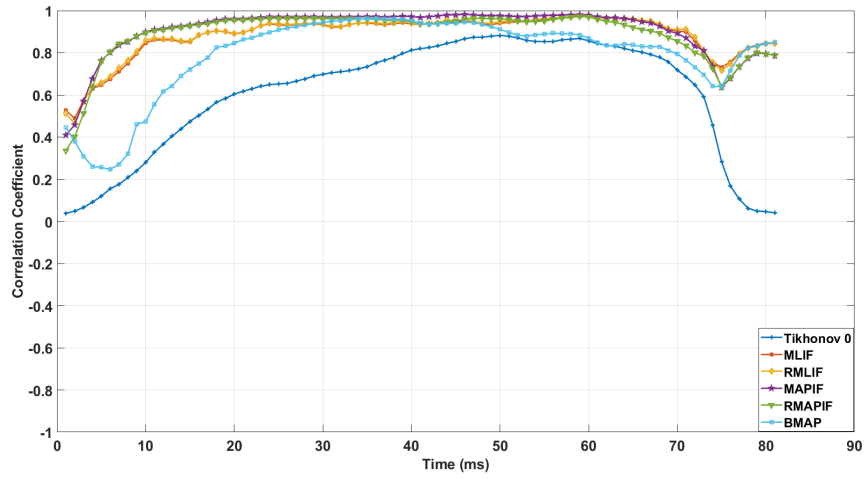
(b) CC vs time plot for scenario 2 under 30 dB SNR
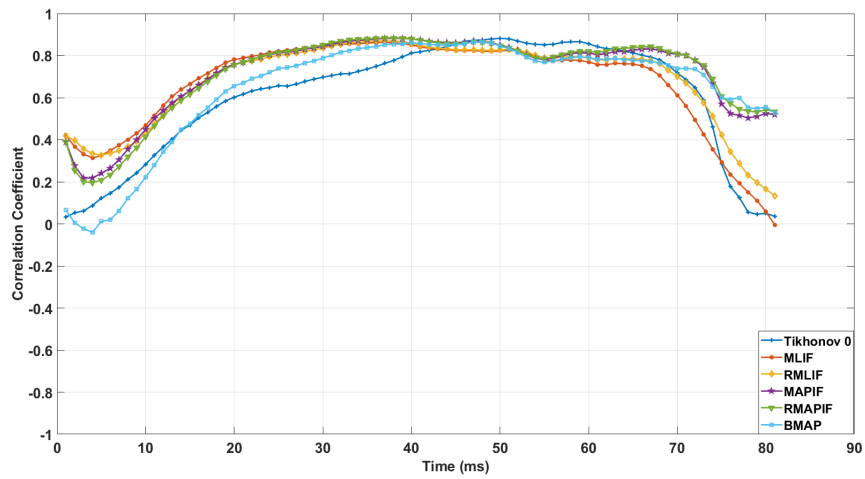
(c) CC vs time plot for scenario 3 under 30 dB SNR

Figure 4.7: CC vs time plots
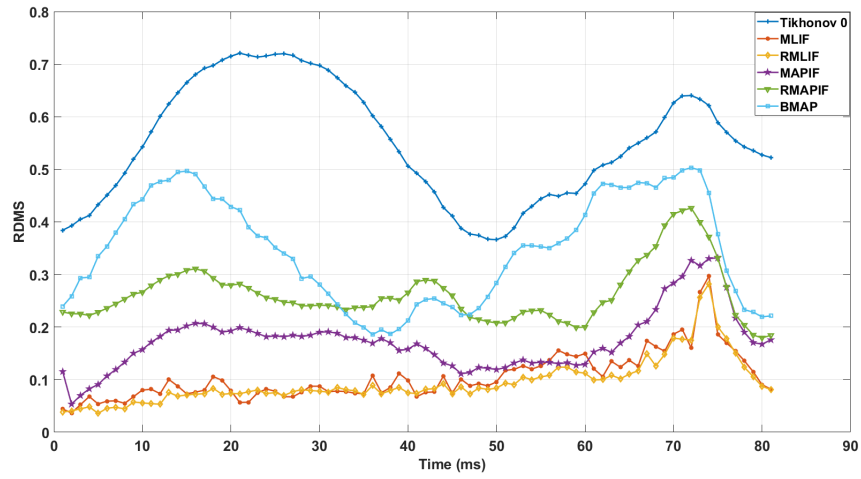
(a) RDMS vs time plot for scenario 1 under 30 dB SNR
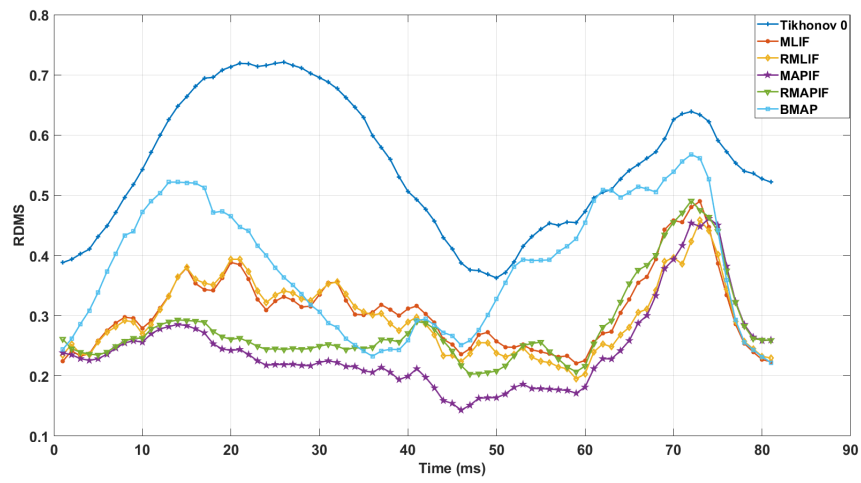
(b) RDMS vs time plot for scenario 2 under 30 dB SNR
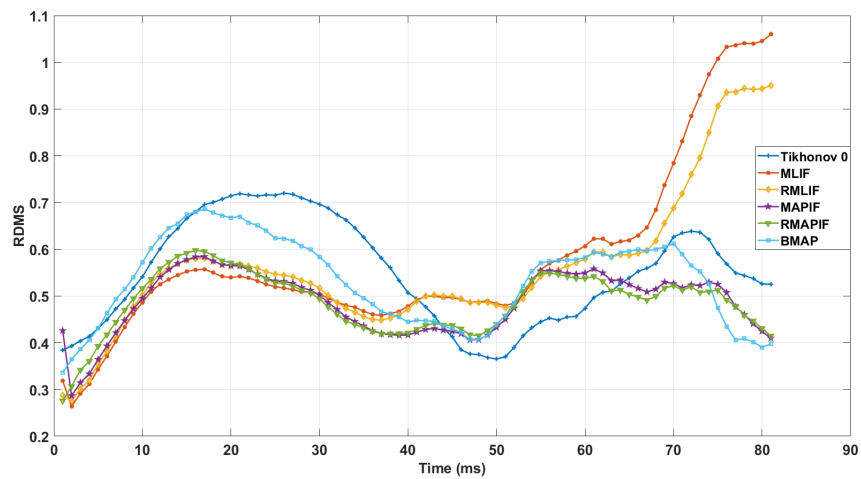
(c) RDMS vs time plot for scenario 3 under 30 dB SNR

Figure 4.8: RDMS vs time plots

In scenario 1, based on the CC and RDMS plots in Figure 4.7a and Figure 4.8a, the following observations are made:

- RMLIF and MLIF algorithms show almost the same performances, whereas RMLIF's performance is slightly better.

- Until 20 ms, MAPIF algorithm's performance is higher than RMAPIF algorithm. After 20 ms, MAPIF and RMAPIF algorithms' performances are close to each other.

- Between 25 ms and 50 ms, BMAP algorithm's performance is very close to RMAPIF algorithm. However, out of 25-50 ms interval, it has second worst performance.

- Tikhonov 0 algorithm has the worst performance among all the solution algorithms.

In scenario 2, based on the CC and RDMS plots in Figure 4.7b and Figure 4.8b, the following observations are made:

- Until 40 ms, MAPIF and RMAPIF algorithms show almost the same performances, but after 40 ms MAPIF algorithm outperforms RMAPIF and the other algorithms until 75 ms.

- RMLIF and MLIF algorithms show almost the same performances, whereas RMLIF's performance is slightly better.

- Between 30 ms and 50 ms, BMAP algorithm's performance is very close to the other algorithms. However, out of 30-50 ms interval, it has second worst performance.

- Tikhonov 0 algorithm has the worst performance among all the solution algorithms.

In scenario 3, based on the CC and RDMS plots in Figure 4.7c and Figure 4.8c , the following observations are made:

- Until 60 ms, ML and MAP based algorithms show similar performances. After 60 ms, the performances of MLIF and RMLIF are degraded rapidly.

- Until 40 ms, BMAP algorithm's performance is low. After 40 ms, BMAP shows similar performance with MAPIF and RMAPIF algorithms.

- Except the interval between 45 ms and 65 ms, Tikhonov 0 algorithm has the worst performance among all the solution algorithms.

- In general, MAPIF and RMAPIF algorithms outperform the other algorithms.

4.4.2 Isopotential Epicardial Maps

True and reconstructed epicardial distributions on the heart surface, viewed from posterior region, for scenario 1, scenario 2 and scenario 3 are shown in Figures 4.9 - 4.11.

Based on Figures 4.9 - 4.11, the following observations are made:

- Tikhonov 0 introduces smoothing effect to the solution and this can be seen in Figures 4.9b - 4.11b.

- ML based algorithms over-fit the training set data, hence MLIF and RMLIF are more sensitive to the training set data as compared to MAP based algorithms. As can be seen in Figure 4.11c and Figure 4.11d, the wave-fronts are more distracted as compared to MAP based algorithms when the training set data is not good.

- MAP based algorithms MAPIF and RMAPIF are less sensitive to the training set data as compared to ML based algorithms.

- BMAP is directly related to the training set data, hence it is more sensitive to the training set data as compared to ML and MAP based algorithms.
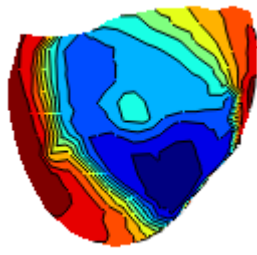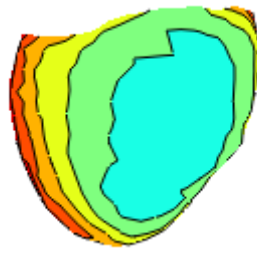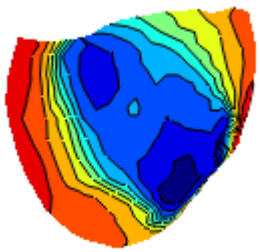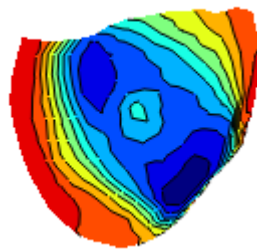
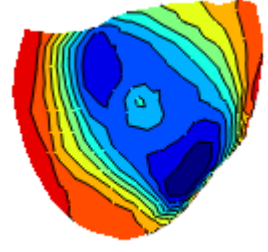(a) True   (b) Tikhonov 0 (CC = 0.73)   (c) MLIF (CC = 0.99)
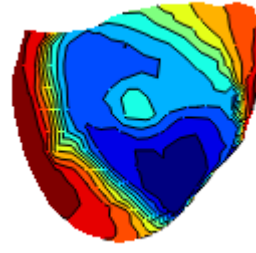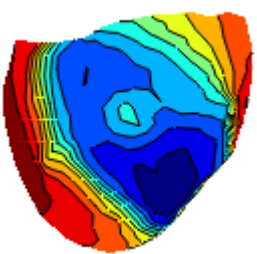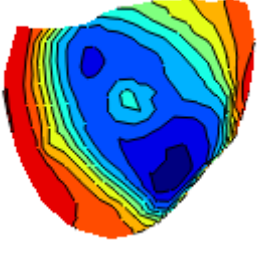
(d) RMLIF (CC = 0.99)   (e) MAPIF (CC = 0.98)   (f) RMAPIF (CC = 0.96)
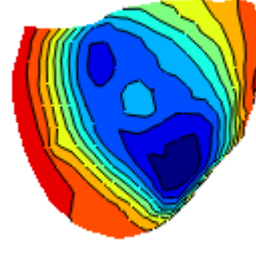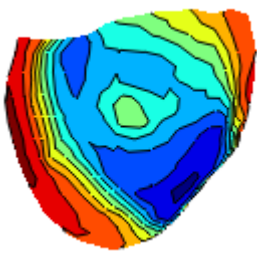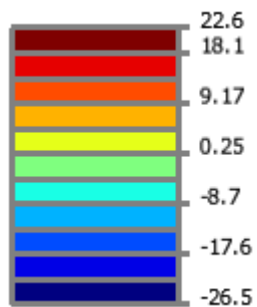
(g) BMAP (CC = 0.97)   (h) Legend

Figure 4.9: Real and estimated epicardial distributions for scenario 1 under 30 dB SNR at t = 35 ms
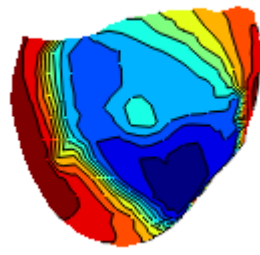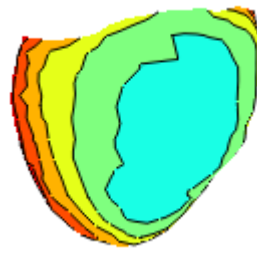
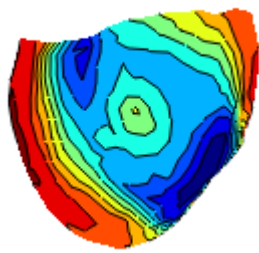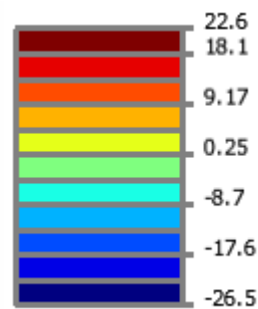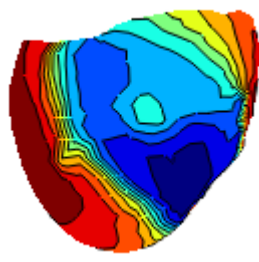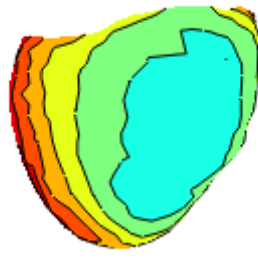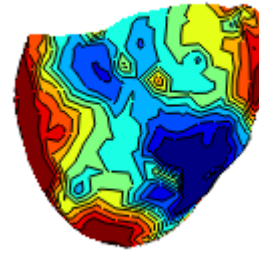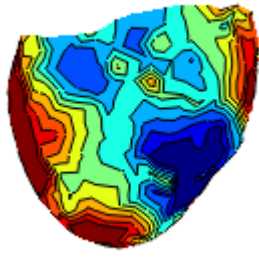(a) True   (b) Tikhonov 0 (CC = 0.73)   (c) MLIF (CC = 0.94)
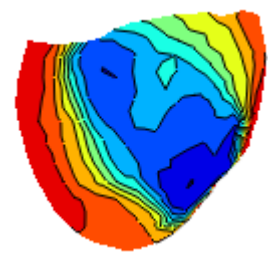
(d) RMLIF (CC = 0.94)   (e) MAPIF (CC = 0.97)   (f) RMAPIF (CC = 0.96)

(g) BMAP (CC = 0.96)   (h) Legend

Figure 4.10: Real and estimated epicardial distributions for scenario 2 under 30 dB SNR at t = 35 ms
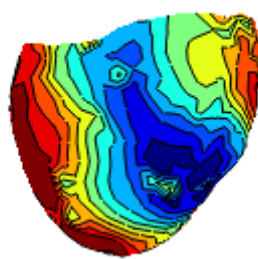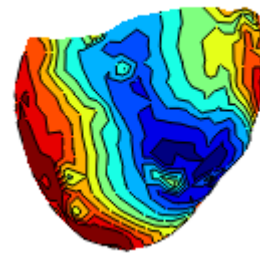
(a) True   (b) Tikhonov 0 (CC = 0.74)   (c) MLIF (CC = 0.86)
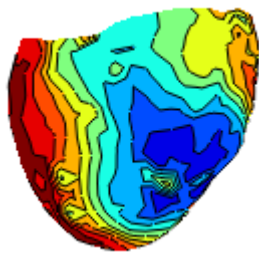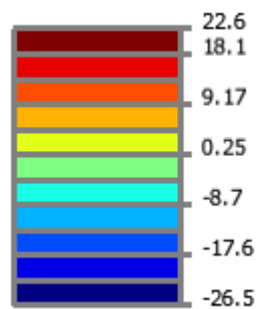
(d) RMLIF (CC = 0.87)   (e) MAPIF (CC = 0.88)   (f) RMAPIF (CC = 0.88)

(g) BMAP (CC = 0.84)   (h) Legend

Figure 4.11: Real and estimated epicardial distributions for scenario 3 under 30 dB SNR at t = 35 ms

4.4.3 Activation Time Isochrone Maps

Activation time distributions are shown in Figures 4.13 - 4.15. Table 4.3 shows correlation coefficients of activation times for different scenarios and Figure 4.12 is bar chart representation of Table 4.3. In terms of activation times, there is no significant difference between the proposed algorithms and all of the proposed algorithms are robust to the training set changes.

Method	Scenario 1	Scenario 2	Scenario 3
Tikhonov	0.98	0.98	0.99
MLIF	0.99	0.99	0.99
RMLIF	0.99	0.99	0.99
MAPIF	0.99	0.99	0.99
RMAPIF	0.99	0.99	0.99
BMAP	0.99	0.99	0.99

Table 4.3: Correlation coefficients of activation times for scenario 1, scenario 2 and scenario 3 under 30 dB SNR measurement noise
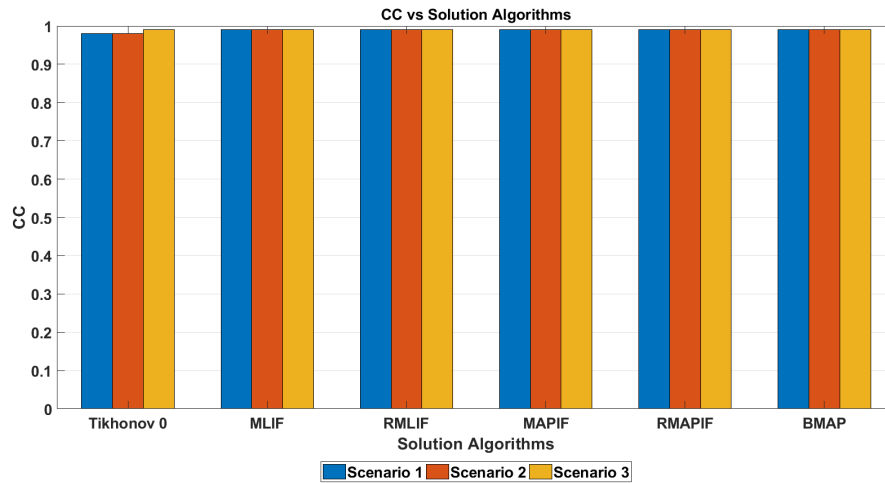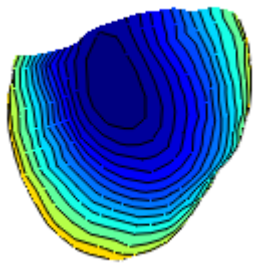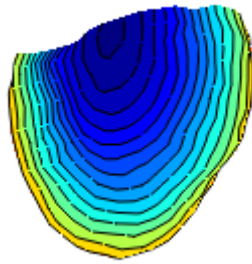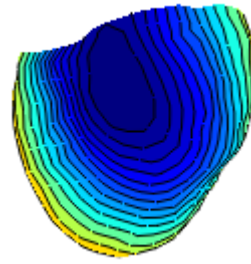

Figure 4.12: Correlation coefficients of activation times vs solution algorithms chart

(a) True   (b) Tikhonov 0 (CC=0.98)   (c) MLIF (CC=0.99)

(d) RMLIF (CC=0.99)   (e) MAPIF (CC=0.99)   (f) RMAPIF (CC=0.99)

(g) BMAP (CC=0.99)   (h) Legend

Figure 4.13: Real and estimated activation time distributions for scenario 1 under 30 dB SNR
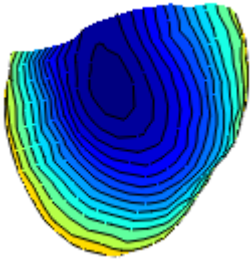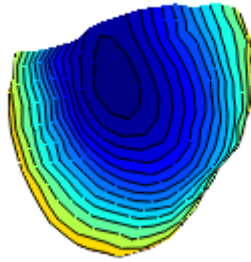
(a) True   (b) Tikhonov 0 (CC=0.98)   (c) MLIF (CC=0.99)

(d) RMLIF (CC=0.99)   (e) MAPIF (CC=0.99)   (f) RMAPIF (CC=0.99)

(g) BMAP (CC=0.99)   (h) Legend

Figure 4.14: Real and estimated activation time distributions for scenario 2 under 30 dB SNR

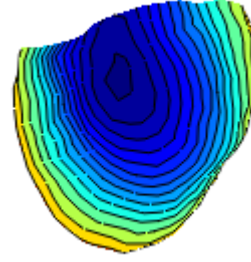(a) True   (b) Tikhonov 0 (CC=0.99)   (c) MLIF (CC=0.99)
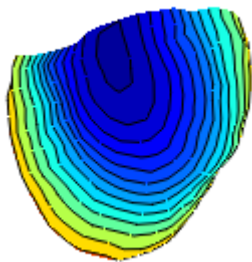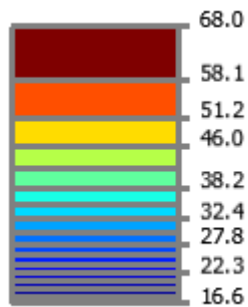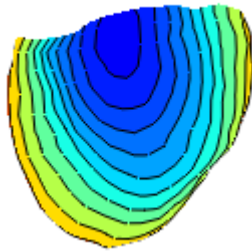
(d) RMLIF (CC=0.99)   (e) MAPIF (CC=0.99)   (f) RMAPIF (CC=0.99)
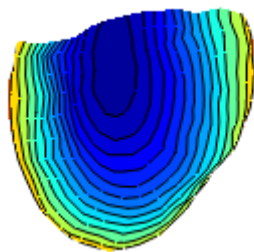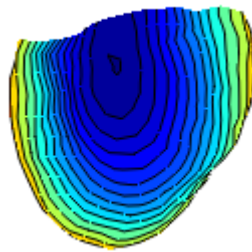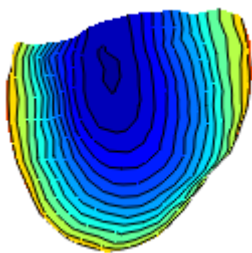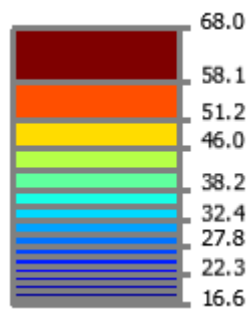
(g) BMAP (CC=0.99)   (h) Legend

Figure 4.15: Real and estimated activation time distributions for scenario 3 under 30 dB SNR
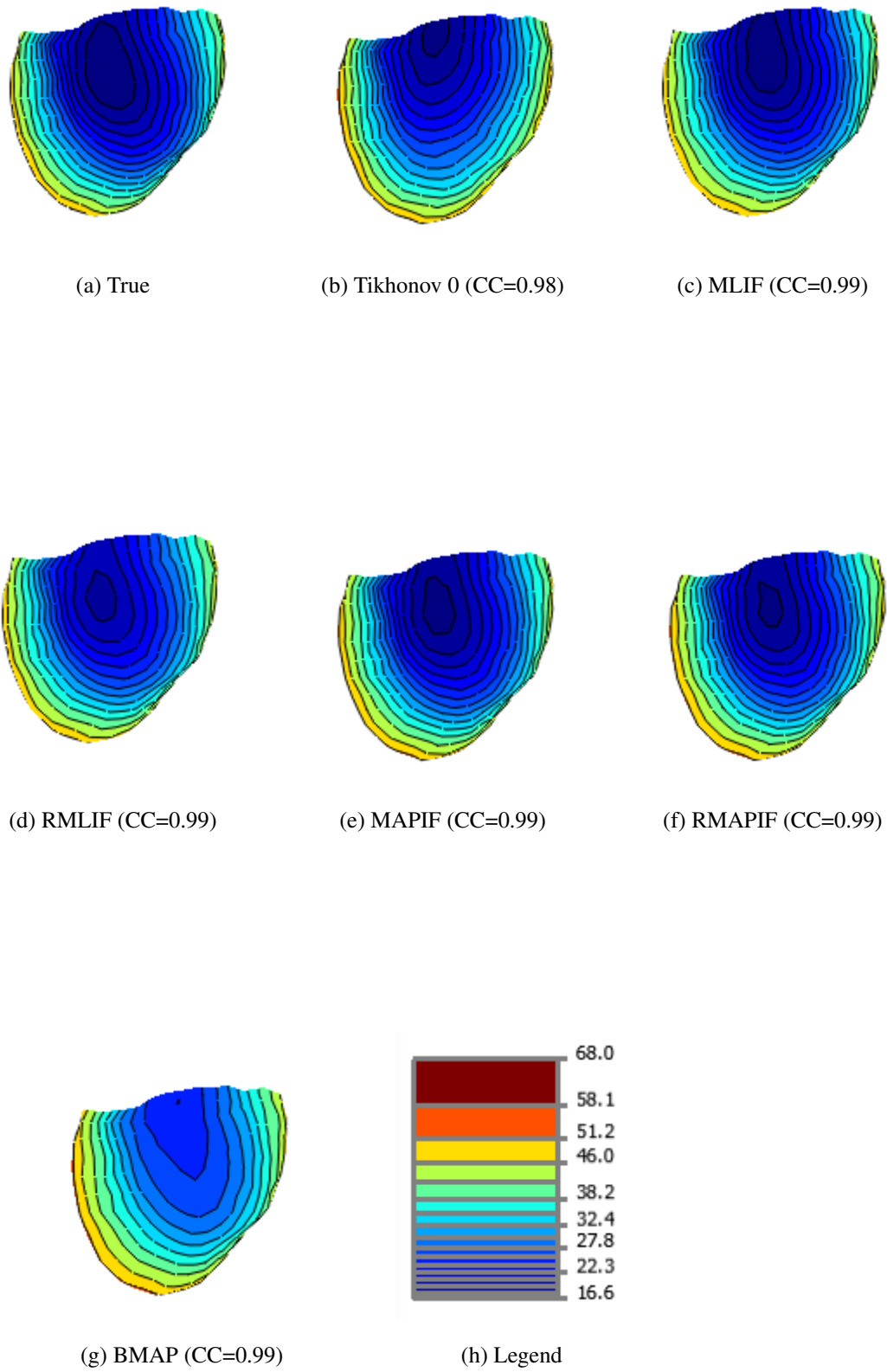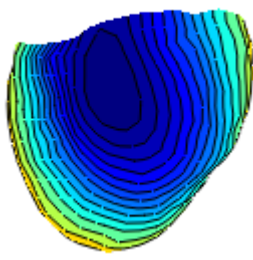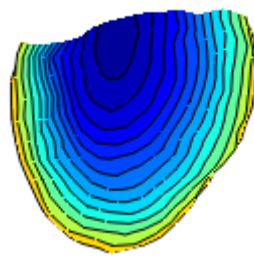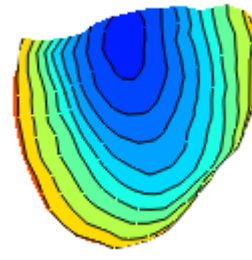
4.4.4 Localization Error Comparison

Table 4.4 shows localization errors for scenario 1, scenario 2 and scenario 3 under 30 dB SNR measurement noise, and Figure 4.16 is bar chart representation of Table 4.4.

Method	Scenario 1	Scenario 2	Scenario 3
Tikhonov	14.04	14.79	14.04
MLIF	0	4.86	14.04
RMLIF	0	0	14.04
MAPIF	0	4.86	4.86
RMAPIF	0	4.86	4.86
BMAP	4.86	14.04	4.86

Table 4.4: Localization errors (mm) for different scenarios under 30 dB SNR measurement noise

Based on Table 4.4, the following observations are made:

- In scenario 1, ML and MAP based spatio-temporal methods perform well and find the exact location of the origin of the beat.

- In scenario 2, due to exclusion of the test beat, localization errors increase.

- In scenario 3, MAP based algorithms show better performances as compared to other algorithms since ML based algorithms suffer from over-fitting.
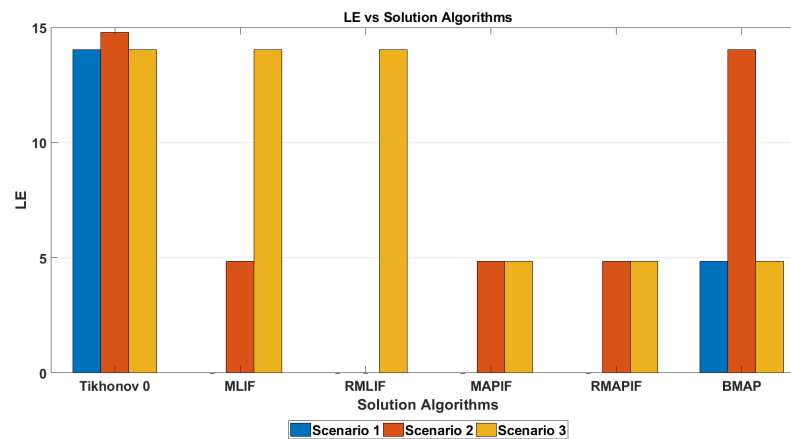
Figure 4.16: LE (mm) vs solution algorithms chart

4.4.5 Discussion of the Results

In terms of the estimated parameters, F and Q estimates are different in MAP based and ML based algorithms. When we inspect the F and Q estimates, there is a slight difference between F_{ML} and F_{MAP} estimates, which does not have significant effect on the estimated state values. The notable difference between MAP based and ML based algorithms is the difference between Q_{ML} and Q_{MAP} estimates. Q_{MAP} is much higher than Q_{ML}. Kalman gain increases with Q and when the Kalman gain is high, the estimated value of the next state mostly depends on the measurements.

### 4.4.5.1 Discussion of Scenario 1 Results

Scenario 1's training set includes the test beat. In addition to this, the training set experiments and the test beat come from the same physiological model. In light of these two settings, we expect high state estimate confidence in scenario 1. Therefore, in order to get accurate results, the Kalman gain should be small, meaning that the state estimate should mostly depend on the current state, not the measurements. Since MAPIF algorithm provides high Kalman gain, this causes poor performance as compared to MLIF algorithm. So, we can conclude that MAPIF algorithm adds unnecessary regularization to Q matrix and this is the main reason why MLIF algorithm outperforms MAPIF algorithm in scenario 1.

To understand the performances of the regularized forms of MLIF and MAPIF algorithms, we inspect the modified Kalman gains in these algorithms. The modified Kalman gain in RMLIF algorithm is lower than the Kalman gain in MLIF algorithm, on the other hand, there is a slight difference between RMAPIF and MAPIF algorithms' Kalman gains. Since the emphasis on the measurements should be less to get accurate results, i.e., small Kalman gain, clearly RMLIF is expected to be perform better than MLIF which conforms with our results. In order to understand why RMAPIF algorithm yields poor results as compared to MAPIF algorithm, consider the modified measurement update equation:

$$\hat{x}_{k|k} = \hat{x}_{k|k-1} + \tilde{K}_k H^\dagger y_k - \tilde{K}_k \hat{x}_{k|k-1} \qquad (4.3)$$

Since the decrease introduced by RMAPIF algorithm in the modified Kalman gain

cannot compensate the term $H^\dagger y_k$, RMAPIF algorithm puts more emphasis on the measurements and this yields lower performance as compared to MAPIF algorithm.

Above-mentioned algorithms take into account both temporal and spatial correlations. However, BMAP and Tikhonov 0 algorithms assume no temporal correlation between the epicardial potentials and take into account only spatial correlations. This assumption is not true since there are also temporal correlations between the epicardial potentials [137]. Hence, BMAP and Tikhonov 0 algorithms show poor performances as compared to other algorithms.

Localization error results are similar to CC and RDMS results. The methods which take into consideration both temporal and spatial correlations show better performances in terms of localization error, as expected.

4.4.5.2 Discussion of Scenario 2 Results

The correlation coefficient between the initial state estimate and the real initial state in scenario 2 is 0.4083. In scenario 1, this coefficient was 0.6429. Comparison of these two correlation coefficients shows us that we have less confidence in the state estimates in scenario 2 as compared to scenario 1. Therefore, we anticipate that a slightly higher Kalman gain will yield better results since our state estimate confidence is low. MAPIF algorithm provides slightly higher Kalman gain as compared to MLIF algorithm due to higher state covariance P and this clearly improves the correlation coefficient between the estimated and the real epicardial potentials. Hence, we can conclude that adding some regularization to the state covariance has boosted the performance.

We have asserted that higher Kalman gains yield better results but using too high Kalman gain will not result in accurate results since very high gains put unnecessary emphasis on the measurements. To evaluate the performance difference between MAPIF and RMAPIF algorithms, again, we consider the modified measurement update equation. The term $\tilde{K}_k H^\dagger$ in equation (4.3) adjusts the contribution of the measurement. We observe a small Kalman gain difference between MAPIF and RMAPIF algorithms. Since $H^\dagger$ term is already a high valued term, RMAPIF al-

gorithm puts much higher unnecessary emphasis on the measurements than MAPIF algorithm. Therefore, MAPIF outperforms RMAPIF algorithm. We also want to compare MLIF and RMLIF algorithms' performances. By following the same logic, we inspect MLIF algorithm's Kalman gain and RMILF algorithm's modified Kalman gain. RMLIF's modified Kalman gain is much smaller than MLIF's Kalman gain, approximately in the order of 10^{-2}. This modified gain compensates high valued term $H^{\dagger}$, hence RMLIF algorithm provides minor improvement to the results as compared to MLIF algorithm.

As we mentioned before, since BMAP and Tikhonov 0 algorithms assume no temporal correlation between the epicardial potentials, these two algorithms show poor performances compared to the other algorithms.

4.4.5.3 Discussion of Scenario 3 Results

In scenario 3, the training set experiments and the test beat comes from different physiological models. Due to this fact, the correlation coefficient between the initial estimated state and the real initial state is very low. This means that we have very low confidence in the state estimates, hence we predict that the emphasis on the measurements should be high to get accurate results. Maximum likelihood based estimation methods usually over-fit the training set data and this causes degraded test-set performance [127,138]. Ozbek and Demirekler's statement [127] conforms with our results and MLIF's performance is degraded in scenario 3. RMLIF algorithm performs better than MLIF algorithm due to its larger Kalman gain, as expected. MAPIF algorithm has the second best performance due its higher Kalman gain as compared to MLIF algorithm's Kalman gain.

In general, the algorithms show poor performances at the final time intervals. The reason for this can be lower RMS signal at these intervals due to small amplitudes of the epicardial signals.

4.5 Effects of The Measurement Noise

In this section, we evaluate the robustness of our proposed algorithms under different measurement noise levels. In the simulations, there is no geometric error and three different measurement noise levels are used: 10 dB, 15 dB and 30 dB SNR. The proposed algorithms' performances are compared in terms of CC, RDMS, activation times and localization errors.

4.5.1 Quantitative Evaluation of Electrograms

Mean and standard deviation of CC values, and mean and standard deviation of RDMS values are shown in Table 4.5 and Table 4.6, respectively. Figures 4.17a - 4.18c are bar chart representations of Tables 4.5 and 4.6. Detailed CC and RDMS plots are given in Appendix D for convenience.

		Tikhonov 0	MLIF	RMLIF	MAPIF	RMAPIF	BMAP
Scenario 1	10 dB	0.37±0.31	0.98±0.02	0.92±0.08	0.92±0.06	0.89±0.10	0.78±0.27
	15 dB	0.46±0.32	0.99±0.02	0.95±0.04	0.93±0.05	0.90±0.10	0.81±0.22
	30 dB	0.60±0.28	0.99±0.02	0.99±0.02	0.97±0.03	0.91±0.09	0.82±0.18
Scenario 2	10 dB	0.37±0.31	0.88±0.11	0.88±0.11	0.87±0.14	0.87±0.14	0.77±0.26
	15 dB	0.46±0.32	0.88±0.11	0.88±0.11	0.89±0.12	0.88±0.13	0.80±0.22
	30 dB	0.60±0.28	0.88±0.10	0.88±0.11	0.91±0.12	0.89±0.12	0.79±0.19
Scenario 3	10 dB	0.37±0.31	0.53±0.30	0.55±0.28	0.60±0.28	0.63±0.24	0.53±0.29
	15 dB	0.45±0.32	0.56±0.29	0.59±0.27	0.63±0.27	0.66±0.23	0.58±0.26
	30 dB	0.60±0.28	0.66±0.23	0.68±0.21	0.72±0.19	0.72±0.20	0.64±0.26

Table 4.5: Mean and standard deviation of CC values under 10 dB, 15 dB and 30 dB SNR measurement noises

		Tikhonov 0	MLIF	RMLIF	MAPIF	RMAPIF	BMAP
Scenario 1	10 dB	0.71±0.18	0.10±0.06	0.27±0.05	0.28±0.08	0.29±0.07	0.37±0.12
	15 dB	0.66±0.17	0.10±0.05	0.20±0.05	0.25±0.07	0.27±0.07	0.35±0.12
	30 dB	0.55±0.11	0.11±0.05	0.09±0.04	0.17±0.06	0.26±0.05	0.35±0.10
Scenario 2	10 dB	0.71±0.18	0.31±0.06	0.30±0.06	0.30±0.08	0.30±0.08	0.38±0.12
	15 dB	0.66±0.17	0.31±0.06	0.30±0.06	0.29±0.07	0.29±0.07	0.36±0.12
	30 dB	0.55±0.11	0.31±0.06	0.30±0.06	0.24±0.07	0.28±0.07	0.38±0.11
Scenario 3	10 dB	0.71±0.18	0.68±0.22	0.67±0.18	0.56±0.10	0.57±0.09	0.61±0.13
	15 dB	0.66±0.17	0.66±0.22	0.64±0.20	0.54±0.09	0.54±0.08	0.57±0.11
	30 dB	0.55±0.11	0.58±0.19	0.56±0.15	0.49±0.07	0.49±0.17	0.53±0.09

Table 4.6: Mean and standard deviation of RDMS values under 10 dB, 15 dB and 30 dB SNR measurement noises

Based on Table 4.5 and Table 4.6, the following observations are made when the measurement noise is increased from 30 dB to 10 dB SNR:

- Tikhonov 0's mean correlation coefficient decreases by approximately 38%,

- BMAP's mean correlation coefficient decreases by approximately 4%, 2% and 17%,

- MLIF's mean correlation coefficient decreases by approximately 1%, 0% and 19%,

- RMLIF's mean correlation coefficient decreases by approximately 7%, 0% and 19%,

- MAPIF's mean correlation coefficient decreases by approximately 5%, 4% and 16%,

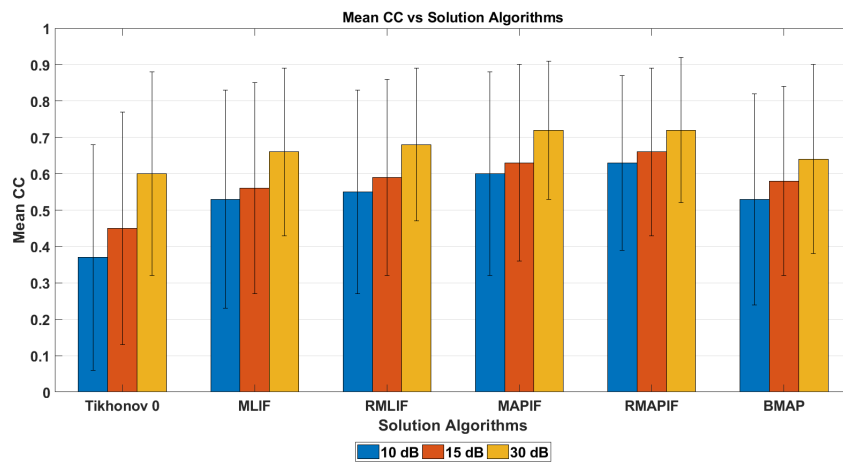- RMAPIF's mean correlation coefficient decreases by approximately 2%, 2% and 12%,

in scenario 1, scenario 2 and scenario 3, respectively.
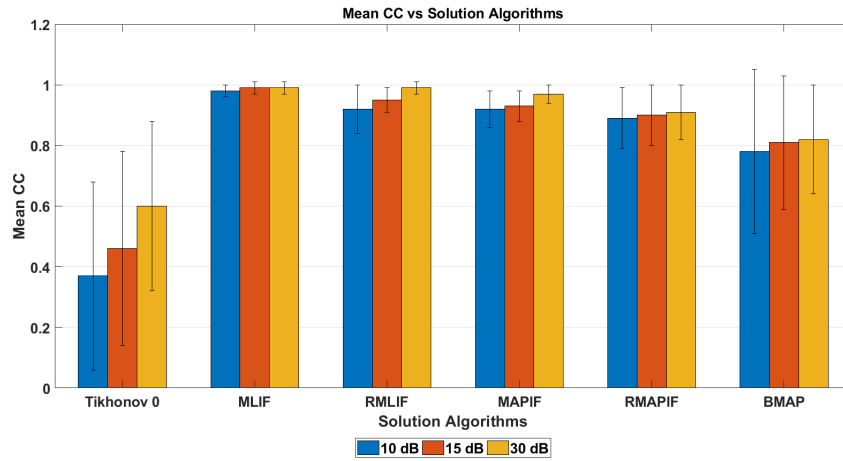
(a) Mean CC vs solution algorithms chart for scenario 1
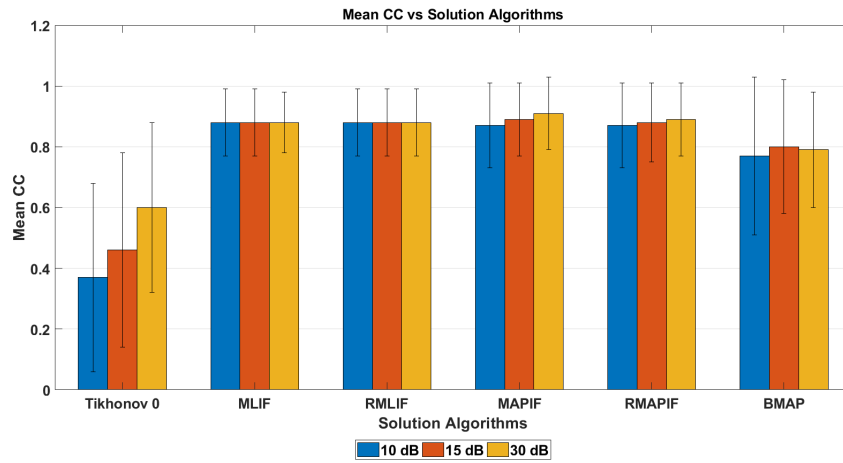
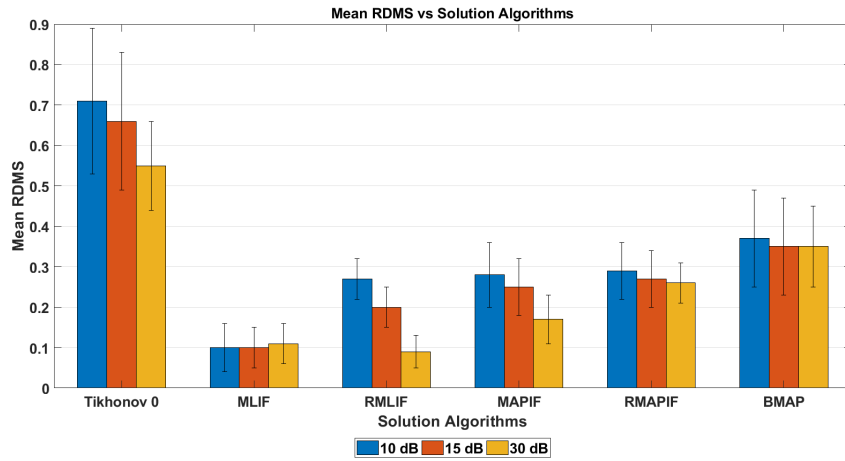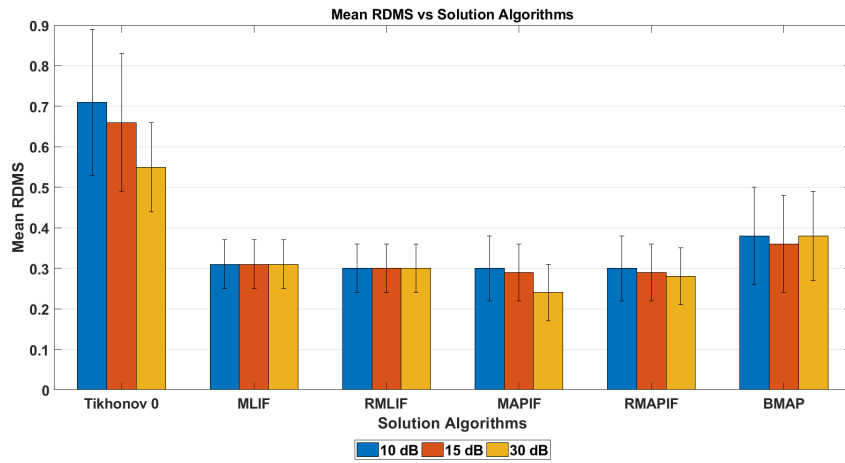(b) Mean CC vs solution algorithms chart for scenario 2

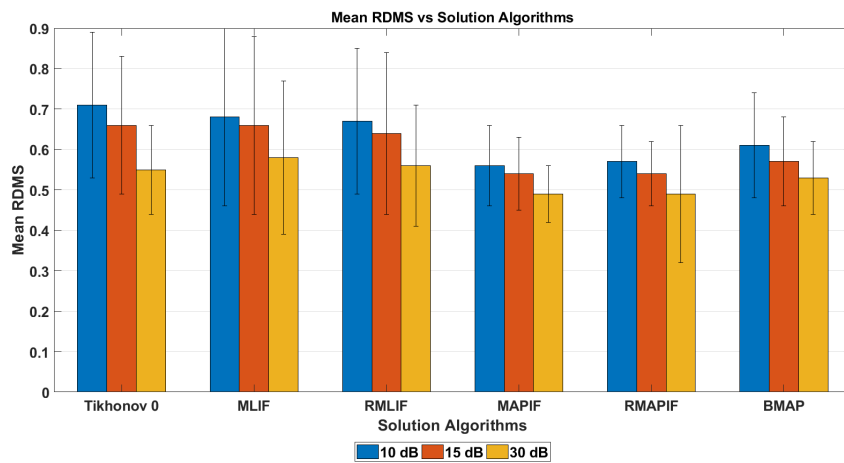(c) Mean CC vs solution algorithms chart for scenario 3

Figure 4.17: Mean CC vs solution algorithms charts

(a) Mean RDMS vs solution algorithms chart for scenario 1

(b) Mean RDMS vs solution algorithms chart for scenario 2

(c) Mean RDMS vs solution algorithms chart for scenario 3

Figure 4.18: Mean RDMS vs solution algorithms charts

4.5.2 Isopotential Epicardial Maps

True and reconstructed epicardial distributions on the heart surface, viewed from posterior region, under different measurement noises for scenario 1, scenario 2 and scenario 3 are shown in Figures 4.19 - 4.24. We have already given the isopotential epicardial maps for 30 dB SNR case in section 4.4.2, hence we do not repeat these results in here.

Based on Figures 4.19 - 4.24, the following observations are made:

- Tikhonov 0 is the most affected method, its CC value drops by approximately %50, when the measurement noise is increased from 30 dB SNR to 10 dB SNR. Tikhonov 0's smoothing effect can be seen in isopotential epicardial maps.

- In scenario 1 and scenario 2, the training set data and the test beat come from the same physiological model. Hence, the reconstructed epicardial distributions are more similar to true epicardial distribution. In scenario 3, since the training set data and the test data come from different physiological models, the results are not as good as other scenarios.

- As seen in Figures 4.23 and 4.24, the reconstruction accuracies of MAPIF and RMAPIF are higher than the other algorithms in scenario 3. This result is expected since MAP based approaches do not suffer from the over-fitting.

- As can be seen in isopotential maps, spatio-temporal approaches, MLIF, RM-LIF, MAPIF and RMAPIF, enhance the reconstruction accuracy and more robust to the measurement noise.
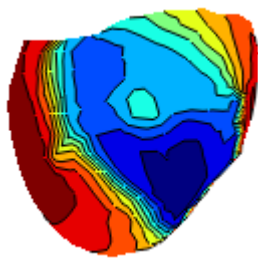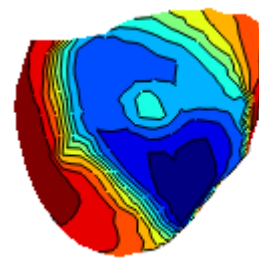
(a) True   (b) Tikhonov 0 (CC = 0.38)   (c) MLIF (CC = 0.99)

(d) RMLIF (CC = 0.96)   (e) MAPIF (CC = 0.96)   (f) RMAPIF (CC = 0.96)

(g) BMAP (CC = 0.95)   (h) Legend

Figure 4.19: Real and estimated epicardial distributions for scenario 1 under 10 dB SNR at t = 35 ms

(a) True

(b) Tikhonov 0 (CC = 0.52)

(c) MLIF (CC = 0.99)

(d) RMLIF (CC = 0.98)

(e) MAPIF (CC = 0.97)

(f) RMAPIF (CC = 0.97)

(g) BMAP (CC = 0.97)

(h) Legend

Figure 4.20: Real and estimated epicardial distributions for scenario 1 under 15 dB SNR at t = 35 ms

(a) True   (b) Tikhonov 0 (CC = 0.38)   (c) MLIF (CC = 0.94)

(d) RMLIF (CC = 0.94)   (e) MAPIF (CC = 0.96)   (f) RMAPIF (CC = 0.96)

(g) BMAP (CC = 0.94)   (h) Legend

Figure 4.21: Real and estimated epicardial distributions for scenario 2 under 10 dB SNR at t = 35 ms
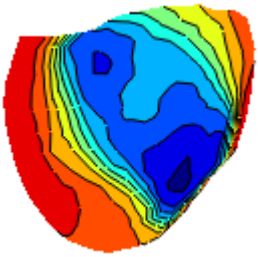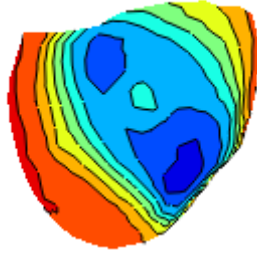
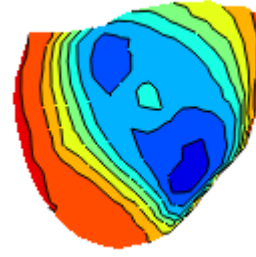(a) True   (b) Tikhonov 0 (CC = 0.51)   (c) MLIF (CC = 0.94)
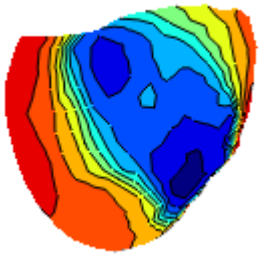
(d) RMLIF (CC = 0.94)   (e) MAPIF (CC = 0.96)   (f) RMAPIF (CC = 0.96)
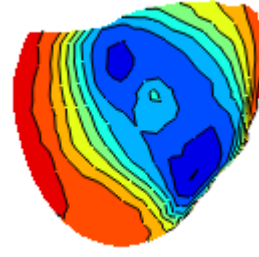
(g) BMAP (CC = 0.97)   (h) Legend

Figure 4.22: Real and estimated epicardial distributions for scenario 2 under 15 dB SNR at t = 35 ms
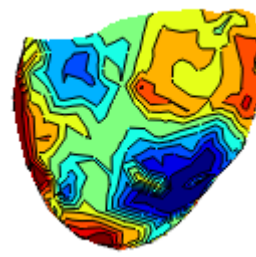
(a) True   (b) Tikhonov 0 (CC = 0.38)   (c) MLIF (CC = 0.77)
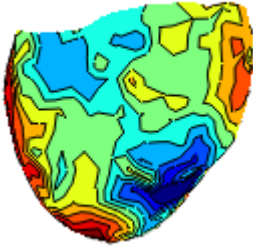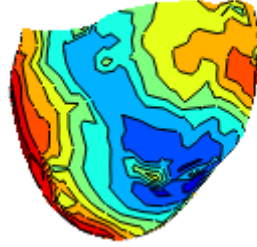
(d) RMLIF (CC = 0.77)   (e) MAPIF (CC = 0.83)   (f) RMAPIF (CC = 0.83)
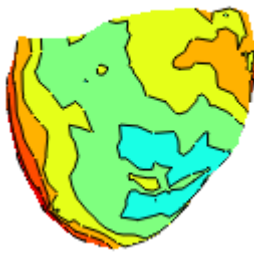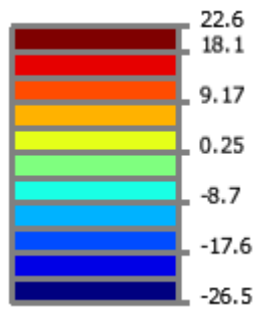
(g) BMAP (CC = 0.73)   (h) Legend

Figure 4.23: Real and estimated epicardial distributions for scenario 3 under 10 dB SNR at t = 35 ms
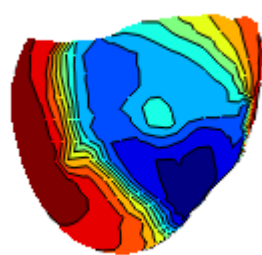
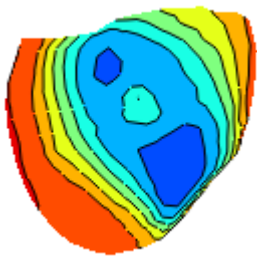(a) True

(b) Tikhonov 0 (CC = 0.52)
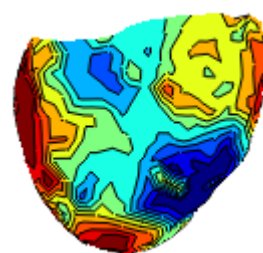
(c) MLIF (CC = 0.80)
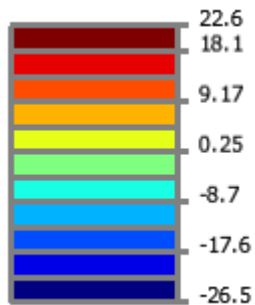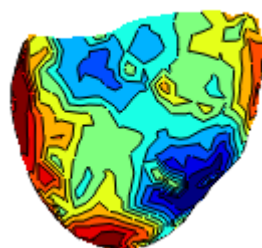
(d) RMLIF (CC = 0.81)
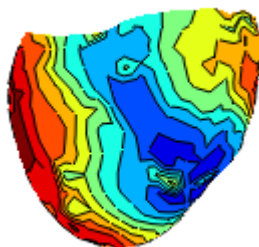
(e) MAPIF (CC = 0.85)
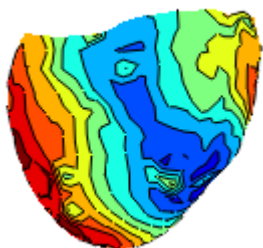
(f) RMAPIF (CC = 0.86)
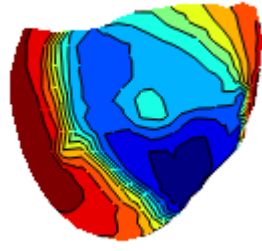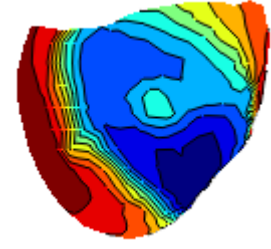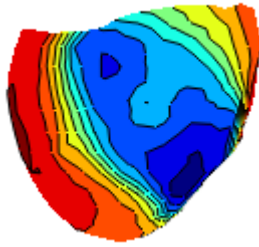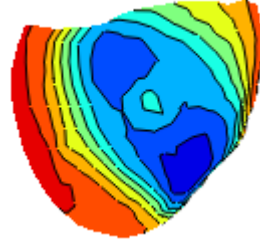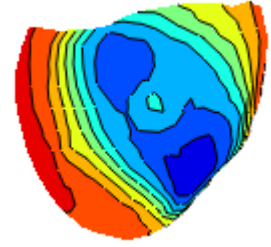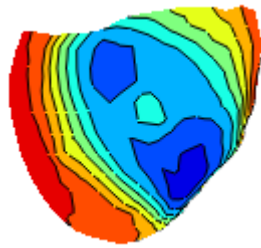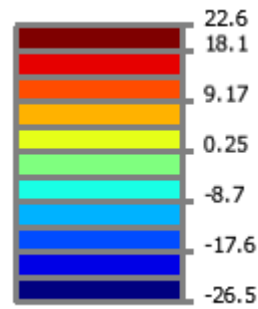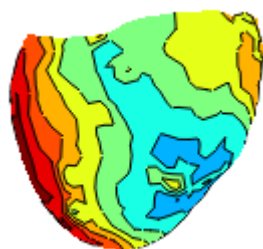
(g) BMAP (CC = 0.78)
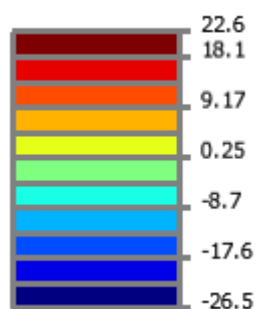
(h) Legend

Figure 4.24: Real and estimated epicardial distributions for scenario 3 under 15 dB SNR at t = 35 ms

4.5.3 Activation Time Isochrone Maps

Activation time distributions are shown in Figures 4.26 - 4.31. Table 4.7 shows correlation coefficients of activation times for different measurement noise levels and Figure 4.25 is bar chart representation of Table 4.7. In terms of activation times, there is no significant difference between the proposed algorithms and all of the proposed algorithms are robust to the measurement noise changes.

		Tikhonov 0	MLIF	RMLIF	MAPIF	RMAPIF	BMAP
Scenario 1	**10 dB**	0.96	0.99	0.99	0.99	0.99	0.99
	15 dB	0.95	0.99	0.99	0.99	0.99	0.99
	30 dB	0.98	0.99	0.99	0.99	0.99	0.99
Scenario 2	**10 dB**	0.96	0.99	0.99	0.99	0.99	0.99
	15 dB	0.95	0.99	0.99	0.99	0.99	0.99
	30 dB	0.98	0.99	0.99	0.99	0.99	0.99
Scenario 3	**10 dB**	0.96	0.99	0.98	0.99	0.99	0.97
	15 dB	0.95	0.99	0.99	0.99	0.99	0.98
	30 dB	0.99	0.99	0.99	0.99	0.99	0.99

Table 4.7: Correlation coefficients of activation times for scenario 1, scenario 2 and scenario 3 under 10 dB, 15 dB and 30 dB SNR measurement noises
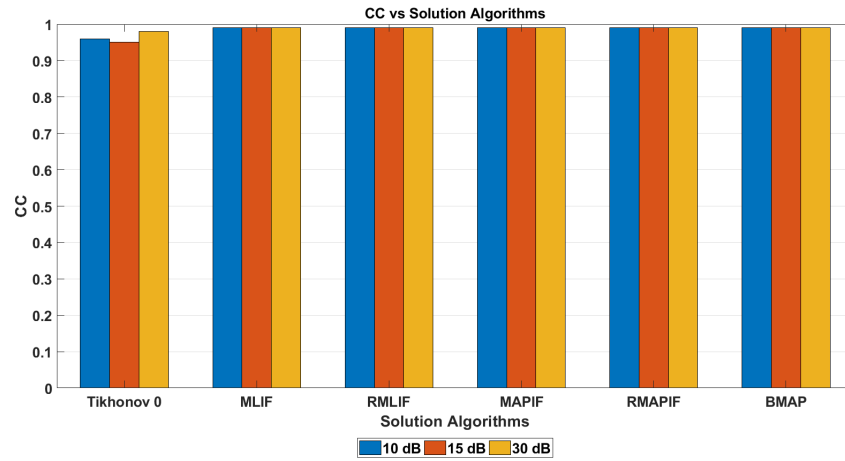
(a) Correlation coefficients of activation times vs solution algorithms chart for scenario 1
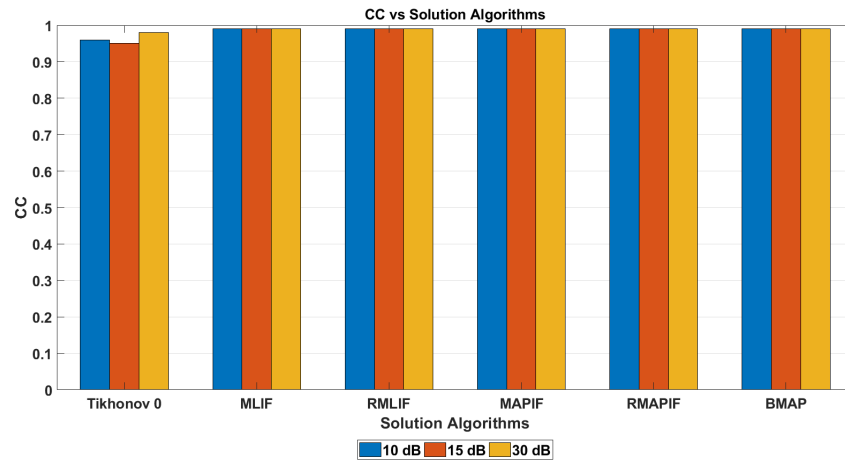
(b) Correlation coefficients of activation times vs solution algorithms chart for scenario 2
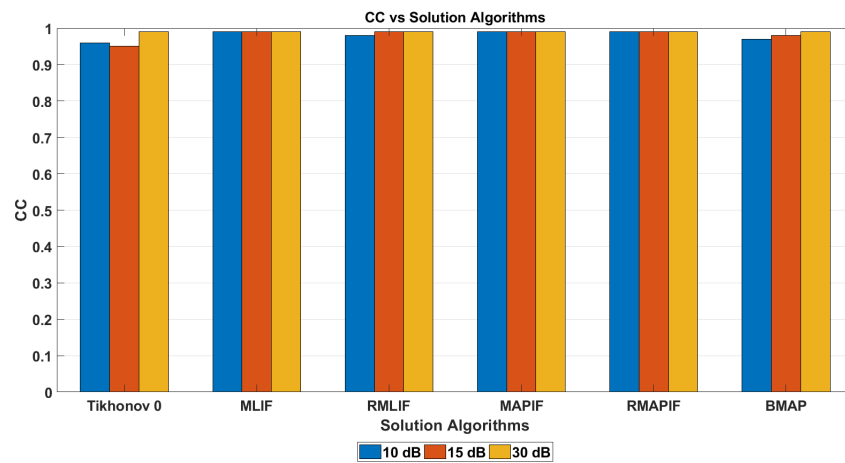
(c) Correlation coefficients of activation times vs solution algorithms chart for scenario 3

Figure 4.25: Correlation coefficients of activation times vs solution algorithms chart

(a) True　　　　　(b) Tikhonov 0 (CC=0.96)　　　　　(c) MLIF (CC=0.99)
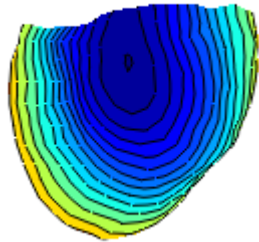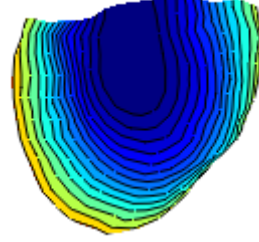
(d) RMLIF (CC=0.99)　　　　　(e) MAPIF (CC=0.99)　　　　　(f) RMAPIF (CC=0.99)
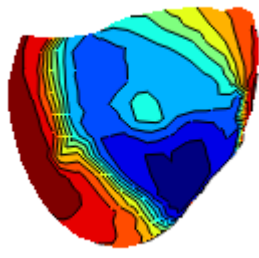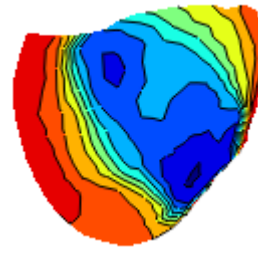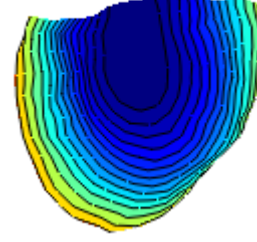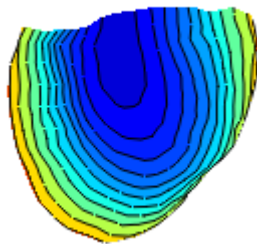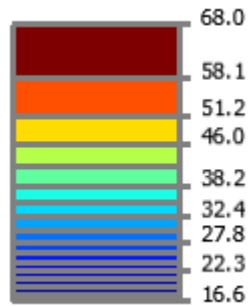
(g) BMAP (CC=0.99)　　　　　(h) Legend

Figure 4.26: Real and estimated activation time distributions for scenario 1 under 10 dB SNR
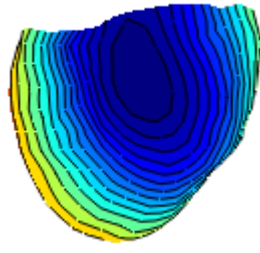
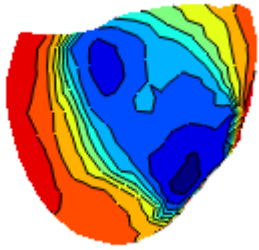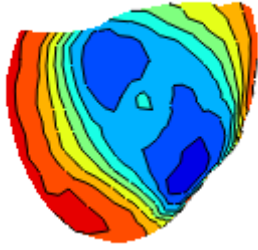(a) True   (b) Tikhonov 0 (CC=0.95)   (c) MLIF (CC=0.99)
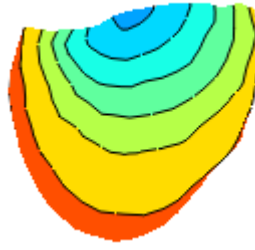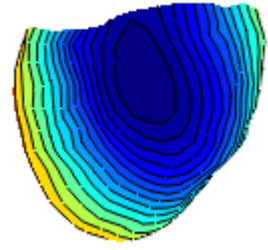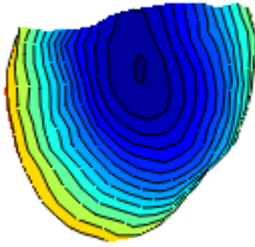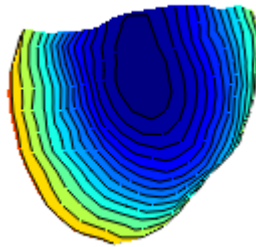
(d) RMLIF (CC=0.99)   (e) MAPIF (CC=0.99)   (f) RMAPIF (CC=0.99)
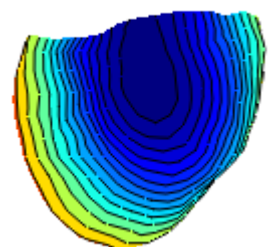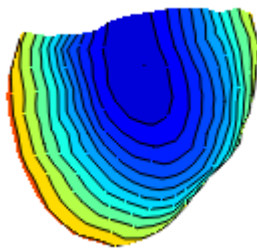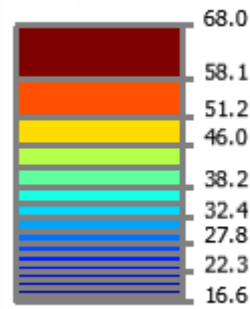
(g) BMAP (CC=0.99)   (h) Legend

Figure 4.27: Real and estimated activation time distributions for scenario 1 under 15 dB SNR
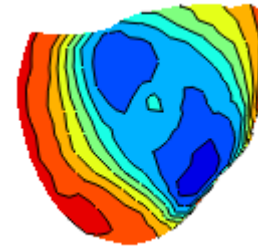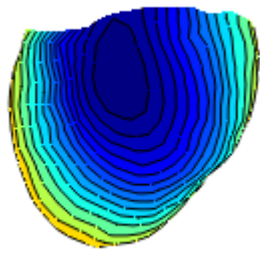
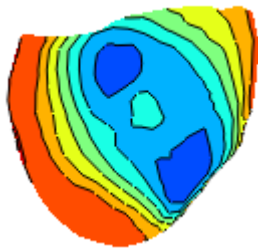(a) True   (b) Tikhonov 0 (CC=0.96)   (c) MLIF (CC=0.99)
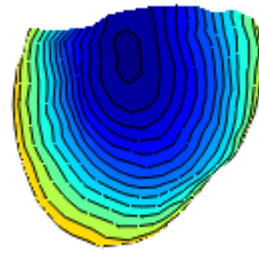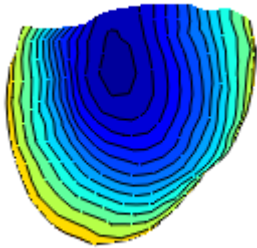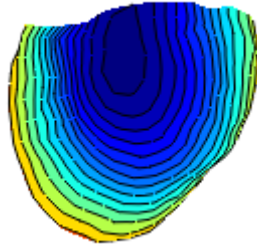
(d) RMLIF (CC=0.99)   (e) MAPIF (CC=0.99)   (f) RMAPIF (CC=0.99)
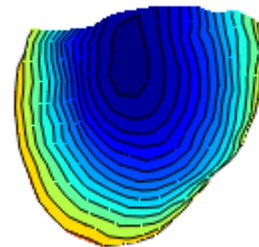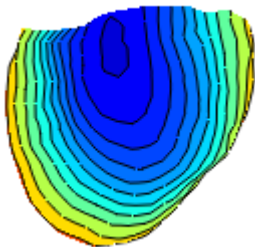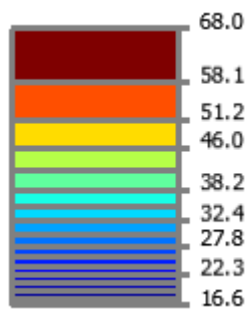
(g) BMAP (CC=0.99)   (h) Legend

Figure 4.28: Real and estimated activation time distributions for scenario 2 under 10 dB SNR
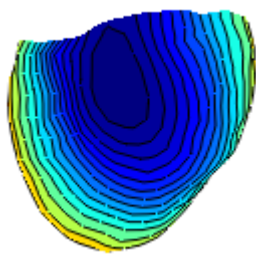
(a) True   (b) Tikhonov 0 (CC=0.95)   (c) MLIF (CC=0.99)
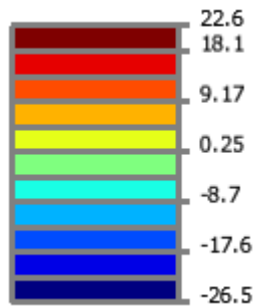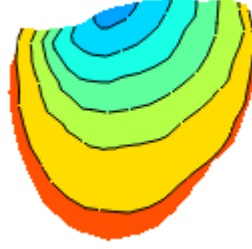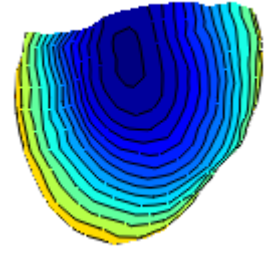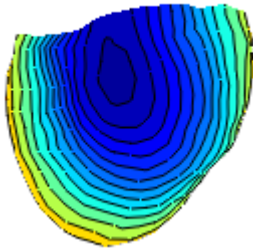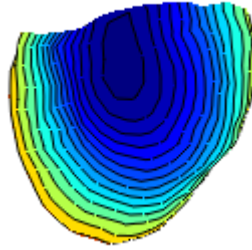
(d) RMLIF (CC=0.99)   (e) MAPIF (CC=0.99)   (f) RMAPIF (CC=0.99)
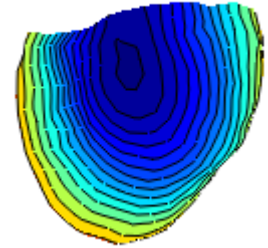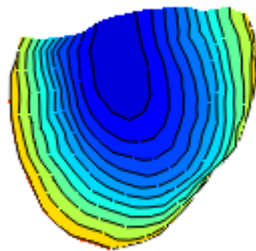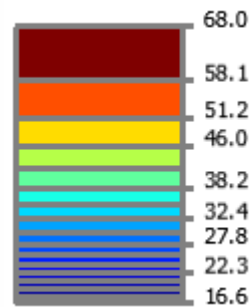
(g) BMAP (CC=0.99)   (h) Legend

Figure 4.29: Real and estimated activation time distributions for scenario 2 under 15 dB SNR
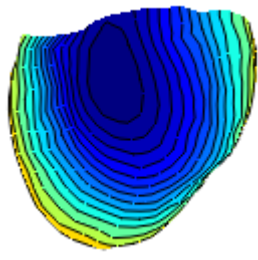
(a) True   (b) Tikhonov 0 (CC=0.96)   (c) MLIF (CC=0.99)
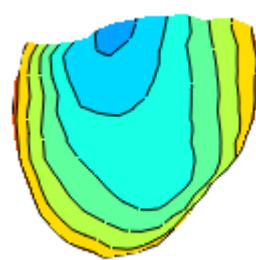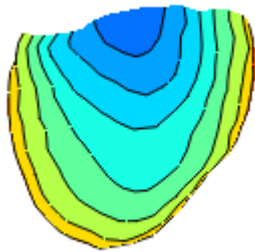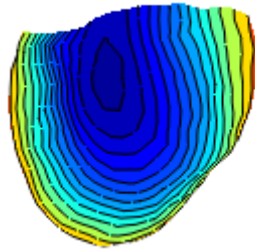
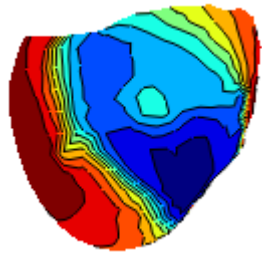(d) RMLIF (CC=0.98)   (e) MAPIF (CC=0.99)   (f) RMAPIF (CC=0.99)
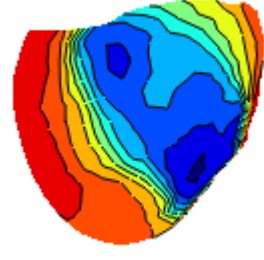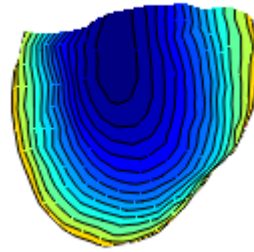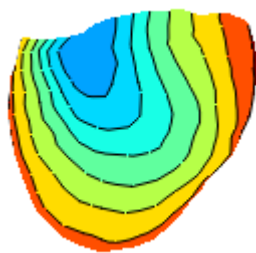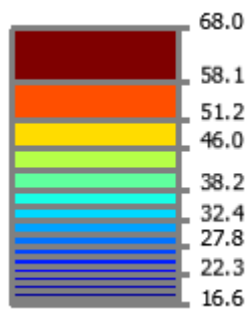
(g) BMAP (CC=0.97)   (h) Legend

Figure 4.30: Real and estimated activation time distributions for scenario 3 under 10 dB SNR
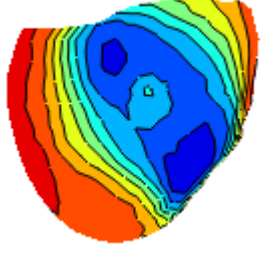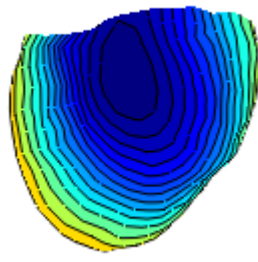
(a) True
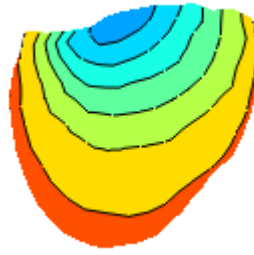
(b) Tikhonov 0 (CC=0.95)
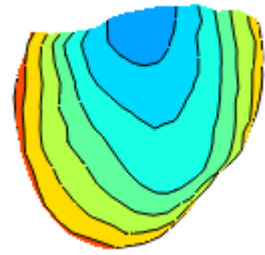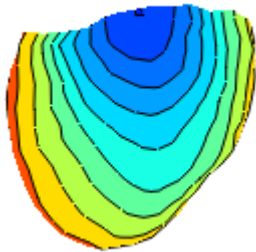
(c) MLIF (CC=0.99)

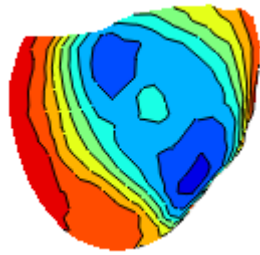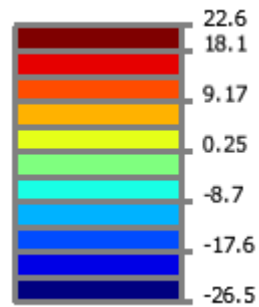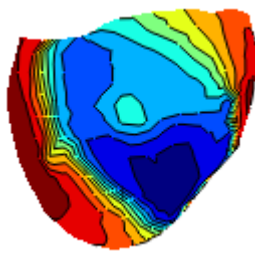(d) RMLIF (CC=0.99)
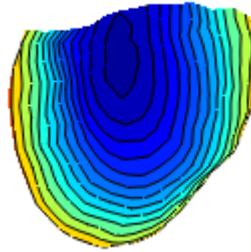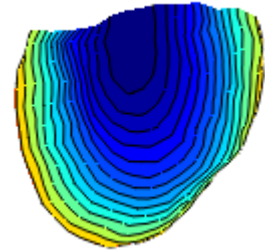
(e) MAPIF (CC=0.99)

(f) RMAPIF (CC=0.99)
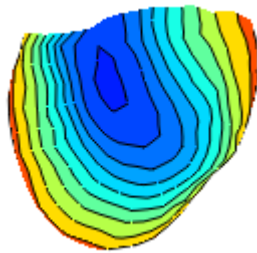
(g) BMAP (CC=0.98)
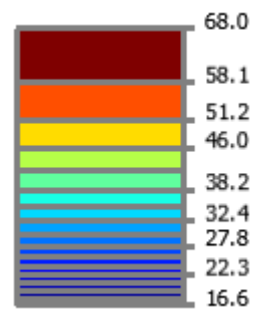
(h) Legend

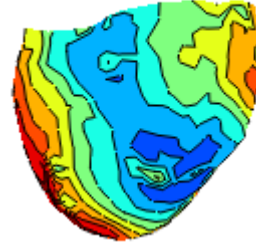Figure 4.31: Real and estimated activation time distributions for scenario 3 under 15 dB SNR

4.5.4   Localization Error Comparison

Table 4.8 shows localization errors under different measurement noise levels and Figure 4.32 is bar chart representation of Table 4.8.

		Tikhonov 0	MLIF	RMLIF	MAPIF	RMAPIF	BMAP
Scenario 1	**10 dB**	19.2	0	4.86	4.86	4.86	4.86
	15 dB	18.70	0	4.86	4.86	4.86	4.86
	30 dB	14.04	0	0	0	0	4.86
Scenario 2	**10 dB**	18.70	4.86	4.86	4.86	4.86	10.43
	15 dB	18.70	4.86	4.86	4.86	4.86	4.86
	30 dB	14.79	4.86	0	4.86	4.86	14.04
Scenario 3	**10 dB**	19.12	14.79	18.34	4.93	4.86	12.73
	15 dB	18.70	18.34	18.34	10.43	10.43	4.93
	30 dB	14.04	14.04	14.04	4.86	4.86	4.86

Table 4.8: Localization errors (mm) under 10 dB, 15 dB and 30 dB SNR measurement noises

Based on Table 4.8, the following observations are made:

- ML based and MAP based algorithms show similar performances in scenario 1 and scenario 2.

- In scenario 3, MAP based algorithms outperform the other algorithms.

- Tikhonov 0 is the most sensitive algorithm to the measurement noise among the proposed algorithms. Also, it has the worst performance in terms of localization error.

- In general, ML based algorithms MLIF and RMLIF are more robust to measurement noise changes.

- Some inconsistencies are observed in some cases, e.g., in scenario 2, BMAP algorithm's localization error in 30 dB SNR case is higher than in 15 dB SNR case. If the reconstructed wave-fronts are very sparse at the initial time frames, this situation may cause wrong localization error results, as in BMAP algorithm's case.
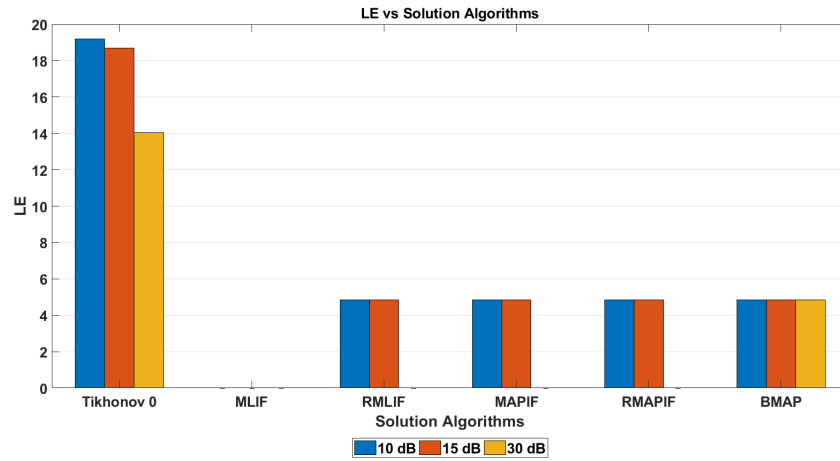
(a) LE (mm) vs solution algorithms chart for scenario 1
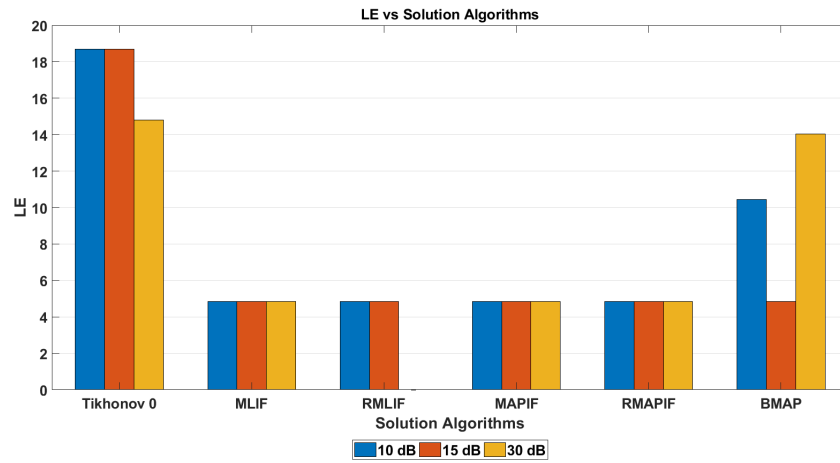
(b) LE (mm) vs solution algorithms chart for scenario 2
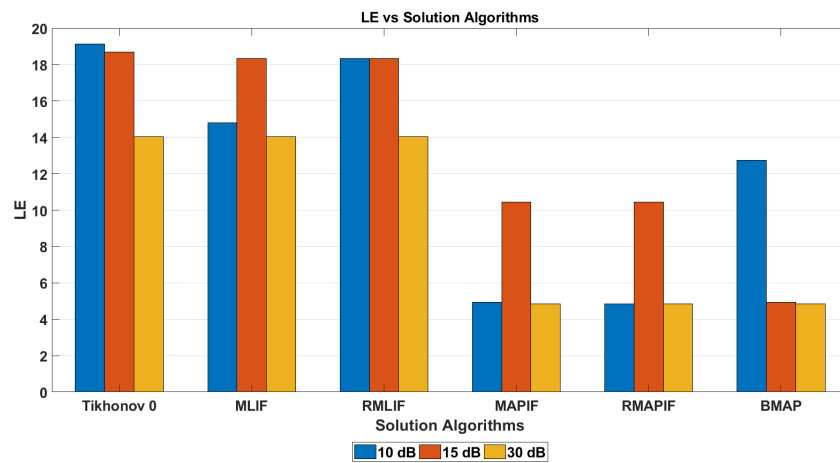
(c) LE (mm) vs solution algorithms chart for scenario 3

Figure 4.32: LE (mm) vs solution algorithms chart

4.5.5 Discussion of the Results

In this section, we investigate the sensitivity of the proposed algorithms to different measurement noise levels. In this thesis, three different measurement noise levels are used: 10 dB, 15 dB and 30 dB SNR.

Suppose the Kalman filter is designed with $Q \geq 0$ and $R > 0$ but the actual noise covariances are Q^0 and R^0. In this case, the Kalman filter's minimum variance estimate property is violated [139]. Hence, instead of Kalman filter's classical equations, we use Kalman filter's general equations as follows [140, 141]:

$$P_{k|k} = (I - K_k H) P_{k|k-1} (I - K_k H)^T + K_k R K_k^T \tag{4.4}$$

$$P_{k|k-1} = F P_{k-1|k-1} F^T + Q \tag{4.5}$$

Substituting equation (4.5) into equation (4.4), we find the state covariance formula as:

$$P_{k|k} = (I - K_k H) F P_{k-1|k-1} F^T (I - K_k H)^T + (I - K_k H) Q (I - K_k H)^T + K_k R K_k^T \tag{4.6}$$

The performance of the filter is evaluated by calculating $tr(P_{k|k})$ [142]. In this case, we want to see the effect of R, hence we write $P_{k|k}$ as a function of R and drop k subscript for the convenience:

$$P(R) \triangleq P(r_{11}, r_{12}, r_{13}, ..., r_{MM}) \tag{4.7}$$

If there is a perturbation in R, we write $P(R)$ as $P(R + \Delta)$. Using the matrix form of Taylor expansion which is given by Turnbull [143], we get:

$$tr(P(R + \Delta)) = tr(P(R)) + \frac{\partial}{\partial R} tr(P(R))\Delta + \frac{\partial^2}{\partial R^2} tr(P(R))\frac{\Delta^2}{2} + \mathbf{H.O.T} \tag{4.8}$$

Under the assumption of small deviations from R, we neglect the second and higher order terms. Carrying out the derivation in the above equation, we obtain:

$$\frac{\partial}{\partial R} tr(P(R)) = \frac{\partial}{\partial R} tr((I - K_k H) F P_{k-1|k-1} F^T (I - K_k H)^T$$
$$+ (I - K_k H) Q (I - K_k H)^T + K_k R K_k^T) \tag{4.9}$$

$$= K_k^T K_k \tag{4.10}$$

Note that we did not carry out derivation for the first and second terms in equation (4.6) since they are not explicit functions of R. In this section, we are investigating the effects of changing R and assumed that the Kalman gain is already computed. Hence, we do not carry out any derivations due the Kalman gain's dependency on R, since we do not want to do any corrections on the filter [142].

In light of the discussion above, we can conclude that the value of $K_k^T K_k$ determines the Kalman filter sensitivity to parameter R and higher Kalman gains cause more deviations in the state estimates.

In ML based algorithms, the Kalman gains are lower than the gains in MAP based algorithms. Hence, the sensitivity to the measurement noise is lower and the robustness to the measurement noise is higher in MLIF and RMLIF algorithms. Due to their higher Kalman gains as compared to the gains in ML based algorithms, MAP based algorithms MAPIF and RMAPIF have higher sensitivity and lower robustness to the measurement noise.

Overall, we observe that Tikhonov 0 and BMAP algorithms have the highest sensitivity to the measurement noise. The reason behind that is these two methods are spatial methods and they ignore the temporal correlations. BMAP is more robust as compared to Tikhonov 0 since BMAP uses statistical prior information on epicardial potential distribution. ML and MAP based algorithms are more robust than Tikhonov 0 and BMAP algorithms since they are spatio-temporal methods.

4.6 Effects of Geometric Errors

The forward model in inverse electrocardiography is usually obtained by first segmenting medical images to obtain organ boundaries, then using numerical solution techniques such as BEM, FEM, or a combination of both to solve the forward ECG problem. However, errors in the segmentation of medical images, discretization errors introduced by numerical solvers, errors introduced by ignoring the movement of the heart, and errors in the conductivity values generate geometric errors, which in turn cause estimation errors in the inverse ECG solutions. In this section, we focus on wrong determination of heart's position. This situation is usually caused by the

movement of the heart.

4.6.1 Geometric Shift Error

In this section, we investigate the effects of faulty determination of the heart's location. To do this, we solve the forward problem by using the correct forward transfer matrix. In the inverse problem solutions, the position of the heart mesh is changed and the forward transfer matrix is found by using the faulty mesh. The heart is shifted in x, y and z directions by -15 mm to +15 mm from its original position. In the simulation of the body surface potentials, 30 dB SNR measurement noise is used.

4.6.1.1 Shift Error in the x Direction

Quantitative Evaluation of Electrograms

Tables 4.9 - 4.11 show the mean and standard deviation of CC values, and Tables 4.12 - 4.14 show mean and standard deviation of RDMS values for scenario 1, scenario 2 and scenario 3, respectively, when there is a shift in x direction by -15 mm to +15 mm from original position of the heart location. Figures 4.33a - 4.34c are bar chart representations of Tables 4.9 - 4.14.

	-15 mm	-10 mm	-6 mm	No Shift	+6 mm	+10 mm	+15 mm
Tikhonov 0	0.55±0.24	0.59±0.26	0.60±0.27	0.60±0.28	0.58±0.27	0.55±0.27	0.51±0.26
MLIF	0.99±0.02	0.99±0.02	0.99±0.02	0.99±0.02	0.99±0.02	0.99±0.02	0.99±0.02
RMLIF	0.99±0.02	0.98±0.02	0.99±0.01	0.99±0.02	0.99±0.02	0.99±0.02	0.99±0.02
MAPIF	0.97±0.04	0.97±0.04	0.97±0.04	0.97±0.03	0.96±0.04	0.96±0.04	0.96±0.05
RMAPIF	0.90±0.10	0.90±0.10	0.91±0.10	0.91±0.09	0.91±0.09	0.90±0.10	0.91±0.10
BMAP	0.74±0.21	0.77±0.21	0.80±0.20	0.82±0.18	0.83±0.14	0.81±0.13	0.78±0.15

Table 4.9: Scenario 1: Mean and standard deviation of CC values for -15 mm to +15 mm shift in x direction

	-15 mm	-10 mm	-6 mm	No Shift	+6 mm	+10 mm	+15 mm
Tikhonov 0	0.55±0.24	0.59±0.26	0.60±0.27	0.60±0.28	0.58±0.27	0.55±0.27	0.51±0.26
MLIF	0.88±0.10	0.88±0.10	0.88±0.10	0.88±0.10	0.88±0.11	0.88±0.11	0.88±0.11
RMLIF	0.88±0.11	0.89±0.11	0.89±0.11	0.88±0.11	0.88±0.11	0.88±0.11	0.88±0.11
MAPIF	0.90±0.14	0.90±0.14	0.90±0.14	0.91±0.12	0.91±0.10	0.90±0.11	0.90±0.11
RMAPIF	0.88±0.14	0.87±0.14	0.88±0.13	0.89±0.12	0.89±0.12	0.88±0.13	0.89±0.12
BMAP	0.72±0.23	0.75±0.22	0.77±0.22	0.79±0.19	0.79±0.16	0.78±0.15	0.74±0.15

Table 4.10: Scenario 2: Mean and standard deviation of CC values for -15 mm to +15 mm shift in x direction

	-15 mm	-10 mm	-6 mm	No Shift	+6 mm	+10 mm	+15 mm
Tikhonov 0	0.55±0.24	0.59±0.26	0.60±0.27	0.60±0.28	0.58±0.27	0.55±0.27	0.51±0.26
MLIF	0.55±0.25	0.60±0.24	0.63±0.23	0.66±0.23	0.65±0.22	0.65±0.22	0.64±0.22
RMLIF	0.58±0.25	0.63±0.22	0.67±0.21	0.68±0.21	0.66±0.21	0.65±0.21	0.64±0.22
MAPIF	0.63±0.23	0.66±0.22	0.69±0.21	0.72±0.19	0.71±0.18	0.70±0.18	0.68±0.18
RMAPIF	0.64±0.22	0.67±0.21	0.70±0.21	0.72±0.20	0.70±0.19	0.70±0.17	0.68±0.20
BMAP	0.61±0.24	0.64±0.26	0.65±0.26	0.64±0.26	0.62±0.24	0.59±0.23	0.55±0.22

Table 4.11: Scenario 3: Mean and standard deviation of CC values for -15 mm to +15 mm shift in x direction

	-15 mm	-10 mm	-6 mm	No Shift	+6 mm	+10 mm	+15 mm
Tikhonov 0	0.62±0.12	0.57±0.11	0.55±0.11	0.55±0.11	0.58±0.11	0.60±0.11	0.64±0.12
MLIF	0.10±0.05	0.10±0.05	0.10±0.05	0.11±0.05	0.10±0.05	0.10±0.05	0.10±0.05
RMLIF	0.11±0.04	0.11±0.04	0.09±0.04	0.09±0.04	0.09±0.04	0.09±0.05	0.09±0.05
MAPIF	0.16±0.06	0.16±0.06	0.16±0.06	0.17±0.06	0.18±0.06	0.18±0.06	0.19±0.07
RMAPIF	0.28±0.07	0.27±0.07	0.27±0.06	0.26±0.05	0.27±0.06	0.28±0.07	0.25±0.07
BMAP	0.45±0.15	0.41±0.14	0.38±0.12	0.35±0.10	0.37±0.11	0.40±0.13	0.44±0.17

Table 4.12: Scenario 1: Mean and standard deviation of RDMS values for -15 mm to +15 mm shift in x direction

	-15 mm	-10 mm	-6 mm	No Shift	+6 mm	+10 mm	+15 mm
Tikhonov 0	0.62±0.12	0.57±0.11	0.55±0.11	0.55±0.11	0.58±0.11	0.60±0.11	0.64±0.12
MLIF	0.31±0.06	0.31±0.06	0.30±0.06	0.31±0.06	0.31±0.06	0.31±0.06	0.31±0.06
RMLIF	0.30±0.06	0.30±0.06	0.30±0.06	0.30±0.06	0.30±0.06	0.30±0.06	0.31±0.06
MAPIF	0.24±0.07	0.24±0.07	0.24±0.07	0.24±0.07	0.24±0.07	0.24±0.07	0.25±0.07
RMAPIF	0.28±0.08	0.29±0.08	0.28±0.07	0.28±0.07	0.28±0.08	0.29±0.08	0.28±0.07
BMAP	0.47±0.16	0.43±0.14	0.41±0.13	0.38±0.11	0.40±0.11	0.43±0.13	0.48±0.17

Table 4.13: Scenario 2: Mean and standard deviation of RDMS values for -15 mm to +15 mm shift in x direction

	-15 mm	-10 mm	-6 mm	No Shift	+6 mm	+10 mm	+15 mm
Tikhonov 0	0.62±0.12	0.57±0.11	0.55±0.11	0.55±0.11	0.58±0.11	0.60±0.11	0.64±0.12
MLIF	0.70±0.20	0.66±0.19	0.62±0.19	0.58±0.19	0.58±0.18	0.59±0.17	0.60±0.18
RMLIF	0.66±0.18	0.61±0.16	0.57±0.15	0.56±0.15	0.57±0.15	0.58±0.15	0.59±0.16
MAPIF	0.57±0.09	0.53±0.08	0.50±0.07	0.49±0.07	0.50±0.08	0.51±0.09	0.52±0.10
RMAPIF	0.57±0.09	0.53±0.08	0.50±0.07	0.49±0.07	0.49±0.08	0.50±0.09	0.52±0.10
BMAP	0.59±0.11	0.54±0.10	0.53±0.10	0.53±0.09	0.57±0.10	0.60±0.12	0.64±0.14

Table 4.14: Scenario 3: Mean and standard deviation of RDMS values for -15 mm to +15 mm shift in x direction

Based on Table 4.9 and Table 4.10, the following observations are made for scenario 1 and scenario 2 when there is 15 mm shift:

- Tikhonov 0's correlation coefficient decreases by approximately 8%.

- BMAP's correlation coefficient decreases by approximately 8%.

- There is no significant change in the correlation coefficient of MLIF, RMLIF, MAPIF and RMAPIF.

Based on Table 4.11, the following observations are made for scenario 3 when there is 15 mm shift:

- Tikhonov 0's correlation coefficient decreases by approximately 8%.

- BMAP's correlation coefficient decreases by approximately 14%.

- MLIF's correlation coefficient decreases by approximately 16%.

- RMLIF's correlation coefficient decreases by approximately 14%.

- MAPIF's correlation coefficient decreases by approximately 12%.

- RMAPIF's correlation coefficient decreases by approximately 11%.
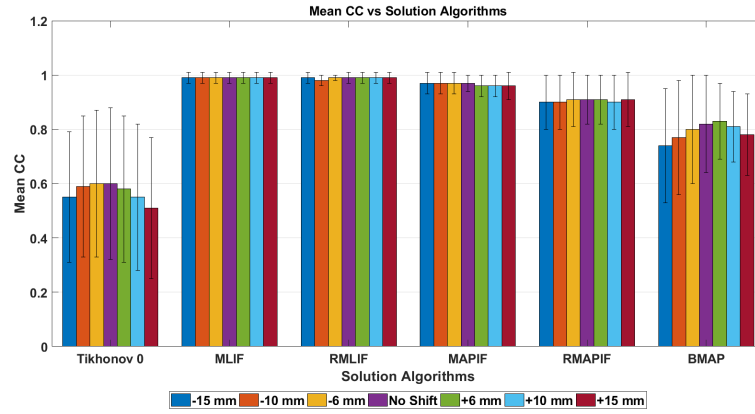
(a) Shift in x direction: Mean CC vs solution algorithms chart for scenario 1
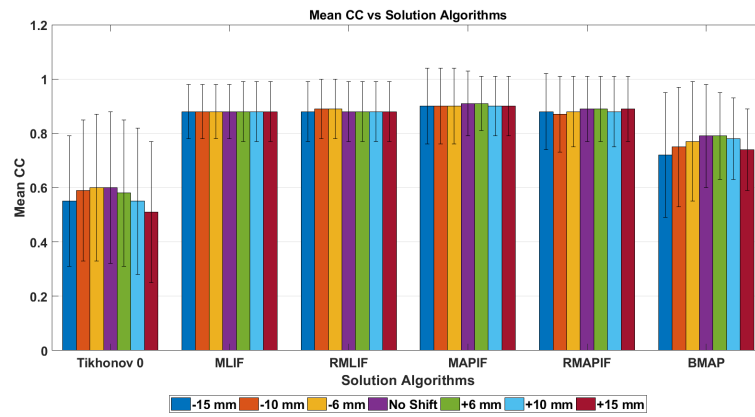
(b) Shift in x direction: Mean CC vs solution algorithms chart for scenario 2
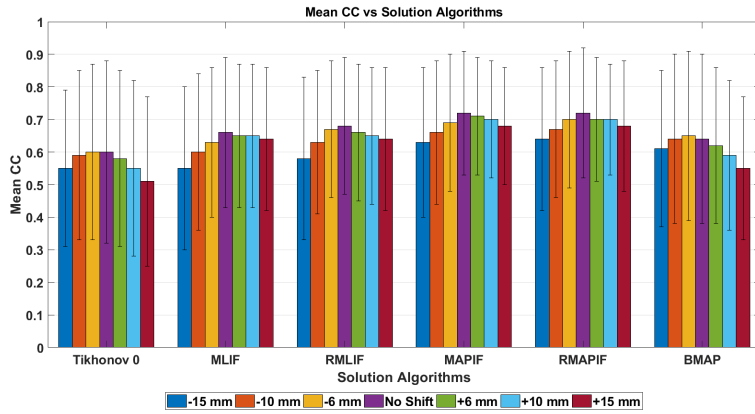
(c) Shift in x direction: Mean CC vs solution algorithms chart for scenario 3

Figure 4.33: Shift in x direction: Mean CC vs solution algorithms charts
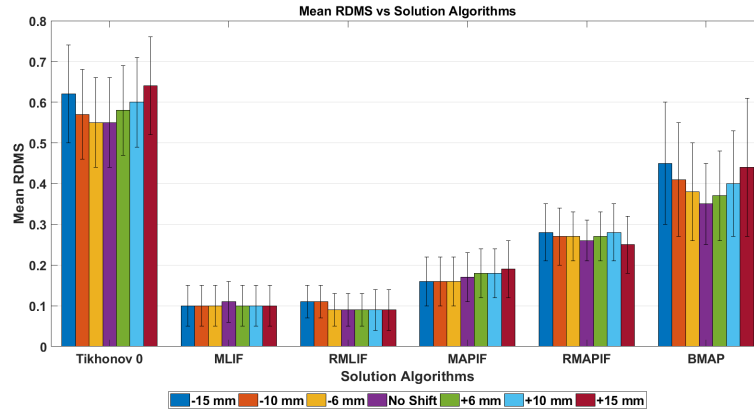
(a) Shift in x direction: Mean RDMS vs solution algorithms chart for scenario 1
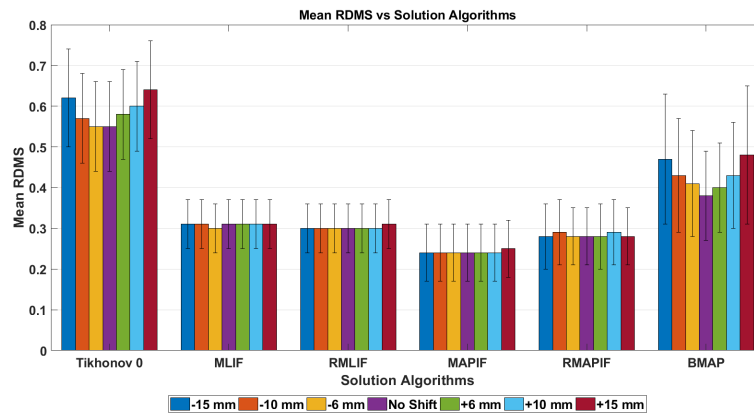
(b) Shift in x direction: Mean RDMS vs solution algorithms chart for scenario 2
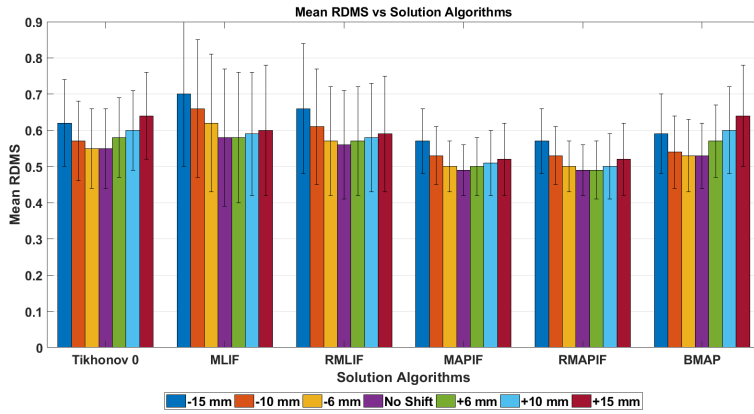
(c) Shift in x direction: Mean RDMS vs solution algorithms chart for scenario 3

Figure 4.34: Shift in x direction: Mean RDMS vs solution algorithms charts

Activation Times

Tables 4.15 - 4.17 show correlation coefficients of activation times for scenario 1, scenario 2 and scenario 3, respectively, when there is a shift in x direction by -15 mm to +15 mm from original position of the heart location. Figures 4.35a - 4.35c are bar chart representations of Tables 4.15 - 4.17.

	-15 mm	-10 mm	-6 mm	No Shift	+6 mm	+10 mm	+15 mm
Tikhonov 0	0.98	0.99	0.99	0.99	0.98	0.98	0.98
MLIF	0.99	0.99	0.99	0.99	0.99	0.99	0.99
RMLIF	0.99	0.99	0.99	0.99	0.99	0.99	0.99
MAPIF	0.99	0.99	0.99	0.99	0.99	0.99	0.99
RMAPIF	0.99	0.99	0.99	0.99	0.99	0.99	0.99
BMAP	0.98	0.99	0.99	0.99	0.99	0.99	0.99

Table 4.15: Scenario 1: Correlation coefficients of activation times for -15 mm to +15 mm shift in x direction

	-15 mm	-10 mm	-6 mm	No Shift	+6 mm	+10 mm	+15 mm
Tikhonov 0	0.98	0.99	0.99	0.99	0.98	0.98	0.98
MLIF	0.99	0.99	0.99	0.99	0.99	0.99	0.99
RMLIF	0.99	0.99	0.99	0.99	0.99	0.99	0.99
MAPIF	0.99	0.99	0.99	0.99	0.99	0.99	0.99
RMAPIF	0.99	0.99	0.99	0.99	0.99	0.99	0.99
BMAP	0.96	0.98	0.99	0.99	0.99	0.99	0.99

Table 4.16: Scenario 2: Correlation coefficients of activation times for -15 mm to +15 mm shift in x direction

	-15 mm	-10 mm	-6 mm	No Shift	+6 mm	+10 mm	+15 mm
Tikhonov 0	0.98	0.99	0.99	0.99	0.98	0.98	0.98
MLIF	0.98	0.99	0.99	0.99	0.99	0.99	0.99
RMLIF	0.98	0.99	0.99	0.99	0.99	0.99	0.99
MAPIF	0.97	0.98	0.98	0.99	0.99	0.99	0.99
RMAPIF	0.97	0.98	0.99	0.99	0.99	0.99	0.99
BMAP	0.96	0.98	0.99	0.99	0.99	0.98	0.98

Table 4.17: Scenario 3: Correlation coefficients of activation times for -15 mm to +15 mm shift in x direction
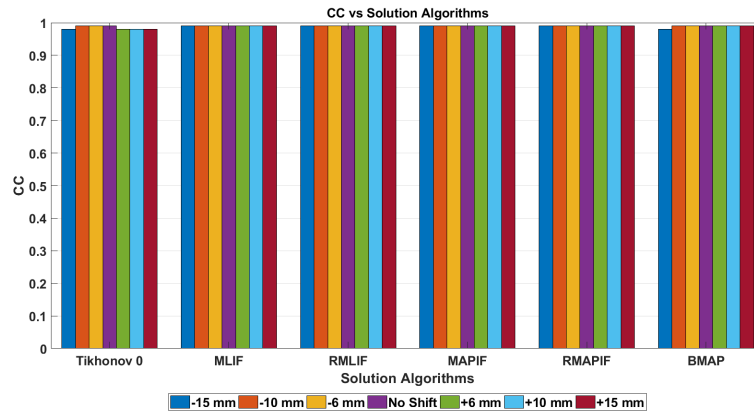
(a) Correlation coefficients of activation times vs solution algorithms chart for scenario 1
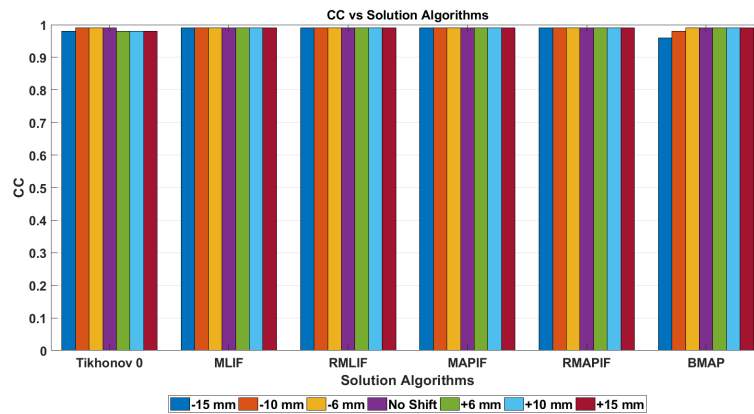
(b) Correlation coefficients of activation times vs solution algorithms chart for scenario 2
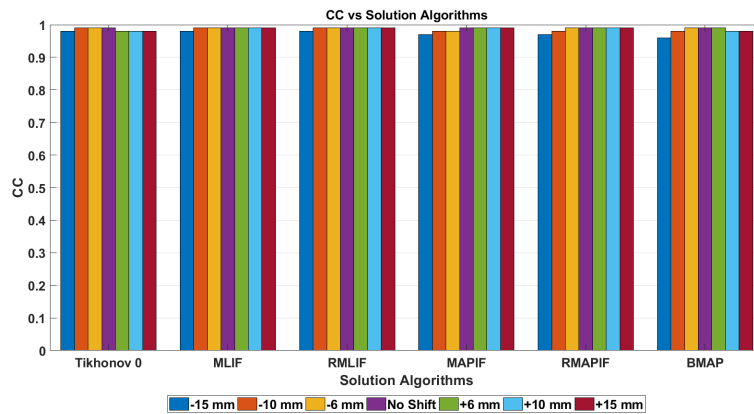
(c) Correlation coefficients of activation times vs solution algorithms chart for scenario 3

Figure 4.35: Correlation coefficients of activation times vs solution algorithms chart

As seen in Tables 4.15 - 4.17, there is no significant difference between the algorithms and all the algorithms are very robust to the shift error in terms of activation times.

Localization Error

Tables 4.18 - 4.20 show localization errors for scenario 1, scenario 2 and scenario 3, respectively, when there is a shift in x direction by -15 mm to +15 mm from original position of the heart location. Figures 4.36a - 4.36c are bar chart representations of Tables 4.18 - 4.20.

	-15 mm	-10 mm	-6 mm	No Shift	+6 mm	+10 mm	+15 mm
Tikhonov 0	7.03	10.43	10.43	14.04	14.04	14.04	9.44
MLIF	0	0	0	0	0	0	0
RMLIF	0	0	0	0	0	0	0
MAPIF	0	0	0	0	0	0	4.86
RMAPIF	0	0	0	0	4.86	4.86	4.86
BMAP	12.42	4.93	4.86	4.86	14.04	14.04	14.04

Table 4.18: Scenario 1: Localization errors (mm) for -15 mm to 15 mm shift in x direction

	-15 mm	-10 mm	-6 mm	No Shift	+6 mm	+10 mm	+15 mm
Tikhonov 0	7.03	10.43	14.79	14.79	14.04	14.04	9.44
MLIF	4.86	4.86	4.86	4.86	4.86	4.86	4.86
RMLIF	4.86	4.86	4.86	0	4.86	4.86	4.86
MAPIF	0	0	0	4.86	4.86	4.86	4.86
RMAPIF	4.80	4.80	0	4.86	4.86	4.86	0
BMAP	12.42	16.03	14.79	14.04	18.34	14.04	18.34

Table 4.19: Scenario 2: Localization errors (mm) for -15 mm to 15 mm shift in x direction

	-15 mm	-10 mm	-6 mm	No Shift	+6 mm	+10 mm	+15 mm
Tikhonov 0	7.03	10.43	10.43	14.04	14.04	14.04	9.44
MLIF	7.95	14.79	10.43	14.04	4.86	9.44	9.44
RMLIF	14.79	14.79	14.79	14.04	4.86	9.44	9.44
MAPIF	7.95	4.93	4.93	4.86	4.86	4.86	4.86
RMAPIF	4.93	4.93	4.93	4.86	4.86	4.86	4.86
BMAP	13.96	4.93	4.93	4.86	4.86	9.44	9.44

Table 4.20: Scenario 3: Localization errors (mm) for -15 mm to 15 mm shift in x direction

Based on Tables 4.18 - 4.20, the following observations are made:

- In scenario 1 and scenario 2, ML and MAP based spatio-temporal algorithms perform well and find the origin of the beat within a range of 4.86 mm.

- In scenario 3, ML and MAP based spatio-temporal algorithms find the origin of the beat within a range of 14.79 mm.

- In scenario 3, since the training set and the test beat come from different physiological models, localization errors are larger.

- Tikhonov 0 provides very sparse wave-fronts at the initial time frames, hence the algorithm that is used to find localization errors [136] does not perform well. Therefore, we see some inconsistencies in the results.

- Spatio-temporal approaches are more robust to the shift error in terms of localization error. When the training set and the test beat are similar, ML based spatio-temporal algorithms MLIF and RMLIF perform well. On the other hand, when the training set and the test beat are not similar, e.g., when they come from different physiological models as in scenario 3, MAP based spatio-temporal algorithms MAPIF and RMAPIF perform better.
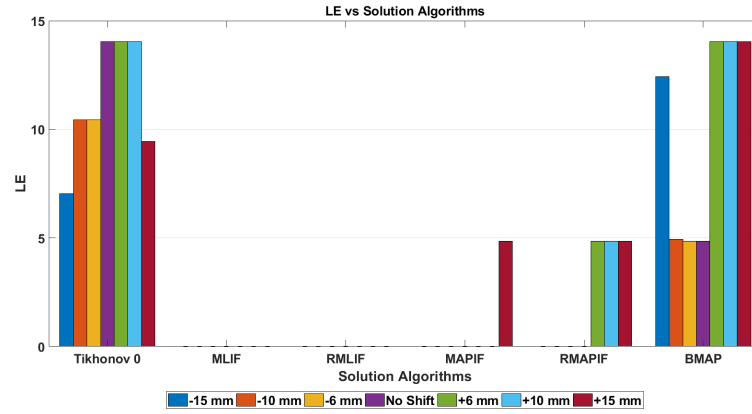
(a) Shift in x direction: LE (mm) vs solution algorithms chart for scenario 1
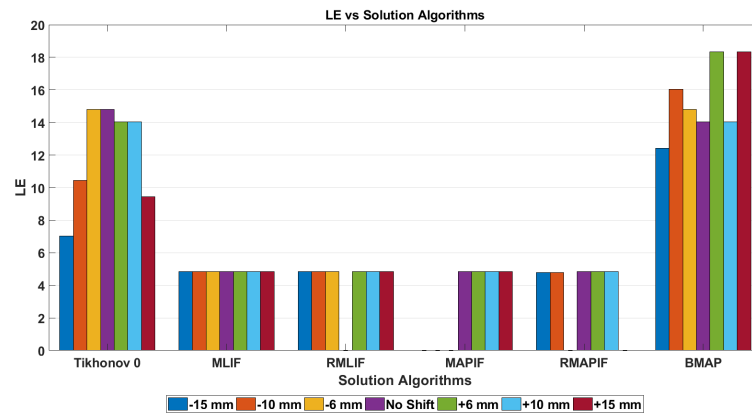
(b) Shift in x direction: LE (mm) vs solution algorithms chart for scenario 2
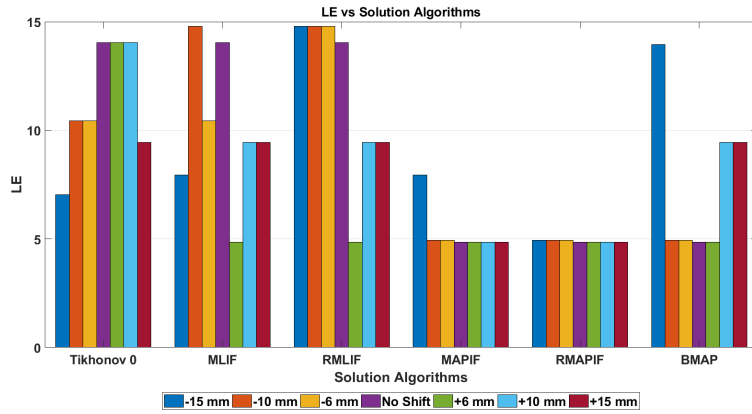
(c) Shift in x direction: LE (mm) vs solution algorithms chart for scenario 3

Figure 4.36: Shift in x direction: LE (mm) vs solution algorithms charts

4.6.1.2 Shift Error in the y Direction

Quantitative Evaluation of Electrograms

Tables 4.21 - 4.23 show mean and standard deviation of CC values, and Tables 4.24 - 4.26 show mean and standard deviation of RDMS values for scenario 1, scenario 2 and scenario 3, respectively, when there is a shift in y direction by -15 mm to +15 mm from original position of the heart location. Figures 4.37a - 4.38c are bar chart representations of Tables 4.21 - 4.26.

	-15 mm	-10 mm	-6 mm	No Shift	+6 mm	+10 mm	+15 mm
Tikhonov 0	0.52±0.27	0.57±0.27	0.59±0.28	0.60±0.28	0.59±0.27	0.57±0.26	0.53±0.24
MLIF	0.99±0.02	0.99±0.02	0.99±0.02	0.99±0.02	0.99±0.02	0.99±0.02	0.99±0.02
RMLIF	0.99±0.02	0.99±0.02	0.99±0.02	0.99±0.02	0.99±0.02	0.99±0.02	0.99±0.02
MAPIF	0.95±0.05	0.96±0.04	0.96±0.04	0.97±0.03	0.96±0.04	0.96±0.04	0.96±0.04
RMAPIF	0.88±0.13	0.89±0.12	0.90±0.11	0.91±0.09	0.90±0.10	0.89±0.10	0.88±0.10
BMAP	0.74±0.20	0.78±0.18	0.81±0.17	0.82±0.18	0.80±0.18	0.75±0.18	0.69±0.18

Table 4.21: Scenario 1: Mean and standard deviation of CC values for -15 mm to +15 mm shift in y direction

	-15 mm	-10 mm	-6 mm	No Shift	+6 mm	+10 mm	+15 mm
Tikhonov 0	0.52±0.27	0.57±0.27	0.59±0.28	0.60±0.28	0.59±0.27	0.57±0.26	0.53±0.24
MLIF	0.88±0.10	0.88±0.10	0.88±0.10	0.88±0.10	0.88±0.10	0.88±0.10	0.88±0.10
RMLIF	0.88±0.11	0.88±0.11	0.88±0.11	0.88±0.11	0.88±0.11	0.88±0.11	0.88±0.11
MAPIF	0.88±0.18	0.88±0.17	0.89±0.14	0.91±0.12	0.91±0.12	0.91±0.11	0.91±0.11
RMAPIF	0.86±0.16	0.87±0.16	0.88±0.14	0.89±0.12	0.88±0.13	0.89±0.12	0.88±0.13
BMAP	0.70±0.22	0.74±0.21	0.77±0.20	0.79±0.19	0.77±0.20	0.73±0.20	0.66±0.19

Table 4.22: Scenario 2: Mean and standard deviation of CC values for -15 mm to +15 mm shift in y direction

	-15 mm	-10 mm	-6 mm	No Shift	+6 mm	+10 mm	+15 mm
Tikhonov 0	0.52±0.27	0.57±0.27	0.59±0.28	0.60±0.28	0.59±0.27	0.57±0.26	0.53±0.24
MLIF	0.64±0.21	0.65±0.22	0.66±0.22	0.66±0.23	0.61±0.24	0.57±0.25	0.54±0.25
RMLIF	0.62±0.22	0.67±0.20	0.68±0.20	0.68±0.21	0.62±0.24	0.58±0.26	0.56±0.26
MAPIF	0.68±0.19	0.70±0.18	0.70±0.18	0.72±0.19	0.69±0.20	0.67±0.21	0.64±0.23
RMAPIF	0.66±0.21	0.70±0.18	0.72±0.18	0.72±0.20	0.68±0.22	0.68±0.20	0.66±0.21
BMAP	0.58±0.24	0.62±0.24	0.63±0.25	0.64±0.26	0.63±0.26	0.60±0.25	0.55±0.24

Table 4.23: Scenario 3: Mean and standard deviation of CC values for -15 mm to +15 mm shift in y direction

	-15 mm	-10 mm	-6 mm	No Shift	+6 mm	+10 mm	+15 mm
Tikhonov 0	0.63±0.13	0.59±0.11	0.56±0.11	0.55±0.11	0.57±0.11	0.59±0.11	0.64±0.11
MLIF	0.10±0.05	0.10±0.05	0.10±0.05	0.11±0.05	0.10±0.05	0.10±0.05	0.10±0.05
RMLIF	0.10±0.05	0.09±0.05	0.09±0.05	0.09±0.04	0.11±0.04	0.09±0.04	0.09±0.05
MAPIF	0.21±0.07	0.20±0.06	0.19±0.06	0.17±0.06	0.17±0.06	0.17±0.06	0.18±0.06
RMAPIF	0.29±0.08	0.28±0.07	0.28±0.07	0.26±0.05	0.28±0.07	0.29±0.08	0.30±0.09
BMAP	0.45±0.21	0.40±0.19	0.37±0.15	0.35±0.10	0.39±0.09	0.45±0.10	0.53±0.12

Table 4.24: Scenario 1: Mean and standard deviation of RDMS values for -15 mm to +15 mm shift in y direction

	-15 mm	-10 mm	-6 mm	No Shift	+6 mm	+10 mm	+15 mm
Tikhonov 0	0.63±0.13	0.59±0.11	0.56±0.11	0.55±0.11	0.57±0.11	0.60±0.11	0.64±0.11
MLIF	0.31±0.06	0.31±0.06	0.31±0.06	0.31±0.06	0.31±0.06	0.31±0.07	0.31±0.07
RMLIF	0.30±0.06	0.30±0.06	0.30±0.06	0.30±0.06	0.30±0.06	0.30±0.06	0.30±0.06
MAPIF	0.27±0.08	0.27±0.08	0.26±0.08	0.24±0.07	0.24±0.07	0.24±0.07	0.24±0.07
RMAPIF	0.31±0.08	0.30±0.08	0.29±0.07	0.28±0.07	0.28±0.07	0.28±0.08	0.29±0.09
BMAP	0.49±0.22	0.43±0.18	0.40±0.15	0.38±0.11	0.42±0.09	0.48±0.10	0.55±0.12

Table 4.25: Scenario 2: Mean and standard deviation of RDMS values for -15 mm to +15 mm shift in y direction

	-15 mm	-10 mm	-6 mm	No Shift	+6 mm	+10 mm	+15 mm
Tikhonov 0	0.63±0.13	0.59±0.11	0.56±0.11	0.55±0.11	0.57±0.11	0.59±0.11	0.64±0.11
MLIF	0.59±0.17	0.58±0.17	0.57±0.16	0.58±0.19	0.63±0.20	0.66±0.20	0.69±0.21
RMLIF	0.60±0.16	0.57±0.15	0.55±0.15	0.56±0.15	0.60±0.17	0.64±0.18	0.65±0.18
MAPIF	0.52±0.09	0.51±0.08	0.50±0.07	0.49±0.07	0.51±0.08	0.53±0.09	0.55±0.10
RMAPIF	0.54±0.09	0.50±0.07	0.49±0.07	0.49±0.07	0.52±0.08	0.52±0.09	0.54±0.10
BMAP	0.60±0.14	0.57±0.11	0.55±0.10	0.53±0.09	0.55±0.10	0.59±0.10	0.64±0.11

Table 4.26: Scenario 3: Mean and standard deviation of RDMS values for -15 mm to +15 mm shift in y direction

Based on Table 4.21 and Table 4.22, the following observations are made for scenario 1 and scenario 2 when there is 15 mm shift:

- Tikhonov 0's correlation coefficient decreases by approximately 13%.

- BMAP's correlation coefficient decreases by approximately 16%.

- There is no significant change in the correlation coefficient of MLIF, RMLIF, MAPIF and RMAPIF.

Based on Table 4.23, the following observations are made for scenario 3 when there is 15 mm shift:

- Tikhonov 0's correlation coefficient decreases by approximately 13%.

- BMAP's correlation coefficient decreases by approximately 14%.

- MLIF's correlation coefficient decreases by approximately 18%.

- RMLIF's correlation coefficient decreases by approximately 17%.

- MAPIF's correlation coefficient decreases by approximately 11%.

- RMAPIF's correlation coefficient decreases by approximately 8%.
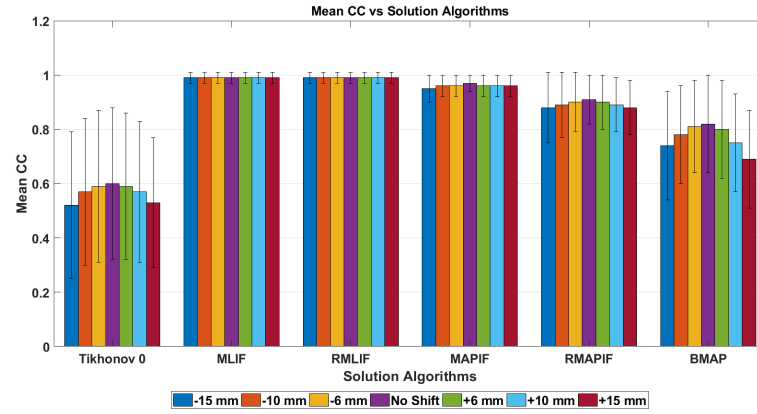
(a) Shift in y direction: Mean CC vs solution algorithms chart for scenario 1
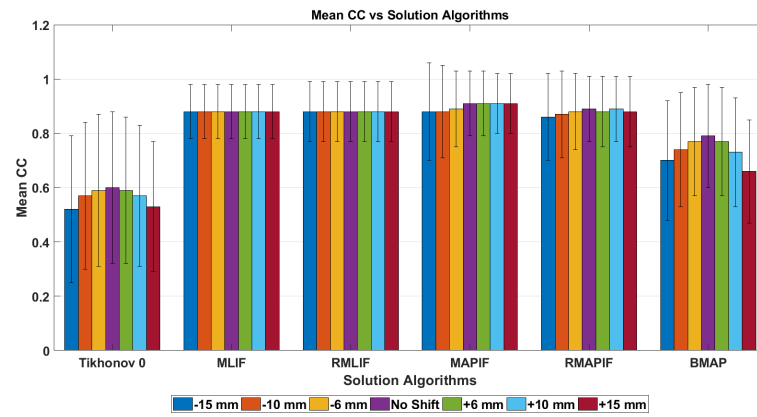
(b) Shift in y direction: Mean CC vs solution algorithms chart for scenario 2
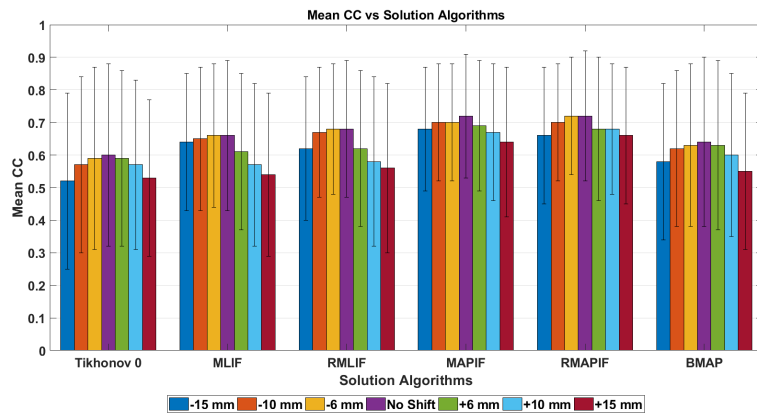
(c) Shift in y direction: Mean CC vs solution algorithms chart for scenario 3

Figure 4.37: Shift in y direction: Mean CC vs solution algorithms charts

(a) Shift in y direction: Mean RDMS vs solution algorithms chart for scenario 1

(b) Shift in y direction: Mean RDMS vs solution algorithms chart for scenario 2

(c) Shift in y direction: Mean RDMS vs solution algorithms chart for scenario 3

Figure 4.38: Shift in x direction: Mean RDMS vs solution algorithms charts

Activation Times

Tables 4.27 - 4.29 show correlation coefficients of activation times for scenario 1, scenario 2 and scenario 3, respectively, when there is a shift in y direction by -15 mm to +15 mm from original position of the heart location. Figures 4.39a - 4.39c are bar chart representations of Tables 4.27 - 4.29.

	-15 mm	-10 mm	-6 mm	No Shift	+6 mm	+10 mm	+15 mm
Tikhonov 0	0.99	0.99	0.99	0.99	0.99	0.99	0.95
MLIF	0.99	0.99	0.99	0.99	0.99	0.99	0.99
RMLIF	0.99	0.99	0.99	0.99	0.99	0.99	0.99
MAPIF	0.99	0.99	0.99	0.99	0.99	0.99	0.99
RMAPIF	0.99	0.99	0.98	0.99	0.99	0.99	0.99
BMAP	0.98	0.98	0.94	0.99	0.99	0.94	0.86

Table 4.27: Scenario 1: Correlation coefficients of activation times for -15 mm to +15 mm shift in y direction

	-15 mm	-10 mm	-6 mm	No Shift	+6 mm	+10 mm	+15 mm
Tikhonov 0	0.99	0.99	0.99	0.99	0.99	0.99	0.95
MLIF	0.99	0.99	0.99	0.99	0.99	0.99	0.99
RMLIF	0.99	0.99	0.99	0.99	0.99	0.99	0.99
MAPIF	0.99	0.99	0.99	0.99	0.99	0.99	0.99
RMAPIF	0.99	0.99	0.99	0.99	0.99	0.99	0.99
BMAP	0.98	0.98	0.99	0.99	0.98	0.94	0.84

Table 4.28: Scenario 2: Correlation coefficients of activation times for -15 mm to +15 mm shift in y direction

	-15 mm	-10 mm	-6 mm	No Shift	+6 mm	+10 mm	+15 mm
Tikhonov 0	0.99	0.99	0.99	0.99	0.99	0.99	0.95
MLIF	0.99	0.99	0.99	0.99	0.99	0.98	0.97
RMLIF	0.99	0.99	0.99	0.99	0.99	0.98	0.96
MAPIF	0.99	0.99	0.99	0.99	0.99	0.99	0.99
RMAPIF	0.99	0.99	0.99	0.99	0.99	0.99	0.99
BMAP	0.99	0.99	0.99	0.99	0.99	0.99	0.98

Table 4.29: Scenario 3: Correlation coefficients of activation times for -15 mm to +15 mm shift in y direction
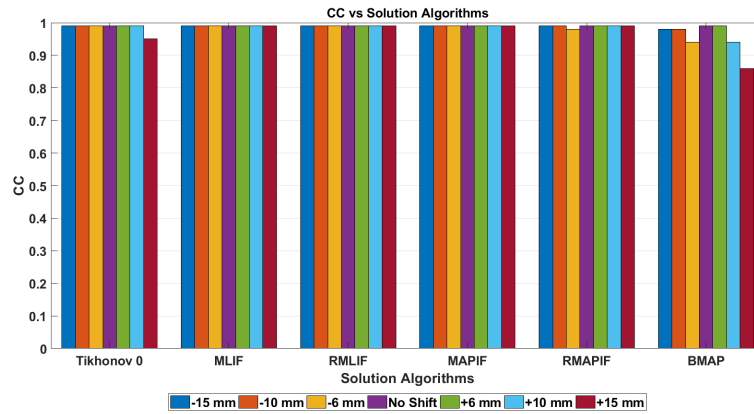
(a) Correlation coefficients of activation times vs solution algorithms chart for scenario 1
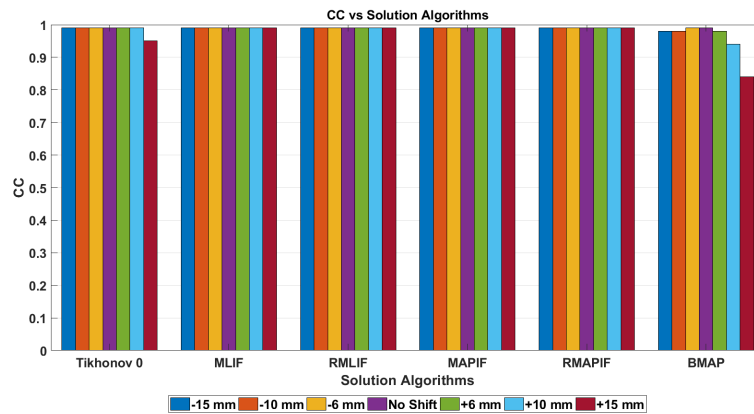
(b) Correlation coefficients of activation times vs solution algorithms chart for scenario 2
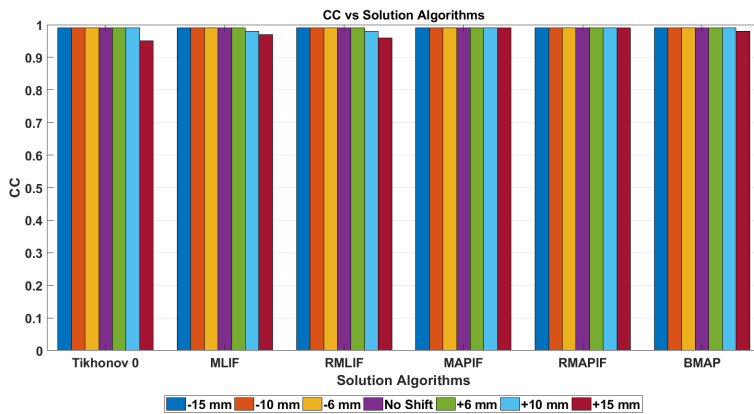
(c) Correlation coefficients of activation times vs solution algorithms chart for scenario 3

Figure 4.39: Correlation coefficients of activation times vs solution algorithms chart

As seen in Table 4.27 - 4.29, there is approximately 4% decrease in correlation co-efficients of activation times in scenario 1, scenario 2 and scenario 3 for Tikhonov 0. Furthermore, there is approximately 13% and 15% decrease in correlation coefficients of activation times in scenario 1 and scenario 2 for BMAP, respectively. On the other hand, there is no significant change in other algorithms.

Localization Error

Tables 4.30 - 4.32 show localization errors for scenario 1, scenario 2 and scenario 3, respectively, when there is a shift in y direction by -15 mm to +15 mm from original position of the heart location. Figures 4.40a - 4.40c are bar chart representations of Tables 4.30 - 4.32.

	-15 mm	-10 mm	-6 mm	No Shift	+6 mm	+10 mm	+15 mm
Tikhonov 0	4.86	4.86	4.86	14.04	14.04	14.04	15.07
MLIF	0	0	0	0	0	0	0
RMLIF	0	0	0	0	0	0	0
MAPIF	0	0	0	0	0	4.86	0
RMAPIF	4.86	4.86	0	0	4.86	4.86	4.86
BMAP	4.86	4.93	4.86	4.86	15.07	21.37	31.16

Table 4.30: Scenario 1: Localization errors (mm) for -15 mm to 15 mm shift in y direction

	-15 mm	-10 mm	-6 mm	No Shift	+6 mm	+10 mm	+15 mm
Tikhonov 0	4.86	4.86	4.86	14.79	14.04	14.04	15.07
MLIF	4.86	4.86	4.86	4.86	4.86	4.86	4.86
RMLIF	4.86	4.86	4.86	0	0	0	4.86
MAPIF	0	4.86	4.86	4.86	4.86	4.86	4.86
RMAPIF	4.86	4.86	4.86	4.86	0	0	0
BMAP	4.86	4.93	10.43	14.04	15.07	21.37	31.16

Table 4.31: Scenario 2: Localization errors (mm) for -15 mm to 15 mm shift in y direction

	-15 mm	-10 mm	-6 mm	No Shift	+6 mm	+10 mm	+15 mm
Tikhonov 0	4.86	4.86	4.86	14.04	14.04	14.04	15.07
MLIF	14.79	10.43	10.43	14.04	9.44	15.07	15.07
RMLIF	10.43	10.43	10.43	14.04	7.13	15.07	15.07
MAPIF	10.43	10.43	10.43	4.86	4.86	9.44	4.09
RMAPIF	10.43	10.43	10.43	4.86	4.86	9.44	4.09
BMAP	10.43	10.43	4.86	4.86	4.86	4.86	15.07

Table 4.32: Scenario 3: Localization errors (mm) for -15 mm to 15 mm shift in y direction

Based on Tables 4.30 - 4.32, the following observations are made:

- In scenario 1 and scenario 2, ML and MAP based spatio-temporal algorithms find the origin of the beat within a range of 4.86 mm.

- In scenario 3, ML and MAP based spatio-temporal algorithms find the origin of the beat within a range of 15.07 mm.

- In scenario 3, since the training set and the test beat come from different physiological models, localization errors are larger. Also in this scenario, due to different physiological models, most of the algorithms provide sparse wave-fronts at the initial frames. Therefore, some inconsistencies are observed in localization errors since sparser wave-fronts may yield incorrect results.

- Tikhonov 0 provides very sparse wave-fronts at the initial time frames, hence the algorithm that is used to find localization errors [136] does not perform well. Therefore, we see some inconsistencies in the results.

- Spatio-temporal approaches are more robust to the shift error in terms of localization error as in section 4.6.1.1.
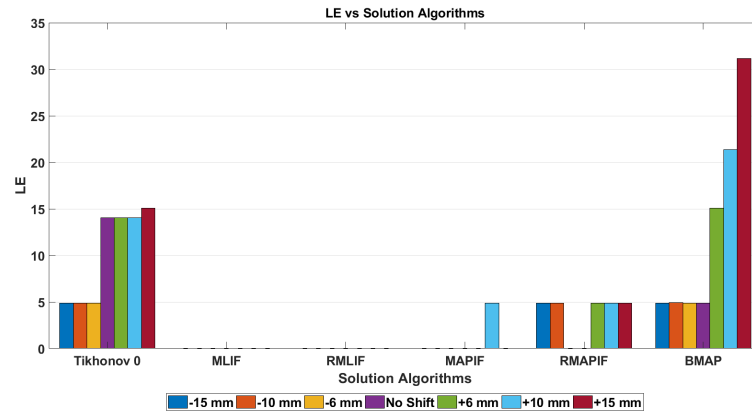
(a) Shift in y direction: LE (mm) vs solution algorithms chart for scenario 1
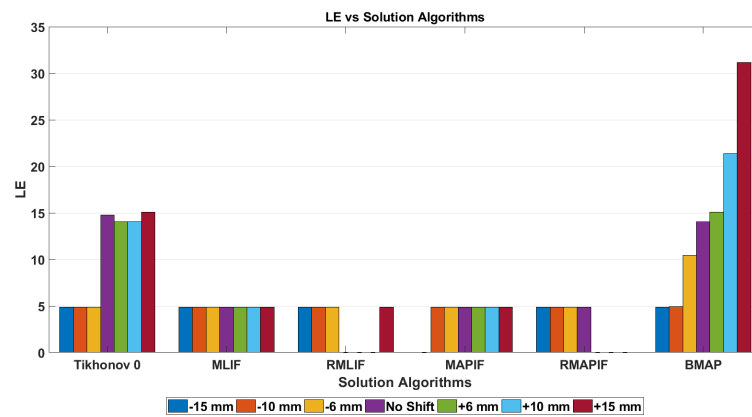
(b) Shift in y direction: LE (mm) vs solution algorithms chart for scenario 2
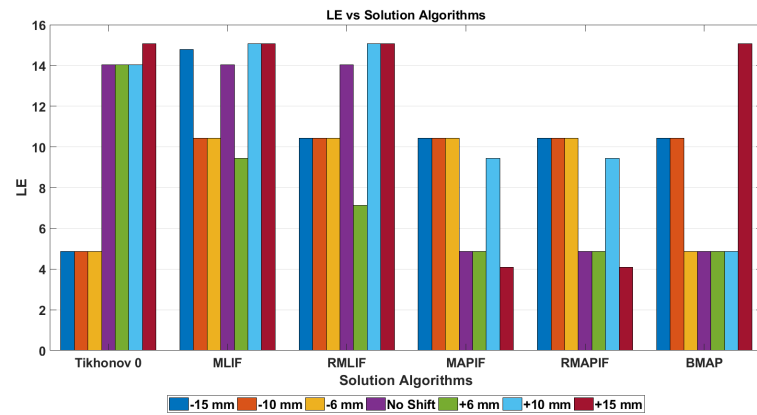
(c) Shift in y direction: LE (mm) vs solution algorithms chart for scenario 3

Figure 4.40: Shift in y direction: LE (mm) vs solution algorithms charts

117

4.6.1.3   Shift Error in the z Direction

Quantitative Evaluation of Electrograms

Tables 4.33 - 4.35 show mean and standard deviation of CC values, and Tables 4.36 - 4.14 show mean and standard deviation of RDMS values for scenario 1, scenario 2 and scenari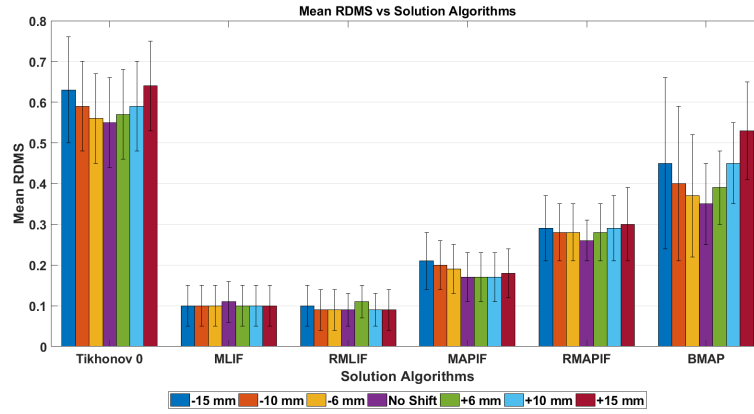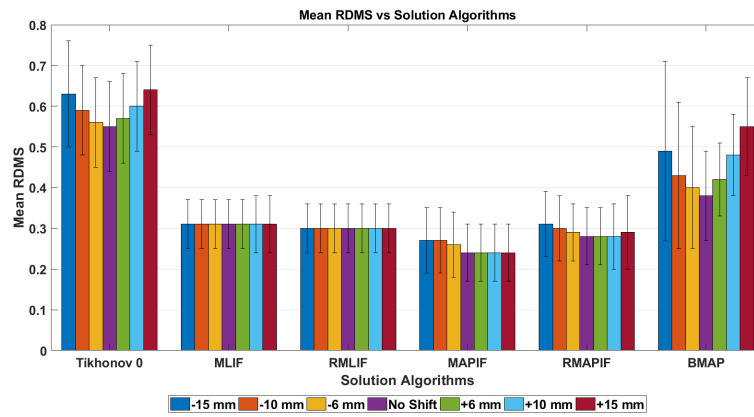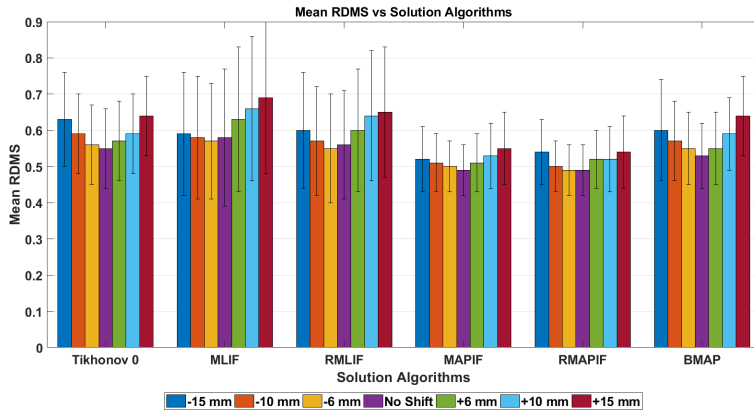o 3, respectively, when there is a shift in z direction by -15 mm to +15 mm from original position of the heart location.

	-15 mm	-10 mm	-6 mm	No Shift	+6 mm	+10 mm	+15 mm
Tikhonov 0	0.55±0.26	0.58±0.27	0.59±0.28	0.60±0.28	0.59±0.27	0.57±0.27	0.55±0.26
MLIF	0.99±0.02	0.99±0.02	0.99±0.02	0.99±0.02	0.99±0.02	0.99±0.02	0.99±0.02
RMLIF	0.99±0.01	0.99±0.01	0.99±0.01	0.99±0.02	0.99±0.02	0.99±0.02	0.99±0.02
MAPIF	0.96±0.03	0.97±0.03	0.97±0.03	0.97±0.03	0.96±0.04	0.96±0.04	0.96±0.04
RMAPIF	0.90±0.10	0.90±0.10	0.91±0.10	0.91±0.09	0.91±0.10	0.91±0.10	0.91±0.10
BMAP	0.82±0.14	0.83±0.16	0.83±0.17	0.82±0.18	0.79±0.20	0.76±0.20	0.72±0.22

Table 4.33: Scenario 1: Mean and standard deviation of CC values for -15 mm to +15 mm shift in z direction

	-15 mm	-10 mm	-6 mm	No Shift	+6 mm	+10 mm	+15 mm
Tikhonov 0	0.55±0.26	0.58±0.27	0.59±0.27	0.60±0.28	0.59±0.27	0.58±0.27	0.55±0.26
MLIF	0.88±0.10	0.88±0.10	0.88±0.10	0.88±0.10	0.88±0.10	0.88±0.10	0.88±0.10
RMLIF	0.88±0.11	0.88±0.11	0.88±0.11	0.88±0.11	0.88±0.11	0.88±0.11	0.88±0.11
MAPIF	0.90±0.12	0.90±0.13	0.90±0.13	0.91±0.12	0.90±0.13	0.91±0.12	0.90±0.12
RMAPIF	0.88±0.13	0.88±0.13	0.88±0.13	0.89±0.12	0.89±0.13	0.89±0.13	0.90±0.12
BMAP	0.77±0.19	0.79±0.20	0.80±0.20	0.79±0.19	0.76±0.20	0.74±0.21	0.70±0.22

Table 4.34: Scenario 2: Mean and standard deviation of CC values for -15 mm to +15 mm shift in z direction

	-15 mm	-10 mm	-6 mm	No Shift	+6 mm	+10 mm	+15 mm
Tikhonov 0	0.55±0.26	0.58±0.27	0.59±0.27	0.60±0.28	0.59±0.27	0.58±0.27	0.55±0.26
MLIF	0.65±0.23	0.65±0.24	0.66±0.24	0.66±0.23	0.65±0.22	0.64±0.22	0.63±0.21
RMLIF	0.65±0.23	0.65±0.23	0.66±0.23	0.68±0.21	0.67±0.20	0.63±0.22	0.64±0.20
MAPIF	0.71±0.18	0.71±0.19	0.71±0.19	0.72±0.19	0.70±0.19	0.69±0.20	0.67±0.21
RMAPIF	0.71±0.19	0.71±0.19	0.70±0.20	0.72±0.20	0.71±0.19	0.68±0.21	0.69±0.19
BMAP	0.62±0.24	0.64±0.25	0.65±0.25	0.64±0.26	0.63±0.25	0.60±0.25	0.57±0.24

Table 4.35: Scenario 3: Mean and standard deviation of CC values for -15 mm to +15 mm shift in z direction

	-15 mm	-10 mm	-6 mm	No Shift	+6 mm	+10 mm	+15 mm
Tikhonov 0	0.61±0.11	0.58±0.11	0.56±0.11	0.55±0.11	0.56±0.11	0.58±0.10	0.61±0.11
MLIF	0.10±0.05	0.10±0.05	0.10±0.05	0.11±0.05	0.10±0.05	0.10±0.05	0.10±0.05
RMLIF	0.10±0.04	0.09±0.04	0.09±0.04	0.09±0.04	0.09±0.05	0.10±0.04	0.09±0.04
MAPIF	0.18±0.05	0.18±0.05	0.18±0.05	0.17±0.06	0.17±0.06	0.17±0.07	0.18±0.07
RMAPIF	0.28±0.06	0.28±0.06	0.27±0.05	0.26±0.05	0.26±0.06	0.26±0.07	0.24±0.07
BMAP	0.38±0.10	0.35±0.09	0.34±0.09	0.35±0.10	0.39±0.12	0.43±0.14	0.47±0.16

Table 4.36: Scenario 1: Mean and standard deviation of RDMS values for -15 mm to +15 mm shift in z direction

	-15 mm	-10 mm	-6 mm	No Shift	+6 mm	+10 mm	+15 mm
Tikhonov 0	0.60±0.11	0.58±0.11	0.56±0.11	0.55±0.11	0.56±0.11	0.58±0.10	0.61±0.11
MLIF	0.31±0.07	0.31±0.06	0.31±0.06	0.31±0.06	0.31±0.06	0.31±0.06	0.31±0.06
RMLIF	0.30±0.06	0.30±0.06	0.30±0.06	0.30±0.06	0.30±0.06	0.30±0.06	0.30±0.06
MAPIF	0.25±0.06	0.25±0.06	0.25±0.06	0.24±0.07	0.24±0.08	0.24±0.07	0.24±0.08
RMAPIF	0.29±0.07	0.29±0.06	0.29±0.06	0.28±0.07	0.28±0.07	0.27±0.07	0.26±0.08
BMAP	0.42±0.11	0.39±0.10	0.37±0.10	0.38±0.11	0.42±0.13	0.46±0.15	0.50±0.18

Table 4.37: Scenario 2: Mean and standard deviation of RDMS values for -15 mm to +15 mm shift in z direction

	-15 mm	-10 mm	-6 mm	No Shift	+6 mm	+10 mm	+15 mm
Tikhonov 0	0.61±0.11	0.58±0.11	0.56±0.11	0.55±0.11	0.56±0.11	0.58±0.10	0.61±0.11
MLIF	0.59±0.18	0.58±0.19	0.57±0.19	0.58±0.19	0.59±0.19	0.60±0.19	0.62±0.20
RMLIF	0.56±0.15	0.57±0.17	0.56±0.16	0.56±0.15	0.57±0.15	0.61±0.17	0.61±0.17
MAPIF	0.49±0.08	0.49±0.07	0.49±0.07	0.49±0.07	0.50±0.08	0.51±0.08	0.52±0.09
RMAPIF	0.49±0.08	0.49±0.07	0.49±0.07	0.49±0.07	0.50±0.08	0.51±0.09	0.51±0.09
BMAP	0.57±0.11	0.54±0.10	0.53±0.09	0.53±0.09	0.56±0.10	0.58±0.10	0.62±0.11

Table 4.38: Scenario 3: Mean and standard deviation of RDMS values for -15 mm to +15 mm shift in z direction
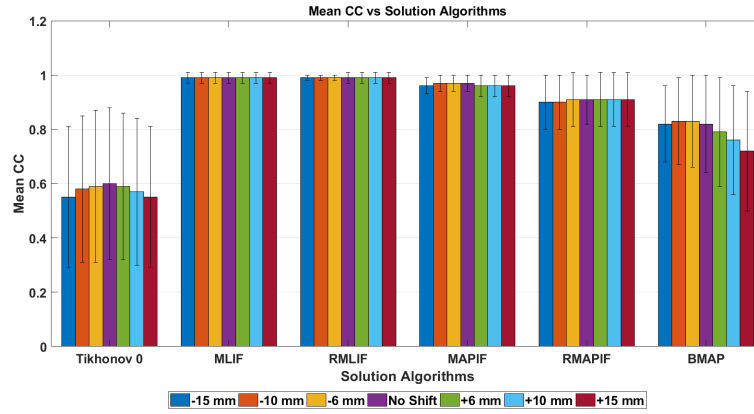
(a) Shift in z direction: Mean CC vs solution algorithms chart for scenario 1
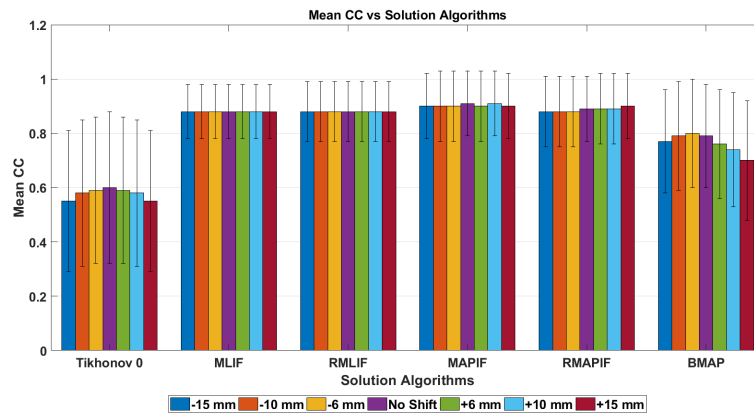
(b) Shift in z direction: Mean CC vs solution algorithms chart for scenario 2
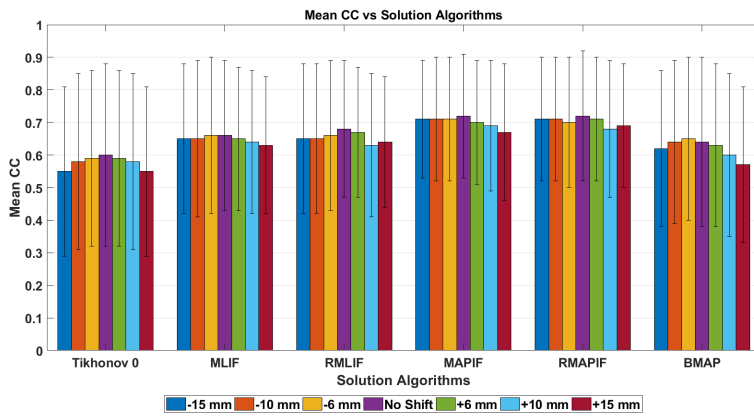
(c) Shift in z direction: Mean CC vs solution algorithms chart for scenario 3

Figure 4.41: Shift in z direction: Mean CC vs solution algorithms charts

(a) Shift in z direction: Mean RDMS vs solution algorithms chart for scenario 1

(b) Shift in z direction: Mean RDMS vs solution algorithms chart for scenario 2

(c) Shift in z direction: Mean RDMS vs solution algorithms chart for scenario 3

Figure 4.42: Shift in z direction: Mean RDMS vs solution algorithms charts

Based on Table 4.33 and Table 4.34, the following observations are made for scenario

121

1 and scenario 2 when there is 15 mm shift:

- Tikhonov 0's correlation coefficient decreases by approximately 8%.

- BMAP's correlation coefficient decreases by approximately 12%.

- There is no significant change in the correlation coefficient of MLIF, RMLIF, MAPIF and RMAPIF.

Based on Table 4.35, the following observations are made for scenario 3 when there is 15 mm shift:

- Tikhonov 0's correlation coefficient decreases by approximately 8%.

- BMAP's correlation coefficient decreases by approximately 10%.

- MLIF's correlation coefficient decreases by approximately 4%.

- RMLIF's correlation coefficient decreases by approximately 5%.

- MAPIF's correlation coefficient decreases by approximately 6%.

- RMAPIF's correlation coefficient decreases by approximately 4%.

Activation Times

Tables 4.39 - 4.41 show correlation coefficients of activation times for scenario 1, scenario 2 and scenario 3, respectively, when there is a shift in z direction by -15 mm to +15 mm from original position of the heart location. Figures 4.43a - 4.43c are bar chart representations of Tables 4.39 - 4.41.

	-15 mm	-10 mm	-6 mm	No Shift	+6 mm	+10 mm	+15 mm
Tikhonov 0	0.99	0.99	0.99	0.99	0.98	0.98	0.96
MLIF	0.99	0.99	0.99	0.99	0.99	0.99	0.99
RMLIF	0.99	0.99	0.99	0.99	0.99	0.99	0.99
MAPIF	0.99	0.99	0.99	0.99	0.99	0.99	0.99
RMAPIF	0.99	0.99	0.99	0.99	0.99	0.99	0.99
BMAP	0.98	0.99	0.99	0.99	0.99	0.99	0.98

Table 4.39: Scenario 1: Correlation coefficients of activation times for -15 mm to +15 mm shift in z direction

	-15 mm	-10 mm	-6 mm	No Shift	+6 mm	+10 mm	+15 mm
Tikhonov 0	0.99	0.99	0.99	0.99	0.98	0.98	0.96
MLIF	0.99	0.99	0.99	0.99	0.99	0.99	0.99
RMLIF	0.99	0.99	0.99	0.99	0.99	0.99	0.99
MAPIF	0.99	0.99	0.99	0.99	0.99	0.99	0.99
RMAPIF	0.99	0.99	0.99	0.99	0.99	0.99	0.99
BMAP	0.98	0.99	0.99	0.99	0.99	0.99	0.97

Table 4.40: Scenario 2: Correlation coefficients of activation times for -15 mm to +15 mm shift in z direction

	-15 mm	-10 mm	-6 mm	No Shift	+6 mm	+10 mm	+15 mm
Tikhonov 0	0.99	0.99	0.99	0.99	0.98	0.98	0.97
MLIF	0.99	0.99	0.99	0.99	0.99	0.99	0.99
RMLIF	0.98	0.99	0.99	0.99	0.99	0.99	0.99
MAPIF	0.99	0.99	0.99	0.99	0.99	0.99	0.99
RMAPIF	0.99	0.99	0.99	0.99	0.99	0.99	0.99
BMAP	0.99	0.99	0.99	0.99	0.99	0.98	0.98

Table 4.41: Scenario 3: Correlation coefficients of activation times for -15 mm to +15 mm shift in z direction

As seen in Tables 4.39 - 4.41, there is no significant difference between the algorithms and all the algorithms are very robust to the shift error in terms of activation times.
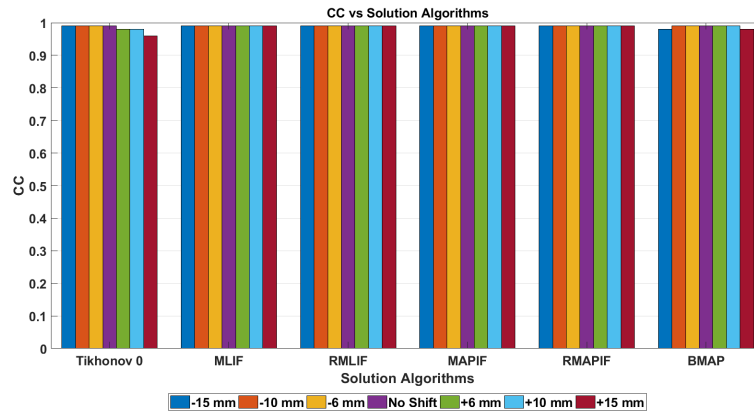
(a) Correlation coefficients of activation times vs solution algorithms chart for scenario 1
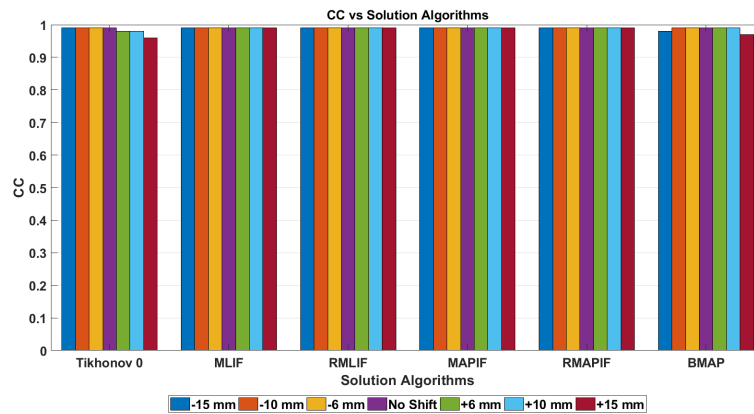
(b) Correlation coefficients of activation times vs solution algorithms chart for scenario 2
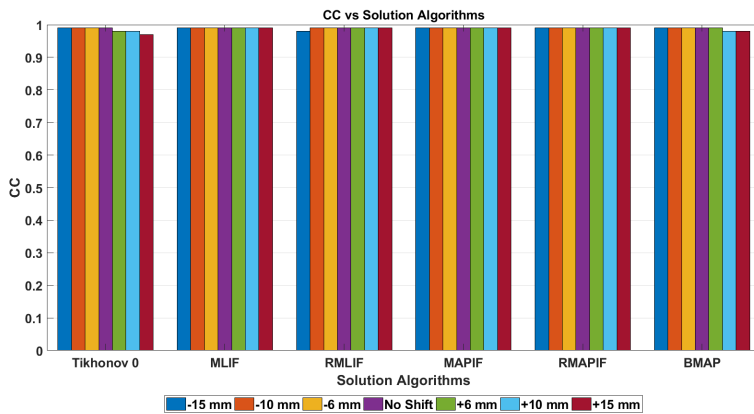
(c) Correlation coefficients of activation times vs solution algorithms chart for scenario 3

Figure 4.43: Correlation coefficients of activation times vs solution algorithms chart

Localization Error

Tables 4.42 - 4.44 show localization errors for scenario 1, scenario 2 and scenario 3, respectively, when there is a shift in z direction by -15 mm to +15 mm from original position of the heart location. Figures 4.44a - 4.44c are bar chart representations of Tables 4.42 - 4.44.

	-15 mm	-10 mm	-6 mm	No Shift	+6 mm	+10 mm	+15 mm
Tikhonov 0	14.04	14.04	14.04	14.04	14.04	15.07	10.96
MLIF	0	0	0	0	0	0	0
RMLIF	0	0	0	0	0	0	0
MAPIF	4.86	4.86	4.86	0	4.86	4.86	4.86
RMAPIF	4.86	4.86	4.86	0	0	4.86	4.86
BMAP	10.43	4.86	4.86	4.86	18.34	16.98	16.98

Table 4.42: Scenario 1: Localization errors (mm) for -15 mm to 15 mm shift in z direction

	-15 mm	-10 mm	-6 mm	No Shift	+6 mm	+10 mm	+15 mm
Tikhonov 0	14.04	14.04	14.0	14.79	14.04	15.07	10.96
MLIF	4.86	4.86	4.86	4.86	4.86	4.86	4.86
RMLIF	4.86	4.86	0	0	0	0	4.86
MAPIF	4.86	4.86	4.86	4.86	4.86	4.86	4.86
RMAPIF	0	4.86	4.86	4.86	4.86	4.86	4.86
BMAP	4.86	4.86	4.86	14.04	15.07	18.34	10.96

Table 4.43: Scenario 2: Localization errors (mm) for -15 mm to 15 mm shift in z direction

	-15 mm	-10 mm	-6 mm	No Shift	+6 mm	+10 mm	+15 mm
Tikhonov 0	14.04	14.04	14.79	14.04	14.04	9.44	10.96
MLIF	14.04	14.04	14.04	14.04	9.44	4.86	4.09
RMLIF	14.04	9.44	9.44	14.04	14.04	4.86	9.44
MAPIF	10.43	10.43	4.86	4.86	4.86	4.86	4.86
RMAPIF	10.43	10.43	4.86	4.86	4.86	4.86	4.86
BMAP	10.43	4.86	4.86	4.86	4.86	4.86	9.44

Table 4.44: Scenario 3: Localization errors (mm) for -15 mm to 15 mm shift in z direction

Based on Tables 4.42 - 4.44, the following observations are made:

- In scenario 1 and scenario 2, ML and MAP based spatio-temporal algorithms find the origin of the beat within a range of 4.86 mm.

- In scenario 3, ML and MAP based spatio-temporal algorithms find the origin of the beat within a range of 14.04 mm.

- In scenario 3, due to sparse wave-fronts at the initial frames, some inconsistencies are observed in localization errors.

- Spatio-temporal approaches are more robust to the shift error in terms of localization error as in section 4.6.1.1 and 4.6.1.2.
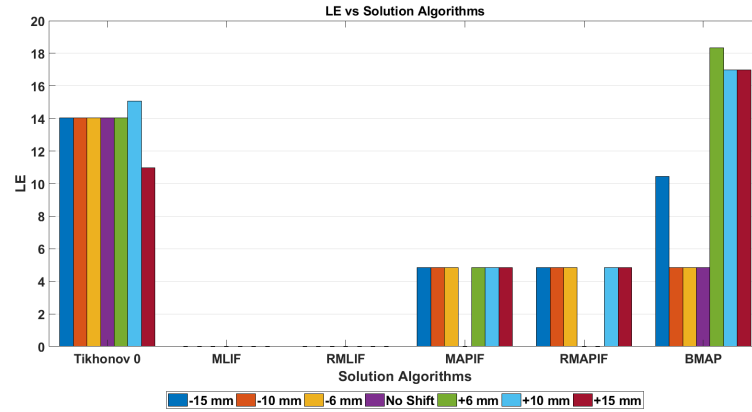
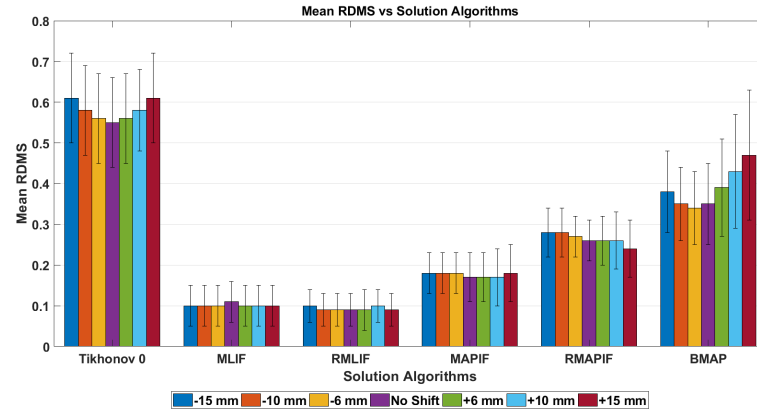(a) Shift in z direction: LE (mm) vs solution algorithms chart for scenario 1
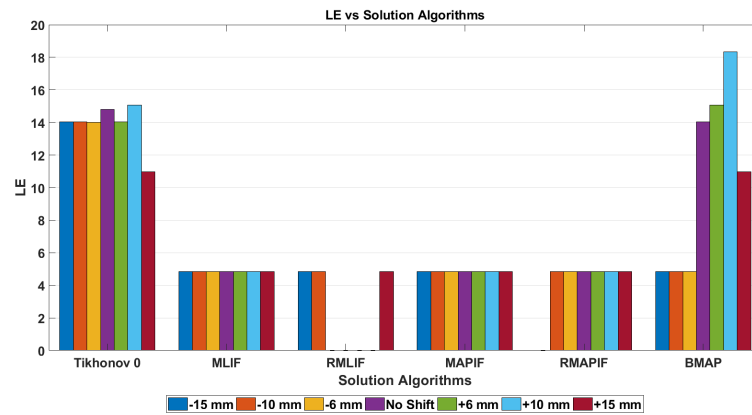
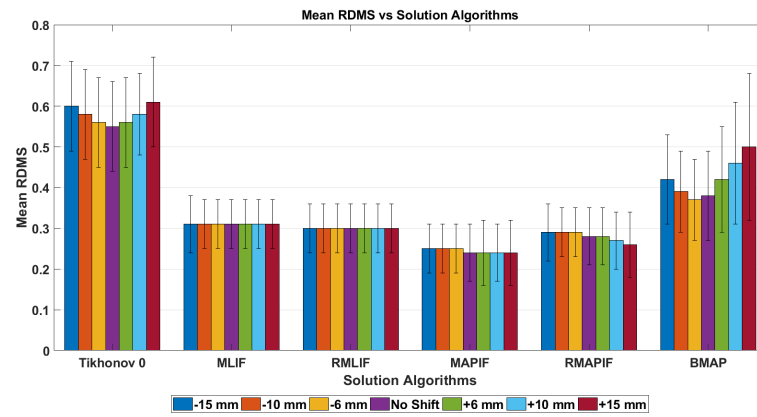(b) Shift in z direction: LE (mm) vs solution algorithms chart for scenario 2
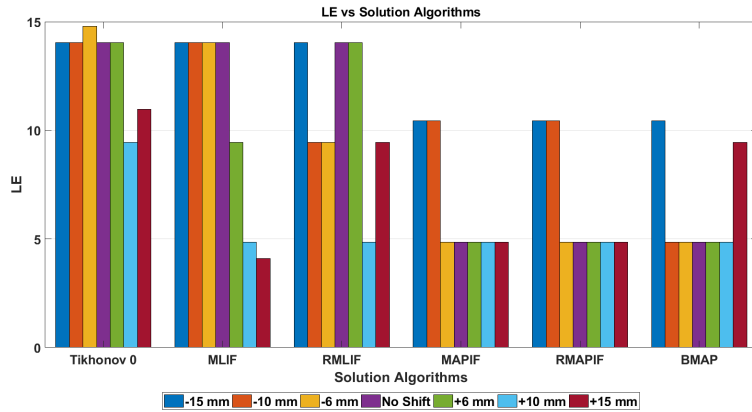
(c) Shift in z direction: LE (mm) vs solution algorithms chart for scenario 3
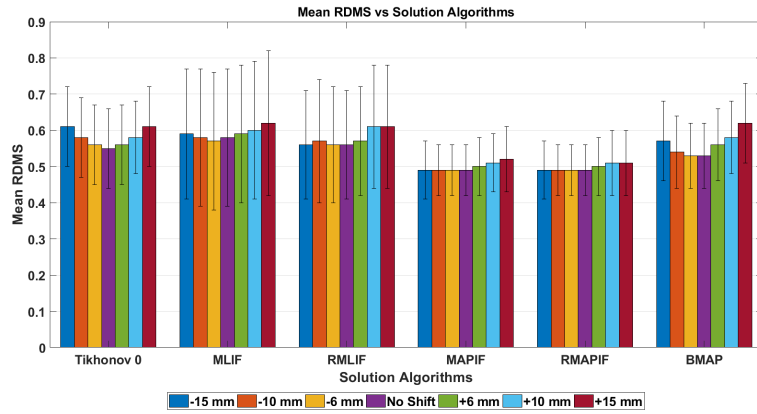
Figure 4.44: Shift in z direction: LE (mm) vs solution algorithms charts

4.6.1.4 Discussion of the Results

To investigate the sensitivity of the proposed algorithms to erroneous forward transfer matrix H, we follow the same procedure as in section 4.5.5. We start by rewriting the state covariance equation (4.6):

$$P_{k|k} = (I - K_k H)F P_{k-1|k-1} F^T (I - K_k H)^T + (I - K_k H)Q(I - K_k H)^T + K_k R K_k^T$$
(4.11)

The sensitivity of the Kalman filter is related to $tr(P_{k|k})$ [142] and when there is a perturbation in H, using Turnbull's matrix form of Taylor expansion [143], the trace of the state covariance is found as follows:

$$tr(P(H+\delta)) = tr(P(H)) + \frac{\partial}{\partial H} tr(P(H))\delta + \frac{\partial^2}{\partial H^2} tr(P(H))\frac{\delta^2}{2} + \mathbf{H \cdot O \cdot T} \quad (4.12)$$

Under the assumption of small deviations from H, we neglect the second and higher order terms. For convenience, we take the derivative of each term on the right hand side in equation (4.6) separately and add them up:

$$\frac{\partial}{\partial H} tr\Big((I - K_k H)F P_{k-1|k-1} F^T (I - K_k H)^T \Big)$$
$$= \frac{\partial}{\partial H} tr\Big((F P_{k-1|k-1} F^T - K_k H F P_{k-1|k-1} F^T)(I - H^T K_k^T) \Big)$$
$$= \frac{\partial}{\partial H} tr\Big(F P_{k-1|k-1} F^T - K_k H F P_{k-1|k-1} F^T - F P_{k-1|k-1} F^T H^T K_k^T$$
$$+ K_k H F P_{k-1|k-1} F^T H^T K_k^T \Big)$$
$$= -K_k^T F P_{k-1|k-1}^T F^T - K_k^T F P_{k-1|k-1} F^T + K_k^T K_k H F P_{k-1|k-1}^T F^T$$
$$+ K_k^T K_k H F P_{k-1|k-1} F^T$$
$$= -2K_k^T F P_{k-1|k-1} F^T + 2K_k^T K_k H F P_{k-1|k-1} F^T \quad (4.13)$$

$$\frac{\partial}{\partial H} tr\Big((I - K_k H)Q(I - K_k H)^T \Big) = \frac{\partial}{\partial H} tr\Big((Q - K_k H Q)(I - H^T K_k^T) \Big)$$
$$= \frac{\partial}{\partial H} tr\Big(Q - K_k H Q - Q H^T K_k^T + K_k H Q H^T K_k^T \Big)$$
$$= -K_k^T Q^T - K_k^T Q + K_k^T K_k H Q^T + K_k^T K_k H Q$$
$$= -2K_k^T Q + 2K_k^T K_k H Q \quad (4.14)$$

Overall, we obtained:

$$\frac{\partial}{\partial H} tr(P_{k|k}) = -2K_k^T F P_{k-1|k-1} F^T + 2K_k^T K_k H F P_{k-1|k-1} F^T - 2K_k^T Q$$
$$+ 2K_k^T K_k H Q \quad (4.15)$$

In light of the discussion above, we can conclude that the value of equation (4.15) determines the Kalman filter sensitivity to parameter H.

In general, for scenario 1 and scenario 2, ML based algorithms MLIF, RMLIF and MAP based algorithms MAPIF, RMAPIF are very robust to erroneous H matrix. The reason behind this can be seen by examining the sensitivity equation:

$$tr(P(H + \delta)) = tr(P(H)) + (-2K_k^T F P_{k-1|k-1} F^T + 2K_k^T K_k H F P_{k-1|k-1} F^T - 2K_k^T Q + 2K_k^T K_k H Q)\delta$$

(4.16)

The second term on the right hand side of the above equation determines the sensitivity, as mentioned before. The Kalman gain is low in scenario 1 and scenario 2, and the value of the sensitivity equation goes to zero. Therefore, we expect zero or very low sensitivity to erroneous H matrix and this expectation conforms with the results.

In scenario 3, the Kalman gain is higher as compared to other scenarios. Hence, the sensitivity of ML and MAP based algorithms are higher in scenario 3.

Tikhonov 0 and BMAP algorithms are the most suffering algorithms from the geometric shift errors whereas BMAP algorithm is more robust than Tikhonov 0 algorithm since it uses statistical prior information on epicardial potential distribution. The reason behind the poor performances of these two algorithms is due to the fact that these two algorithms do not use temporal correlations.

In terms of the sensitivity, some of the proposed methods are more sensitive to the shift errors in different directions. This may caused by electrode positions on the heart and the body.

CHAPTER 5

CONCLUSION AND FUTURE WORK

5.1 Conclusions

In this study, the inverse electrocardiography problem was solved by using spatial and spatio-temporal techniques. The following methods were used in this thesis:

- Spatial methods: Zero order Tikhonov regularization and Bayesian maximum a posteriori estimation.

- Spatio-temporal methods: Kalman filter and regularized Kalman filter. For parameter estimation in these methods, ML and MAP methods were adopted, yielding four different solution approaches: Maximum Likelihood Inference & Filtering, Regularized Maximum Likelihood Inference & Filtering, Maximum a Posteriori Inference & Filtering and Regularized Maximum a Posteriori Inference & Filtering.

The proposed methods were compared with each other by using different training sets. Three different training sets were used in this study:

- Training Set 1 (Scenario 1): The test beat and the training set originate from the same physiological models, and the test beat was included in the training set.

- Training Set 2 (Scenario 2): The test beat and the training set originate from the same physiological models, and the test beat was excluded from the training set.

- Training Set 3 (Scenario 3): The test beat and the training set originate from

different physiological models, meaning that they are from different dog experiments.

We evaluated the performances of the proposed methods under different measurement noise levels and when a geometric error was presented to the system.

Under moderate noise conditions (30 dB SNR), in scenario 1 and scenario 2, ML based algorithms outperformed the other algorithms due to their low process noise covariance matrix and a good training set. In scenario 3, ML based algorithms' performances were degraded due to the over-fitting nature of the ML estimation and MAP based algorithms outperformed the other algorithms due to their high process noise covariances.

Next, sensitivity of the methods to increasing measurement noise levels was evaluated. Three measurement noise levels were used to test the noise robustness: 10 dB, 15 dB and 30 dB SNR. The sensitivity was related to the Kalman gain and determined by equation (4.9). According to equation (4.9), higher Kalman gains increase the sensitivity to the measurement noise, i.e. the robustness decreases with increasing Kalman gain. ML based algorithms had low Kalman gains due to their low process noise covariance matrix, hence, ML based algorithms had low sensitivity to the measurement noise. MAP based algorithms' Kalman gains were higher than ML based algorithms, therefore, their robustness to the measurement were low.

The sensitivity of the methods to the geometric errors was also evaluated in this study. To simulate the geometric errors, the location of the heart was shifted by -15 mm to +15 mm in x, y and z directions. The sensitivity to the geometric errors was determined by equation (4.15). In scenario 1 and scenario 2, the value of equation (4.15) was close to zero, hence ML and MAP based algorithms were very robust to the geometric shift errors. On the other hand, in scenario 3, since the Kalman gains were higher due to bad training set, the algorithms were less robust to the geometric shift errors.

In general, spatio-temporal methods outperformed spatial methods and enhanced the reconstruction accuracy. Comparison of spatio-temporal methods showed that when the training set data and the test beat were similar, finding Kalman filter's parameters

with maximum likelihood estimation yielded better results. However, due to over-fitting, if the training set data and the test beat were not similar, i.e., if they came from different physiological models, the performance of maximum likelihood estimation was degraded. In such situations, maximum a posteriori estimation can be used to overcome the over-fitting issue [138].

5.2   Limitations of the Study

There are number of limitations in this study. These limitations can be listed as follows:

- Since the body surface measurements were not available in this study, we worked with the simulated data.

- The torso geometry used in this study was simple and only the lungs were included in the medium between the heart and the body.

- The training set used in this study was limited. Also, the training set experiments and their QRS complexes were selected manually.

5.3   Future Works

The following topics can be considered as the future work:

- In this study, we worked with simulated body surface potentials. Working with real body surface potential measurements can show the feasibility of our approaches in clinic applications.

- We worked with closed form solutions in this study. Other solution approaches such as Markov Chain Monte Carlo (MCMC) or Variational Bayes (VB) can also be used.

REFERENCES

[1] WHO. The top 10 causes of death, 2017.

[2] Paul A. Iaizzo. *Handbook of cardiac anatomy, physiology, and devices, third edition*. 2015.

[3] David M. Mirvis. What's Wrong With Electrocardiography? 31(4):313–316, 1998.

[4] J. Gordon Betts. *Anatomy & Physiology*. OpenStax College, Rice University, Houston, Texas, 2013.

[5] A. Despopoulos and S. Silbernagl. *Color atlas of physiology*. 2003.

[6] Fei Wang, Tanveer Syeda-Mahmood, and David Beymer. Information Extraction from Multimodal ECG Documents, 2009.

[7] R. L. Lux, R. S. MacLeod, M. Fuller, L. S. Green, and F. Kornreich. Estimating ECG distributions from small numbers of leads. *Journal of Electrocardiology*, 28:92–98, 1995.

[8] D.H. Brooks and R.S. MacLeod. Electrical Imaging of the Heart. *IEEE Signal Processing Magazine*, 14(1):24 – 42, 1997.

[9] Robert L. Lux, Creig R. Smith, Roland F. Wyatt, and J. A. Abildskov. Limited Lead Selection for Estimation of Body Surface Potential Maps in Electrocardiography. *IEEE Transactions on Biomedical Engineering*, BME-25(3):270–276, 1978.

[10] Luigi De Ambroggi and Alexandru Dan Corlan. Clinical use of body surface potential mapping in cardiac arrhythmias. *Anatol J Cardiol*, 7(0):8–10, 2007.

[11] Yoram Rudy. The Forward Problem of Electrocardiography Revisited. *Circulation: Arrhythmia and Electrophysiology*, 8(3):526–528, 2015.

[12] Rok Hren, Jukka Nenonen, and B. Milan Horáček. Simulated epicardial potential maps during paced activation reflect myocardial fibrous structure. *Annals of Biomedical Engineering*, 26(6):1022–1035, 1998.

[13] R.S. MacLeod and D.H. Brooks. Recent progress in inverse problems in Electrocardiology. *IEEE Engineering in Medicine and Biology Magazine*, 17(1):73–83, 1998.

[14] C R Johnson, R Macleod, and P R Ershler. A computer model for the study of electrical current flow in the human thorax. *Comput. Biol. Med.*, 22(5):305–23, 1992.

[15] J A Schmidt, C R Johnson, J C Eason, and R S Macleod. Applications of Automatic Mesh Generation and Adaptive Methods in Computational Medicine. In Ivo Babuska, William D Henshaw, Joseph E Oliger, Joseph E Flaherty, John E Hopcroft, and Tayfun Tezduyar, editors, *Modeling, Mesh Generation, and Adaptive Numerical Methods for Partial Differential Equations*, pages 367–393, New York, NY, 1995. Springer New York.

[16] S Babaeizadeh, D H Brooks, and D Isaacson. Electrical impedance tomography using a 3-D boundary element inverse solution. In *Conference Record of the Thirty-Eighth Asilomar Conference on Signals, Systems and Computers, 2004.*, volume 2, pages 1595–1599 Vol.2, nov 2004.

[17] H Griffiths and Z Zhang. Dual-frequency electrical impedance tomography in vitro and in vivo. In *Images of the Twenty-First Century. Proceedings of the Annual International Engineering in Medicine and Biology Society*, pages 476–477 vol.2, nov 1989.

[18] A.W. Maurits van der Graaf, Pranav Bhagirath, Hemanth Ramanna, Vincent J.H.M. van Driel, Jacques de Hooge, Natasja M.S. de Groot, and Marco J. W. Götte. Noninvasive Imaging of Cardiac Excitation: Current Status and Future Perspective. *Annals of Noninvasive Electrocardiology*, 19(2):105–113, 2014.

[19] Heinz Antes. A Short Course on Boundary Element Methods. nov 2010.

[20] M. Seger, G. Fischer, R. Modre, B. Messnarz, F. Hanser, and B. Tilg. Lead field computation for the electrocardiographic inverse problem - Finite elements versus boundary elements. *Computer Methods and Programs in Biomedicine*, 77(3):241–252, 2005.

[21] R C Barr, M Ramsey, and M S Spach. Relating Epicardial to Body Surface Potential Distributions by Means of Transfer Coefficients Based on Geometry Measurements. *IEEE Transactions on Biomedical Engineering*, BME-24(1):1–11, jan 1977.

[22] G Fairweather and A Karageorghis. The method of fundamental solutions for elliptic boundary value problems. *Advances in Computational Mathematics*, 9(1):69–95, 1998.

[23] Yong Wang and Yoram Rudy. Meshless methods in potential inverse electrocardiography. *Annual International Conference of the IEEE Engineering in Medicine and Biology - Proceedings*, pages 2558–2559, 2006.

[24] R C Barr, M S Spach, and G S Herman-Giddens. Selection of the Number and Positions of Measuring Locations for Electrocardiography. *IEEE Transactions on Biomedical Engineering*, BME-18(2):125–138, 1971.

[25] David B. Geselowitz. On Bioelectric Potentials in an Inhomogeneous Volume Conductor. *Biophysical Journal*, 7(1):1–11, 1967.

[26] Yasuo Yamashita. Theoretical Studies on the Inverse Problem in Electrocardiography and the Uniqueness of the Solution. *IEEE Transactions on Biomedical Engineering*, BME-29(11):719–725, 1982.

[27] Jaakko Malmivuo Jari Hyttinen, Noriyuki Takano, Pasi Kauppinen. Estimation of the number of dipole sources for accurate simulation of electrocardiography. *Journal of Electrocardiology*, 31(X):31, 1998.

[28] W Einthoven, G Fahr, and A de Waart. On the direction and manifest size of the variations of potential in the human heart and on the influence of the position of the heart on the form of the electrocardiogram. *American Heart Journal*, 40(2):163–211, aug 1950.

[29] C. K. Gordon Yeh and Johann Martinek. Comparison of surface potentials due to several singularity representations of the human heart. *The bulletin of mathematical biophysics*, 19(4):293–308, 1957.

[30] Otto H Schmitt, Raphael B Levine, and Ernst Simonson. Electrocardiographic mirror pattern studies. I. *American Heart Journal*, 45(3):416–428, 1953.

[31] Raphael B Levine, Otto H Schmitt, and Ernst Simonson. Electrocardiographic mirror pattern studies. II. *American Heart Journal*, 45(4):500–518, 1953.

[32] Ernst Simonson, Otto H. Schmitt, Raphael B. Levine, and James Dahl. Electrocardiographic mirror pattern studies. III. *American Heart Journal*, 45(5):655–664, 1953.

[33] D. B. Geselowitz. Multipole Representation for an Equivalent Cardiac Generator. *Proceedings of the IRE*, 48(1):75–79, 1960.

[34] Daniel A Brody. The Inverse Determination of Simple Generator Configurations from Equivalent Dipole and Multipole Information. *IEEE Transactions on Biomedical Engineering*, BME-15(2):106–110, 1968.

[35] Y. Kim and W. J. Tompkins. Forward and inverse high-frequency electrocardiography. *Medical & Biological Engineering & Computing*, 19(1):11–22, 1981.

[36] P De Muynck, J Cornelis, and L I Titomir. Multipole approach to the inverse problem in electrocardiology: convergence of the multipole equivalent generator on the inhomogeneous body conductor. *Bulletin of mathematical biology*, 62(3):543–83, 2000.

[37] M. Stuart Lynn, Anthony C. Barnard, J H Holt, and L T Sheffield. A proposed method for the inverse problem in electrocardiology. *Biophysical journal*, 7(6):925–45, 1967.

[38] T.C. Rogers, C.L., Pilkington. Free-Moment Current Dipoles in Inverse Electrocardiography. *IEEE Transactions on Biomedical Engineering*, 15(4):312–323, 1968.

[39] R. Bellman, B. Kashef, and R. Vasudevan. The inverse problem of estimating heart parameters from cardiograms. *Mathematical biosciences*, 19(3-4):221–230, 1974.

[40] Y. Yamashita. Inverse Solution in Electrocardiography: Determining Epicardial from Body Surface Maps by Using the Finite Element Method. *Japanese Circulation Journal*, 45(11):1312–1322, 1981.

[41] Richard O. Martin and Theo C. Pilkington. Unconstrained Inverse Electrocardiography : Epicardial Potentials. *IEEE Transactions on Biomedical Engineering*, BME-19(4):276–285, 1972.

[42] King Td, Barr Rc, Herman-Giddens Gs, Boaz De, and Spach Ms. Isopotential body surface maps and their relationship to atrial potentials in the dog. *Circ Res*, 30(4):393–405, 1972.

[43] Y. Rudy and B.J. Messinger-Rapport. The inverse problem in electrocardiography: solutions in terms of epicardial potentials. *Critical reviews in biomedical engineering*, 16(3):215–268, 1988.

[44] B. Milan Horáček and John C. Clements. The inverse problem of electrocardiography: A solution in terms of single- end double-layer sources on the epicardial surface. *Mathematical Biosciences*, 144(2):119–154, 1997.

[45] R C Barr and M S Spach. Inverse calculation of QRS-T epicardial potentials from body surface potential distributions for normal and ectopic beats in the intact dog. *Circ. Res.*, 42(5):661–675, 1978.

[46] BM Horácek, CJ Penney, and John C. Clements. The Inverse Problem of Electrocardiography in Terms of Epicardial Potentials and their Gradients. In *Computers in Cardiology*, pages 197–200, 1999.

[47] Fred Greensite and Geertjan Huiskamp. An improved method for estimating epicardial potentials from the body surface. *IEEE Transactions on Biomedical Engineering*, 45(1):98–104, 1998.

[48] Bernd Messnarz, Bernhard Tilg, Robert Modre, Gerald Fischer, and Friedrich Hanser. A New Spatiotemporal Regularization Approach for Reconstruction

of Cardiac Transmembrane Potential Patterns. *IEEE Transactions on Biomedical Engineering*, 51(2):273–281, 2004.

[49] Bin He, Guanglin Li, and Xin Zhang. Noninvasive imaging of cardiac transmembrane potentials within three-dimensional myocardium by means of a realistic geometry anisotropic heart model. *IEEE Transactions on Biomedical Engineering*, 50(10):1190–1202, 2003.

[50] D Potyagaylo, W H W Schulze, and O Dössel. A new method for choosing the regularization parameter in the transmembrane potential based inverse problem of ECG. *Computing in Cardiology*, pages 29–32, 2012.

[51] G Huiskamp and A van Oosterom. The depolarization sequence of the human heart surface computed from measured body surface potentials. *IEEE Transactions on Biomedical Engineering*, 35(12):1047–1058, dec 1988.

[52] Geertjan Huiskamp and Fred Greensite. A new method for myocardial activation imaging. *IEEE Transactions on Biomedical Engineering*, 44(6):433–446, 1997.

[53] A. J. Pullan, L. K. Cheng, M. P. Nash, C. P. Bradley, and D. J. Paterson. Noninvasive electrical imaging of the heart: Theory and model development. *Annals of Biomedical Engineering*, 29(10):817–836, 2001.

[54] Jan J M Cuppen and Adriaan Van Oosterom. Model Studies with the Inversely Calculated Isochrones of Ventricular Depolarization. *IEEE Transactions on Biomedical Engineering*, BME-31(10):652–659, 1984.

[55] Per Christian Hansen. *Rank-Deficient and Discrete III-Posed Problems.: Numerical Aspects of Linear Inversion*, volume 4. 1997.

[56] A N Tikhonov and V I A Arsenin. Solutions of Ill-Posed Problems. *Halsted*, 1977.

[57] Dana H. Brooks and G. F. Ahmad. Inverse electrocardiography by simultaneous imposition of multiple constraints. *IEEE Transactions on Biomedical Engineering*, 46(1):3–18, 1999.

[58] Piero Colli Franzone, B Taccardi, and C Viganotti. An approach to inverse calculation of epicardial potentials from body surface maps. *Advances in cardiology*, 21:50–54, 1978.

[59] Subham Ghosh and Yoram Rudy. Application of L1-norm regularization to epicardial potential solution of the inverse electrocardiography problem. *Annals of Biomedical Engineering*, 37(5):902–912, 2009.

[60] Linwei Wang, Omar A. Gharbia, B. Milan Horáček, and John L. Sapp. Noninvasive epicardial and endocardial electrocardiographic imaging of scar-related ventricular tachycardia. *Journal of Electrocardiology*, 49(6):887–893, 2016.

[61] Karthikeyan Umapathy, Krishnakumar Nair, Stephane Masse, Sridhar Krishnan, Jack Rogers, Martyn P. Nash, and Kumaraswamy Nanthakumar. Phase mapping of cardiac fibrillation. *Circulation: Arrhythmia and Electrophysiology*, 3(1):105–114, 2010.

[62] Martin Hanke. *Conjugate Gradient Type Methods for Ill-Posed Problems*. 1995.

[63] Jingjia Xu, Azar Rahimi Dehaghani, Fei Gao, and Linwei Wang. A Novel Total Variation Based Noninvasive Transmural Electrophysiological Imaging. *Miccai*, pages 501–508, 2013.

[64] Jingjia Xu, Azar Rahimi Dehaghani, Fei Gao, and Linwei Wang. Noninvasive transmural electrophysiological imaging based on minimization of total-variation functional. *IEEE Transactions on Medical Imaging*, 33(9):1860–1874, 2014.

[65] Paul Rodríguez and Brendt Wohlberg. Efficient minimization method for a generalized total variation functional. *IEEE Transactions on Image Processing*, 18(2):322–332, 2009.

[66] Azar Rahimi, Jingjia Xu, and Linwei Wang. Lp-Norm Regularization in Volumetric Imaging of Cardiac Current Sources. *Computational and Mathematical Methods in Medicine*, 2013:1–10, 2013.

[67] Jaume Coll-Font, Brittany Purcell, Jingjia Xu, Petr Stovicek, Dana H. Brooks, and Linwei Wang. Evaluation of 2-norm versus sparsity regularization in

spline-based joint reconstruction of epicardial and endocardial potentials from body-surface measurements. *Computing in Cardiology*, 42(2):957–960, 2015.

[68] Burak Erem, Jaume Coll-Font, Ramon Martinez Orellana, Petr St'Ovicek, and Dana H. Brooks. Using transmural regularization and dynamic modeling for noninvasive cardiac potential imaging of endocardial pacing with imprecise thoracic geometry. *IEEE Transactions on Medical Imaging*, 33(3):726–738, 2014.

[69] F Greensite. A new treatment of the inverse problem of multivariate analysis. *Inverse Problems*, 18:363–379, 2002.

[70] Fred Greensite. The temporal prior in bioelectromagnetic source imaging problems. *IEEE Transactions on Biomedical Engineering*, 50(10):1152–1159, 2003.

[71] Murat Onal and Yesim Serinagaoglu. Spatio-Temporal Solutions in Inverse Electrocardiography. In Jos Vander Sloten, Pascal Verdonck, Marc Nyssen, and Jens Haueisen, editors, *4th European Conference of the International Federation for Medical and Biological Engineering*, pages 180–183, Berlin, Heidelberg, 2009. Springer Berlin Heidelberg.

[72] D. Joly, Y. Goussard, and P. Savard. Time-recursive solution to the inverse problem of electrocardiography: a model-based approach. *Proceedings of the 15th Annual International Conference of the IEEE Engineering in Medicine and Biology Society*, pages 1–10, 1993.

[73] J. El-Jakl, F. Champagnat, and Y. Goussard. Time-space regularization of the inverse problem of electrocardiography. *Proceedings of 17th International Conference of the Engineering in Medicine and Biology Society*, 1:213–214, 1995.

[74] Linwei Wang, Ken C.L. Wong, Pengcheng Shi, Heye Zhang, and Huafeng Liu. Physiological-Model-Constrained Noninvasive Reconstruction of Volumetric Myocardial Transmembrane Potentials. *IEEE Transactions on Biomedical Engineering*, 57(2):296–315, 2010.

[75] Linwei Wang, Ken C L Wong, Heye Zhang, Huafeng Liu, and Pengcheng Shi. Noninvasive computational imaging of cardiac electrophysiology for 3-D infarct. *IEEE Transactions on Biomedical Engineering*, 58(4):1033–1043, 2011.

[76] J E Burnes, B Taccardi, R S MacLeod, and Y Rudy. Noninvasive ECG imaging of electrophysiologically abnormal substrates in infarcted hearts : A model study. *Circulation*, 101(5):533–540, 2000.

[77] F D Dawoud. Using inverse electrocardiography to image myocardial infarction. In *2007 Computers in Cardiology*, pages 177–180, sep 2007.

[78] W. Schulze, D. Farina, Y. Jiang, and O. Dössel. A Kalman filter with integrated Tikhonov-regularization to solve the inverse problem of electrocardiography. *IFMBE Proceedings*, 25(2):821–824, 2009.

[79] Umit Aydin and Yesim Serinagaoglu. Use of Activation Time Based Kalman Filtering in Inverse Problem of Electrocardiography. In Jos Vander Sloten, Pascal Verdonck, Marc Nyssen, and Jens Haueisen, editors, *4th European Conference of the International Federation for Medical and Biological Engineering*, pages 1200–1203, Berlin, Heidelberg, 2009. Springer Berlin Heidelberg.

[80] Y Serinagaoglu and U Aydin. Imaging the electrical activity of the heart using a Kalman filter based approach: Comparison of results using different STM's. In *2009 IEEE International Symposium on Biomedical Imaging: From Nano to Macro*, pages 153–156, jun 2009.

[81] U Aydin and Y Serinagaoglu. Comparison of Kalman filter and Bayesian-MAP approaches in the spatio-temporal solution of the inverse electrocardiography. In *2010 15th National Biomedical Engineering Meeting*, pages 1–4, apr 2010.

[82] Umit Aydin and Yesim Serinagaoglu Dogrusoz. A Kalman filter-based approach to reduce the effects of geometric errors and the measurement noise in the inverse ECG problem. *Medical and Biological Engineering and Computing*, 49(9):1003–1013, 2011.

[83] Jari Kaipio and Somersalo Erkki. *Statistical and Computational Inverse Problems*, volume 160. Springer, 2004.

[84] Alireza Ghodrati, Dana H. Brooks, Gilead Tadmor, and Robert S. MacLeod. Wavefront-based models for inverse electrocardiography. *IEEE Transactions on Biomedical Engineering*, 53(9):1821–1831, 2006.

[85] C Liu and B He. Noninvasive estimation of global activation sequence using the extended Kalman filter. *IEEE Trans. Biomed. Eng*, 58(3):541–549, 2011.

[86] Yesim Serinagaoglu Dogrusoz and Alireza Mazloumi Gavgani. Genetic algorithm-based regularization parameter estimation for the inverse electrocardiography problem using multiple constraints. *Medical and Biological Engineering and Computing*, 51(4):367–375, 2013.

[87] G F Ahmad, D H Brooks, and R S MacLeod. An admissible solution approach to inverse electrocardiography. *Annals of biomedical engineering*, 26(2):278–292, 1998.

[88] Yeşim Serinagaoglu, Dana H. Brooks, and Robert S. MacLeod. Improved performance of Bayesian solutions for inverse electrocardiography using multiple information sources. *IEEE Transactions on Biomedical Engineering*, 53(10):2024–2034, 2006.

[89] David M Schmidt, John S George, and C C Wood. Bayesian Inference Applied to the Electromagnetic Inverse Problem. *Human Brain Mapping*, 212:195–212, 1999.

[90] Gerald S Russell, Ramesh Srinivasan, and Don M Tucker. Bayesian estimates of error bounds for EEG source imaging. *IEEE transactions on medical imaging*, 17(6):1084–9, 1998.

[91] R O Martin, T C Pilkington, and M N Morrow. Statistically Constrained Inverse Electrocardiography. *IEEE Transactions on Biomedical Engineering*, BME-22(6):487–492, nov 1975.

[92] Manus Foster. An Application of the Wiener-Kolmogorov Smoothing Theory to Matrix Inversion. *Journal of the Society for Industrial and Applied Mathematics*, 9(3):387–392, 1961.

[93] T. C. Pilkington, R. C. Barr, and C. L. Rogers. Effect of conductivity interfaces in electrocardiography. *The Bulletin of Mathematical Biophysics*, 30(4):637–643, 1968.

[94] O. N. Strand and E. Rd Westwater. Minimum-RMS Estimation of the Numerical Solution of a Fredholm Integral Equation of the First Kind. *SIAM Journal on Numerical Analysis*, 5(2):287–295, 1968.

[95] Adriaan Van Oosterom. The use of the spatial covariance in computing pericardial potentials. *IEEE Transactions on Biomedical Engineering*, 46(7):778–787, 1999.

[96] Anders M. Dale and Martin I. Sereno. Improved Localization of Cortical Activity by Combining EEG and MEG with MRI Cortical Surface Reconstruction: A Linear Approach, 1993.

[97] Yeşim Serinagaoglu, Dana H. Brooks, and Robert S. MacLeod. Bayesian solutions and performance analysis in bioelectric inverse problems. *IEEE Transactions on Biomedical Engineering*, 52(6):1009–1020, 2005.

[98] Steven M. Kay. *Fundamentals of Statistical Signal Processing: Estimation Theory*, volume I. Prentice Hall, 1993.

[99] Charulatha Ramanathan and Yoram Rudy. Electrocardiographic imaging: II. Effect of torso inhomogeneities on noninvasive reconstruction of epicardial potentials, electrograms, and isochrones. *Journal of Cardiovascular Electrophysiology*, 12(2):241–252, 2001.

[100] Azar Rahimi and Linwei Wang. Sensitivity of noninvasive cardiac electrophysiological imaging to variations in personalized anatomical modeling. *IEEE Transactions on Biomedical Engineering*, 62(6):1563–1575, 2015.

[101] Tobias Heimann and Hans Peter Meinzer. Statistical shape models for 3D medical image segmentation: A review. *Medical Image Analysis*, 13(4):543–563, 2009.

[102] Brett M Burton, Burak Erem, Kristin Potter, Paul Rosen, Chris R. Johnson, Dana H. Brooks, and Rob S. MacLeod. Uncertainty visualization in forward and inverse cardiac models. *Computational Cardiology*, 36(3):490–499, 2010.

[103] Burak Erem, Peter M. Van Dam, and Dana H. Brooks. Identifying model inaccuracies and solution uncertainties in noninvasive activation-based imaging of cardiac excitation using convex relaxation. *IEEE Transactions on Medical Imaging*, 33(4):902–912, 2014.

[104] Nejib Zemzemi, Cecile Dobrzynski, Laura Bear, Mark Potse, Corentin Dallet, Yves Coudière, Remi Dubois, and Josselin Duchateau. Effect of the torso conductivity heterogeneities on the ECGI inverse problem solution. *Computing in Cardiology*, 42:233–236, 2015.

[105] A van Oosterom. ECGSIM: an interactive tool for studying the genesis of QRST waveforms. *Heart*, 90(2):165–168, 2004.

[106] J. Coil-Font, B. Erem, P. Stovicek, and D H Brooks. A Statistical Approach To Incorporate Multiple ECG or EEG Recordings With Artifactual Variability Into Inverse Solutions. In *International Symposium on Biomedical Imaging*, pages 1053–1056, 2015.

[107] Jaume Coll-Font, Burak Erem, Petr Stovicek, and Dana H. Brooks. Using a new Time-Independent Average Method for Non-Invasive Cardiac Potential Imaging of Endocardial Pacing with Imprecise Thorax Geometry. *Computing in Cardiology Conference (CinC)*, pages 825–828, 2014.

[108] Corentin Dallet, Josselin Duchateau, Mélèze Hocini, Laura Bear, Marianna Meo, Frédéric Sacher, Michel Haïssaguerre, and Rémi Dubois. Combined Signal Averaging and Electrocardiographic Imaging Method to Non-Invasively Identify Atrial and Ventricular Tachycardia Mechanisms. *Computing in Cardiology*, 43(Cc):1–4, 2016.

[109] Azar Rahimi, Jingjia Xu, and Linwei Wang. Hierarchical Multiple-Model Bayesian Approach to Transmural Electrophysiological Imaging. *Medical Image Computing and Computer-Assisted Intervention – MICCAI 2014*, 8674:538–545, 2014.

[110] Azar Rahimi, John Sapp, Jingjia Xu, Peter Bajorski, Milan Horacek, and Linwei Wang. Examining the impact of prior models in transmural electrophys-

iological imaging: A hierarchical multiple-model Bayesian approach. *IEEE Transactions on Medical Imaging*, 35(1):229–243, 2016.

[111] Radford M. Neal. Slice Sampling. *Annals of Statistics*, 31(3):758–767, 2003.

[112] Jingjia Xu, John L Sapp, Azar Rahimi Dehaghani, Fei Gao, and Linwei Wang. *Variational Bayesian Electrophysiological Imaging of Myocardial Infarction*, pages 529–537. Springer International Publishing, Cham, 2014.

[113] Nejib Zemzemi, Simon Labarthe, Rémi Dubois, and Yves Coudiere. From body surface potential to activation maps on the atria: A machine learning technique. *Computing in Cardiology (CinC), 2012*, pages 125–128, 2012.

[114] Nejib Zemzemi and Remi Dubois. A machine learning regularization of the inverse problem in electrocardiography imaging. *Computing in Cardiology Conference (CinC)*, pages 1135–1138, 2013.

[115] H. S. Oster, B. Taccardi, R. L. Lux, P. R. Ershler, and Y. Rudy. Electrocardiographic imaging: Noninvasive characterization of intramural myocardial activation from inverse-reconstructed epicardial potentials and electrograms. *Circulation*, 97(15):1496–1507, 1998.

[116] Howard S. Oster and Yoram Rudy. The Use of Temporal Information in the Regularization of the Inverse Problem of Electrocardiography. *IEEE Transactions on Biomedical Engineering*, 39(1):65–75, 1992.

[117] Peter R. Johnston and Ramesh M. Gulrajani. Selecting the corner in the L-curve approach to Tikhonov regularization. *IEEE Transactions on Biomedical Engineering*, 47(9):1293–1296, 2000.

[118] Per Christian Hansen. Analysis of Discrete Ill-Posed Problems by Means of the L-Curve. *SIAM Review*, 34(4):561–580, 1992.

[119] Cesare Corrado, Jean Frédéric Gerbeau, and Philippe Moireau. Identification of weakly coupled multiphysics problems. Application to the inverse problem of electrocardiography. *Journal of Computational Physics*, 283:271–298, 2015.

[120] Linwei Wang. Computational reduction for noninvasive transmural electro-physiological imaging. *Computers in Biology and Medicine*, 43(3):184–199, 2013.

[121] Dan Simon. *Optimal State Estimation: Kalman, HInfinity, and Nonlinear Approaches*. 2006.

[122] H. E. Rauch, C. T. Striebel, and F. Tung. Maximum likelihood estimates of linear dynamic systems. *AIAA Journal*, 3(8):1445–1450, 1965.

[123] Byron M Yu and Krishna V Shenoy. Derivation of Kalman Filtering and Smoothing Equations Forward Recursions : Filtering. (1):1–5, 2004.

[124] A. Katsamanis, G. Ananthakrishnan, G. Papandreou, P. Maragos, and O. Engwall. Audiovisual speech inversion by switching dynamical modeling governed by a Hidden Markov process. *European Signal Processing Conference*, pages 2–6, 2008.

[125] Leo J Lee, Paul Fieguth, and Li Deng. A functional articulatory dynamic model for speech production. *Proceedings of ICASSP*, pages 797–800, 2001.

[126] Sorin Dusan and Li Deng. Acoustic-to-articulatory inversion using dynamical and phonological constraints. *5'th Seminar on Speech Production: Models and Data*, pages 237–240, 2000.

[127] I. Yücel Özbek and Mübeccel Demirekler. ML vs. MAP parameter estimation of linear dynamic systems for acoustic-to-articulatory inversion: A comparative study. *European Signal Processing Conference*, pages 805–809, 2010.

[128] Zoubin Ghahramani and Geoffrey E. Hinton. Parameter Estimation for Linear Dynamical Systems. *Technical Report*, 6(CRG-TR-96-2):1–6, 1996.

[129] Stephen Boyd and Lieven Vandenberghe. *Convex Optimization*, volume 25. Cambridge University Press, 2010.

[130] Peter D. Hoff. *A First Course in Bayesian Statistical Methods*. Springer, 2009.

[131] R. S. MacLeod, R. L. Lux, and B. Taccardi. A possible mechanism for electrocardiographically silent changes in cardiac repolarization. *Journal of Electrocardiology*, 30(SUPPL.):114–121, 1998.

[132] Yoram Rudy. Noninvasive electrocardiographic imaging of arrhythmogenic substrates in humans. *Circulation Research*, 112(5):863–874, 2013.

[133] R.S. MacLeod and C.R. Johnson. Map3d: interactive scientific visualization for bioengineering data. *Proceedings of the 15th Annual International Conference of the IEEE Engineering in Medicine and Biology Societ*, pages 30–31, 1993.

[134] L I Horwitz. Current clinical utility of body surface mapping. *The Journal of invasive cardiology*, 7(9):265–274, 1995.

[135] Matthijs J.M. Cluitmans, Pietro Bonizzi, Joël M.H. Karel, Marco Das, Bas L.J.H. Kietselaer, Monique M.J. de Jong, Frits W. Prinzen, Ralf L.M. Peeters, Ronald L. Westra, and Paul G.A. Volders. In Vivo Validation of Electrocardiographic Imaging. *JACC: Clinical Electrophysiology*, 3(3):232–242, 2017.

[136] Burak Erem, Dana H. Brooks, Peter M. Van Dam, Jeroen G. Stinstra, and Rob S. MacLeod. Spatiotemporal estimation of activation times of fractionated ECGs on complex heart surfaces. *Proceedings of the Annual International Conference of the IEEE Engineering in Medicine and Biology Society, EMBS*, pages 5884–5887, 2011.

[137] Ramesh M. Gulrajani. The forward and inverse problems of electrocardiography. *IEEE Engineering in Medicine and Biology*, 17(5):84–122, 1998.

[138] Christopher M Bishop. *Pattern Recognition and Machine Learning (Information Science and Statistics)*. Springer-Verlag, Berlin, Heidelberg, 2006.

[139] Suwanchai Sangsuk-Iam and Thomas E. Bullock. Analysis of discrete-time Kalman filtering under incorrect noise covariances. *IEEE Transactions on Automatic Control*, 35(12):1304 – 1309, 1990.

[140] Andrew H Jazwinski. Stochastic Processes and Filtering Theory. volume 64, pages 47–92. Elsevier, 1970.

[141] N. A. Thacker and A. J. Lacey. Tutorial : The Kalman Filter, 1996.

[142] Nick T Koussoulas and Cornelius T Leondes. On the sensitivity of a discrete-time Kalman filter to plant-dynamics modelling errors. *International Journal of Systems Science*, 17(6):937–941, 1986.

[143] H. W. Turnbull. A Matrix Form of Taylor's Theorem. *Proceedings of the Edinburgh Mathematical Society*, 2(01):33, jan 1930.

[144] Kaare Breandt Petersen and Michael Syskind Pedersen. The Matrix Cookbook. *Citeseer*, 16(4):1–66, 2007.

[145] Marianna Bolla. Maximum likelihood estimation of the parameters of the multivariate normal distribution and the distribution of these estimators (the Wishart distribution).

[146] Daniel B. Rowe. *Multivariable Bayesian statistics: models for source separation and signal mixing*. Chapman & Hall/CRC, 2003.

APPENDIX A

MAXIMUM LIKELIHOOD PARAMETER ESTIMATION DERIVATION

Estimation of $\bar{x}$:

$$\frac{\partial}{\partial \bar{x}} \sum_{\ell=1}^{L} ln \, p(x_1^\ell | \bar{x}, \Sigma)$$

$$= \frac{\partial}{\partial \bar{x}} \sum_{\ell=1}^{L} ln \left[\frac{1}{(2\pi)^{M/2} |\Sigma|^{1/2}} \cdot exp\left(-\frac{1}{2}(x_1^\ell - \bar{x})^T \Sigma^{-1} (x_1^\ell - \bar{x}) \right) \right]$$

$$= \frac{\partial}{\partial \bar{x}} \sum_{\ell=1}^{L} -\frac{M}{2} ln \, 2\pi - \frac{1}{2} ln \, |\Sigma| - \frac{1}{2}(x_1^\ell - \bar{x})^T \Sigma^{-1} (x_1^\ell - \bar{x})$$

$$= \sum_{\ell=1}^{L} \underbrace{\frac{\partial}{\partial \bar{x}}\left(-\frac{M}{2} ln \, 2\pi \right)}_{0} + \underbrace{\frac{\partial}{\partial \bar{x}}\left(-\frac{1}{2} ln \, |\Sigma| \right)}_{0} + \frac{\partial}{\partial \bar{x}}\left(-\frac{1}{2}(x_1^\ell - \bar{x})^T \Sigma^{-1} (x_1^\ell - \bar{x}) \right)$$

$$\tag{A.1}$$

Petersen and Pedersen [144] (see equation (86) in their work) stated that when W is a symmetric matrix, we have the following property:

$$\frac{\partial}{\partial s}(x - s)^T W (x - s) = -2W(x - s) \tag{A.2}$$

Since the covariance matrix Σ is symmetric, by using Petersen and Pedersen's statement, we have:

$$\frac{\partial}{\partial \bar{x}} \sum_{\ell=1}^{L} ln \, p(x_1^\ell | \bar{x}, \Sigma) = \sum_{\ell=1}^{L} \frac{\partial}{\partial \bar{x}}\left(-\frac{1}{2}(x_1^\ell - \bar{x})^T \Sigma^{-1} (x_1^\ell - \bar{x}) \right)$$

$$= \sum_{\ell=1}^{L} -\frac{1}{2} \cdot \left(-2\Sigma^{-1}(x_1^\ell - \bar{x}) \right)$$

$$= \sum_{\ell=1}^{L} \Sigma^{-1}(x_1^\ell - \bar{x}) = 0 \tag{A.3}$$

$$\hat{\bar{x}} = \frac{1}{L} \sum_{\ell=1}^{L} x_1^\ell \tag{A.4}$$

Estimation of Σ:

Taking the derivative with respect to Σ is equivalent to taking the derivative with respect to Σ^{-1} [145]. Therefore, we proceed with using Σ^{-1} as the derivative argument.

$$\frac{\partial}{\partial \Sigma^{-1}} \sum_{\ell=1}^{L} ln \; p(x_1^\ell | \bar{x}, \Sigma)$$

$$= \frac{\partial}{\partial \Sigma^{-1}} \sum_{\ell=1}^{L} ln \left[\frac{1}{(2\pi)^{M/2} |\Sigma|^{1/2}} \cdot exp\left(-\frac{1}{2} (x_1^\ell - \bar{x})^T \Sigma^{-1} (x_1^\ell - \bar{x}) \right) \right]$$

$$= \frac{\partial}{\partial \Sigma^{-1}} \sum_{\ell=1}^{L} -\frac{M}{2} ln \; 2\pi - \frac{1}{2} ln \; |\Sigma| - \frac{1}{2} (x_1^\ell - \bar{x})^T \Sigma^{-1} (x_1^\ell - \bar{x})$$

$$= \sum_{\ell=1}^{L} \underbrace{\frac{\partial}{\partial \Sigma^{-1}} \left(-\frac{M}{2} ln \; 2\pi \right)}_{0} + \frac{\partial}{\partial \Sigma^{-1}} \left(\frac{1}{2} ln \; |\Sigma^{-1}| \right)$$

$$+ \frac{\partial}{\partial \Sigma^{-1}} \left(-\frac{1}{2} \underbrace{(x_1^\ell - \bar{x})^T \Sigma^{-1} (x_1^\ell - \bar{x})}_{tr\left(\Sigma^{-1} (x_1^\ell - \bar{x})(x_1^\ell - \bar{x})^T \right)} \right) \tag{A.5}$$

According to Petersen and Pedersen's [144] work (see equation (100) in their work) we have the following property:

$$\frac{\partial}{\partial X} tr(XA) = A^T \tag{A.6}$$

Using this property and keeping in the mind that Σ is symmetric:

$$\frac{\partial}{\partial \Sigma^{-1}} \sum_{\ell=1}^{L} ln \; p(x_1^\ell | \bar{x}, \Sigma) = \sum_{\ell=1}^{L} \frac{1}{2} \frac{\partial}{\partial \Sigma^{-1}} ln \; |\Sigma^{-1}| - \frac{1}{2} \frac{\partial}{\partial \Sigma^{-1}} tr\left((x_1^\ell - \bar{x})^T \Sigma^{-1} (x_1^\ell - \bar{x}) \right)$$

$$= \sum_{\ell=1}^{L} \left(\frac{1}{2} \Sigma - \frac{1}{2} (x_1^\ell - \bar{x})(x_1^\ell - \bar{x})^T \right) = 0 \tag{A.7}$$

Finally, we have:

$$L \cdot \Sigma = \sum_{\ell=1}^{L} (x_1^\ell - \bar{x})(x_1^\ell - \bar{x})^T \tag{A.8}$$

$$\hat{\Sigma} = \frac{1}{L} \sum_{\ell=1}^{L} (x_1^\ell - \bar{x})(x_1^\ell - \bar{x})^T \tag{A.9}$$

Estimation of R:

$$\frac{\partial}{\partial R^{-1}} \sum_{\ell=1}^{L} \sum_{k=1}^{T} ln\ p(y_k^\ell | x_k^\ell, R) = \frac{\partial}{\partial R^{-1}} \sum_{\ell=1}^{L} \sum_{k=1}^{T}$$

$$ln\left[\frac{1}{(2\pi)^{D/2} |R|^{1/2}} \cdot exp\left(-\frac{1}{2}(y_k^\ell - Hx_k^\ell)^T R^{-1}(y_k^\ell - Hx_k^\ell) \right) \right]$$

$$= \frac{\partial}{\partial R^{-1}} \sum_{\ell=1}^{L} \sum_{k=1}^{T} -\frac{D}{2}\ ln\ 2\pi - \frac{1}{2}\ ln\ |R| - \frac{1}{2}(y_k^\ell - Hx_k^\ell)^T R^{-1}(y_k^\ell - Hx_k^\ell)$$

$$= \sum_{\ell=1}^{L} \sum_{k=1}^{T} \underbrace{\frac{\partial}{\partial R^{-1}}\left(-\frac{D}{2}\ ln\ 2\pi \right)}_{0} + \frac{\partial}{\partial R^{-1}}\left(-\frac{1}{2}\ ln\ |R| \right)$$

$$+ \frac{\partial}{\partial R^{-1}}\left(-\frac{1}{2}(y_k^\ell - Hx_k^\ell)^T R^{-1}(y_k^\ell - Hx_k^\ell) \right) \quad \text{(A.10)}$$

By using the same approach we used while finding $\hat{\Sigma}$, we simplify equation (A.10) as follows:

$$\frac{\partial}{\partial R^{-1}} \sum_{\ell=1}^{L} \sum_{k=1}^{T} ln\ p(y_k^\ell | x_k^\ell, R) = \left(\sum_{\ell=1}^{L} \sum_{k=1}^{T} \frac{1}{2}R - \frac{1}{2}(y_k^\ell - Hx_k^\ell)(y_k^\ell - Hx_k^\ell)^T \right)$$

$$= 0 \quad \text{(A.11)}$$

$$\underbrace{\sum_{\ell=1}^{L} \sum_{k=1}^{T} R}_{LTR} = \sum_{\ell=1}^{L} \sum_{k=1}^{T} (y_k^\ell - Hx_k^\ell)(y_k^\ell - Hx_k^\ell)^T \quad \text{(A.12)}$$

$$\hat{R} = \frac{1}{LT} \sum_{\ell=1}^{L} \sum_{k=1}^{T} (y_k^\ell - Hx_k^\ell)(y_k^\ell - Hx_k^\ell)^T \quad \text{(A.13)}$$

Estimation of F:

$$\frac{\partial}{\partial F} \sum_{\ell=1}^{L} \sum_{k=2}^{T} \ln p(x_k^\ell | x_{k-1}^\ell, F, Q) = \frac{\partial}{\partial F} \sum_{\ell=1}^{L} \sum_{k=2}^{T}$$

$$\ln \left[\frac{1}{(2\pi)^{M/2} |Q|^{1/2}} \cdot exp\left(-\frac{1}{2}(x_k^\ell - Fx_{k-1}^\ell)^T Q^{-1}(x_k^\ell - Fx_{k-1}^\ell) \right) \right]$$

$$= \frac{\partial}{\partial F} \sum_{\ell=1}^{L} \sum_{k=2}^{T} -\frac{M}{2} \ln 2\pi - \frac{1}{2} \ln |Q| - \frac{1}{2}(x_k^\ell - Fx_{k-1}^\ell)^T Q^{-1}(x_k^\ell - Fx_{k-1}^\ell)$$

$$= \sum_{\ell=1}^{L} \sum_{k=2}^{T} \underbrace{\frac{\partial}{\partial F}\left(-\frac{M}{2} \ln 2\pi \right)}_{0} + \underbrace{\frac{\partial}{\partial F}\left(-\frac{1}{2} \ln |Q| \right)}_{0}$$

$$+ \frac{\partial}{\partial F}\left(-\frac{1}{2}(x_k^\ell - Fx_{k-1}^\ell)^T Q^{-1}(x_k^\ell - Fx_{k-1}^\ell) \right)$$

$$\text{(A.14)}$$

Again, utilizing Petersen and Pedersen's [144] work (see property number 88):

$$\frac{\partial}{\partial A}(x - As)^T W (x - As) = -2W(x - As)s^T \qquad \text{(A.15)}$$

We have:

$$\sum_{\ell=1}^{L} \sum_{k=2}^{T} -\frac{1}{2} \cdot -2Q^{-1}(x_k^\ell - Fx_{k-1}^\ell)(x_{k-1}^\ell)^T = 0 \qquad \text{(A.16)}$$

$$\sum_{\ell=1}^{L} \sum_{k=2}^{T} Q^{-1} x_k^\ell (x_{k-1}^\ell)^T = \sum_{\ell=1}^{L} \sum_{k=2}^{T} Q^{-1} Fx_{k-1}^\ell (x_{k-1}^\ell)^T \qquad \text{(A.17)}$$

Cancelling Q^{-1} terms out yields:

$$\hat{F} = \left[\sum_{\ell=1}^{L} \sum_{k=2}^{T} x_k^\ell (x_{k-1}^\ell)^T \right] \cdot \left[\sum_{\ell=1}^{L} \sum_{k=2}^{T} x_{k-1}^\ell (x_{k-1}^\ell)^T \right]^{-1} \qquad \text{(A.18)}$$

Estimation of Q:

$$\frac{\partial}{\partial Q^{-1}} \sum_{\ell=1}^{L} \sum_{k=2}^{T} \ln p(x_k^\ell | x_{k-1}^\ell, F, Q) = \frac{\partial}{\partial Q^{-1}} \sum_{\ell=1}^{L} \sum_{k=2}^{T}$$

$$\ln \left[\frac{1}{(2\pi)^{M/2} |Q|^{1/2}} \cdot exp\left(-\frac{1}{2}(x_k^\ell - Fx_{k-1}^\ell)^T Q^{-1}(x_k^\ell - Fx_{k-1}^\ell) \right) \right]$$

$$= \frac{\partial}{\partial Q^{-1}} \sum_{\ell=1}^{L} \sum_{k=2}^{T} -\frac{M}{2} \ln 2\pi - \frac{1}{2} \ln |Q| - \frac{1}{2}(x_k^\ell - Fx_{k-1}^\ell)^T Q^{-1}(x_k^\ell - Fx_{k-1}^\ell)$$

$$= \sum_{\ell=1}^{L} \sum_{k=2}^{T} \underbrace{\frac{\partial}{\partial Q^{-1}}\left(-\frac{M}{2} \ln 2\pi \right)}_{0} + \frac{\partial}{\partial Q^{-1}}\left(-\frac{1}{2} \ln |Q| \right)$$

$$+ \frac{\partial}{\partial Q^{-1}}\left(-\frac{1}{2}(x_k^\ell - Fx_{k-1}^\ell)^T Q^{-1}(x_k^\ell - Fx_{k-1}^\ell) \right)$$

$$\tag{A.19}$$

Again, by utilizing the approach that is used for finding $\hat{\Sigma}$, equation (A.19) simplifies to the following equation:

$$\frac{\partial}{\partial Q^{-1}} \sum_{\ell=1}^{L} \sum_{k=2}^{T} \ln p(x_k^\ell | x_{k-1}^\ell, F, Q) = \left(\sum_{\ell=1}^{L} \sum_{k=2}^{T} \frac{1}{2}Q - \frac{1}{2}(x_k^\ell - Fx_{k-1}^\ell)(x_k^\ell - Fx_{k-1}^\ell)^T \right)$$

$$= 0 \tag{A.20}$$

$$\underbrace{\sum_{\ell=1}^{L} \sum_{k=2}^{T} Q}_{L(T\text{-}1)Q} = \sum_{\ell=1}^{L} \sum_{k=2}^{T}(x_k^\ell - Fx_{k-1}^\ell)(x_k^\ell - Fx_{k-1}^\ell)^T \tag{A.21}$$

$$\hat{Q} = \frac{1}{L(T-1)} \sum_{\ell=1}^{L} \sum_{k=2}^{T}(x_k^\ell - Fx_{k-1}^\ell)(x_k^\ell - Fx_{k-1}^\ell)^T \tag{A.22}$$

MAXIMUM A POSTERIORI PARAMETER ESTIMATION DERIVATION

Estimation of F:

$$\frac{\partial}{\partial F}\big(ln\ \Pi(\Theta) + ln\ p(F,Q)\big) = \frac{\partial}{\partial F}\big(ln\ \Pi(\Theta)\big) + \underbrace{\frac{\partial}{\partial F}\big(-\frac{M}{2}ln\ |\Phi|\big)}_{0}$$

$$+ \underbrace{\frac{\partial}{\partial F}\big(\frac{v+2M+1}{2}ln\ |Q^{-1}|\big)}_{0} + \frac{\partial}{\partial F}\big(-\frac{1}{2}tr\big[\Phi^{-1}F^T Q^{-1}F + Q^{-1}\Psi\big]\big) \quad \text{(B.1)}$$

We have already found $\frac{\partial}{\partial F}\big(ln\ \Pi(\Theta)\big)$ term in equation (A.16). To find the derivative of the last term in equation (B.1), we use the following property [146] (see section 6.2.1 in [146]):

$$\frac{\partial}{\partial \theta}tr\big[A(\theta - \theta_0)^T B(\theta - \theta_0)\big] = 2B(\theta - \theta_0)A \quad \text{(For symmetric A and B matrices)}$$
$$\text{(B.2)}$$

Using above-mentioned statements, we take the derivative and equate it to zero as follows provided that Φ and Q are symmetric matrices which we will show shortly:

$$\frac{\partial}{\partial F}\big(ln\ \Pi(\Theta) + ln\ p(F,Q)\big) = \sum_{\ell=1}^{L}\sum_{k=2}^{T} Q^{-1}x_k^\ell (x_{k-1}^\ell)^T - \sum_{\ell=1}^{L}\sum_{k=2}^{T} Q^{-1}F x_{k-1}^\ell (x_{k-1}^\ell)^T$$
$$- \frac{1}{2}2Q^{-1}F\Phi^{-1} \quad \text{(B.3)}$$

$$0 = \sum_{\ell=1}^{L}\sum_{k=2}^{T} Q^{-1}x_k^\ell (x_{k-1}^\ell)^T - \sum_{\ell=1}^{L}\sum_{k=2}^{T} Q^{-1}F x_{k-1}^\ell (x_{k-1}^\ell)^T - \frac{1}{2}2Q^{-1}F\Phi^{-1}$$

$$= Q^{-1}\sum_{\ell=1}^{L}\sum_{k=2}^{T} x_k^\ell (x_{k-1}^\ell)^T - Q^{-1}F\left[\sum_{\ell=1}^{L}\sum_{k=2}^{T}\big(x_{k-1}^\ell (x_{k-1}^\ell)^T\big) + \Phi^{-1}\right] \quad \text{(B.4)}$$

$$\hat{F} = \left[\sum_{\ell=1}^{L}\sum_{k=2}^{T} x_k^\ell (x_{k-1}^\ell)^T\right]\left[\sum_{\ell=1}^{L}\sum_{k=2}^{T}\big(x_{k-1}^\ell (x_{k-1}^\ell)^T\big) + \Phi^{-1}\right]^{-1} \quad \text{(B.5)}$$

Estimation of Q:

$$\frac{\partial}{\partial Q^{-1}}\big(ln\ \Pi(\Theta) + ln\ p(F, Q)\big) = \frac{\partial}{\partial Q^{-1}}\big(ln\ \Pi(\Theta)\big) + \underbrace{\frac{\partial}{\partial Q^{-1}}\big(-\frac{M}{2}ln\ |\Phi|\big)}_{0}$$

$$+ \frac{\partial}{\partial Q^{-1}}\big(\frac{v + 2M + 1}{2}ln\ |Q^{-1}|\big) + \frac{\partial}{\partial Q^{-1}}\big(-\frac{1}{2}tr\big[\Phi^{-1}F^T Q^{-1}F + Q^{-1}\Psi\big]\big) \quad \text{(B.6)}$$

We have already found $\frac{\partial}{\partial Q^{-1}}\big(ln\ \Pi(\Theta)\big)$ term in equation (A.20). To find the derivative of the last term in equation (B.6), we use the following properties [144]:

$$tr(AB) = tr(BA) \tag{B.7}$$

$$\frac{\partial}{\partial X}tr(XA) = A^T \tag{B.8}$$

$$tr\big(\underbrace{\Phi^{-1}F^T}_{A}\underbrace{Q^{-1}F}_{B} + Q^{-1}\Psi\big) = tr(Q^{-1}F\Phi^{-1}F^T) + tr(Q^{-1}\Psi) \tag{B.9}$$

$$\frac{\partial}{\partial Q^{-1}}\big[tr(Q^{-1}F\Phi^{-1}F^T) + tr(Q^{-1}\Psi)\big] = F^T\Phi^{-1}F + \Psi^T \tag{B.10}$$

In the light of the discussion above, we take the derivative and equate it to zero as follows:

$$\frac{\partial}{\partial Q^{-1}}\big(ln\ \Pi(\Theta) + ln\ p(F, Q)\big) = \sum_{\ell=1}^{L}\sum_{k=2}^{T}\Big[\frac{1}{2}Q - \frac{1}{2}(x_k^\ell - Fx_{k-1}^\ell)(x_k^\ell - Fx_{k-1}^\ell)^T\Big]$$

$$+ \frac{v + 2M + 1}{2}Q - \frac{1}{2}(F^T\Phi^{-1}F + \Psi^T) \tag{B.11}$$

$$0 = L(T-1)Q - \sum_{\ell=1}^{L}\sum_{k=2}^{T}(x_k^\ell - Fx_{k-1}^\ell)(x_k^\ell - Fx_{k-1}^\ell)^T$$

$$+ (v + 2M + 1)Q - (F^T\Phi^{-1}F + \Psi^T) \tag{B.12}$$

$$\hat{Q} = \frac{\sum_{\ell=1}^{L}\sum_{k=2}^{T}(x_k^\ell - Fx_{k-1}^\ell)(x_k^\ell - Fx_{k-1}^\ell)^T + \big(F^T\Phi^{-1}F + \Psi^T\big)}{L(T-1) + (v + 2M + 1)} \tag{B.13}$$

We now have found $\hat{F}$ and $\hat{Q}$ but there are unknowns in these formulas. These unknowns are degrees of freedom v, scale matrix Ψ and left covariance matrix Φ. Those three prior distribution parameters should be estimated.

In our work, we choose the inverse of left covariance matrix Φ and the scale matrix Ψ as follows:

$$\Phi^{-1} = \alpha \sum_{\ell=1}^{L} \sum_{k=2}^{T} x_{k-1}^{\ell} (x_{k-1}^{\ell})^T \tag{B.14}$$

$$\Psi = \frac{1}{v} I \tag{B.15}$$

where the parameter α is estimated by trial and error. In this work, we use $\alpha = 0.1$. Degrees of freedom v is the number of independent observations and in our case equals to:

$$v = L(T - 1) \tag{B.16}$$

APPENDIX C

BAYESIAN MAXIMUM A POSTERIORI ESTIMATION DERIVATION

$$\hat{x} = \underset{x}{\operatorname{argmax}}[\underbrace{ln\ p(y \mid x)}_{\text{Part 1}} + \underbrace{ln\ p(x)}_{\text{Part 2}}] \tag{C.1}$$

Taking the derivative of **Part 1** yields:

$$
\begin{aligned}
\frac{\partial}{\partial x} ln\ p(y|x) &= \frac{\partial}{\partial x} ln\left[\frac{1}{(2\pi)^{D/2}|R|^{1/2}} \cdot exp\left(-\frac{1}{2}(y - Hx)^T R^{-1}(y - Hx) \right) \right] \\
&= \frac{\partial}{\partial x}\left(\underbrace{-\frac{D}{2}\ ln\ 2\pi - \frac{1}{2}\ ln\ |R|}_{0} - \frac{1}{2}(y - Hx)^T R^{-1}(y - Hx) \right)
\end{aligned}
\tag{C.2}
$$

Using Petersen and Pedersen's [144] study (see equation (84) in their work), provided that R is symmetric, we find the result as:

$$\frac{\partial}{\partial s}(x - As)^T W(x - As) = -2A^T W(x - As) \tag{C.3}$$

$$
\begin{aligned}
\frac{\partial}{\partial x}\left(-\frac{1}{2}(y - Hx)^T R^{-1}(y - Hx) \right) &= -\frac{1}{2} \cdot -2H^T R^{-1}(y - Hx) \\
&= H^T R^{-1}(y - Hx) \tag{C.4}
\end{aligned}
$$

Taking the derivative of **Part 2** yields:

$$
\begin{aligned}
\frac{\partial}{\partial x} ln\ p(x) &= \frac{\partial}{\partial x} ln\left[\frac{1}{(2\pi)^{M/2}|\Sigma|^{1/2}} \cdot exp\left(-\frac{1}{2}(x - \bar{x})^T \Sigma^{-1}(x - \bar{x}) \right) \right] \\
&= \frac{\partial}{\partial x}\left(\underbrace{-\frac{M}{2}\ ln\ 2\pi - \frac{1}{2}\ ln\ |\Sigma|}_{0} - \frac{1}{2}(x - \bar{x})^T \Sigma^{-1}(x - \bar{x}) \right)
\end{aligned}
\tag{C.5}
$$

Again, using Petersen and Pedersen's [144] study (see equation (87) in their work), provided that Σ is symmetric, we find the result as:

$$\frac{\partial}{\partial x}(x - As)^T W(x - As) = 2W(x - As) \tag{C.6}$$

$$\frac{\partial}{\partial x}\left(-\frac{1}{2}(x - \bar{x})^T \Sigma^{-1}(x - \bar{x})\right) = -\frac{1}{2} \cdot 2\Sigma^{-1}(x - \bar{x})$$
$$= -\Sigma^{-1}(x - \bar{x}) \tag{C.7}$$

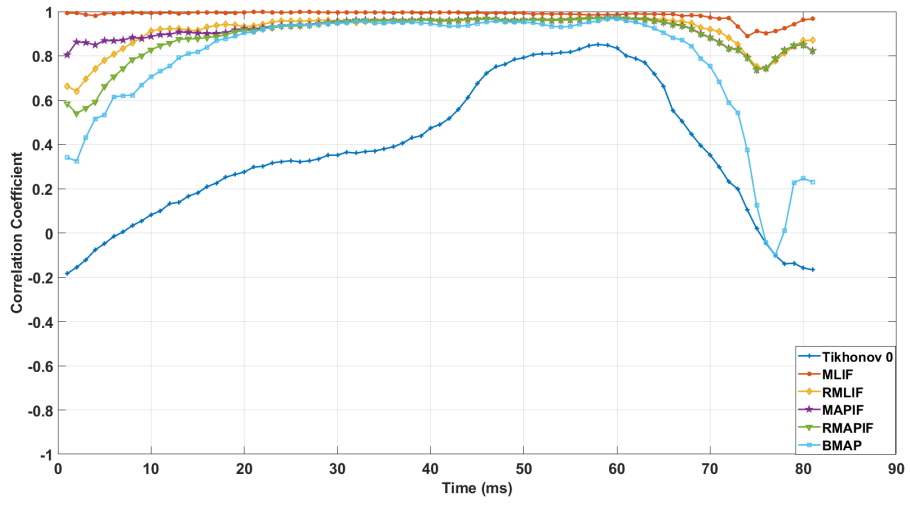Finally, we add **Part 1** and **Part 2** and set the result equal to zero to find $\hat{x}$:

$$H^T R^{-1}(y - Hx) - \Sigma^{-1}(x - \bar{x}) = 0 \tag{C.8}$$

$$H^T R^{-1}y + \Sigma^{-1}\bar{x} = \left(H^T R^{-1}H + \Sigma^{-1}\right)x \tag{C.9}$$

$$\hat{x} = \left(H^T R^{-1}H + \Sigma^{-1}\right)^{-1}\left(H^T R^{-1}y + \Sigma^{-1}\bar{x}\right) \tag{C.10}$$

APPENDIX D

CC AND RDMS PLOTS

(a) Correlation coefficient vs time plot for scenario 1 under 10 dB SNR
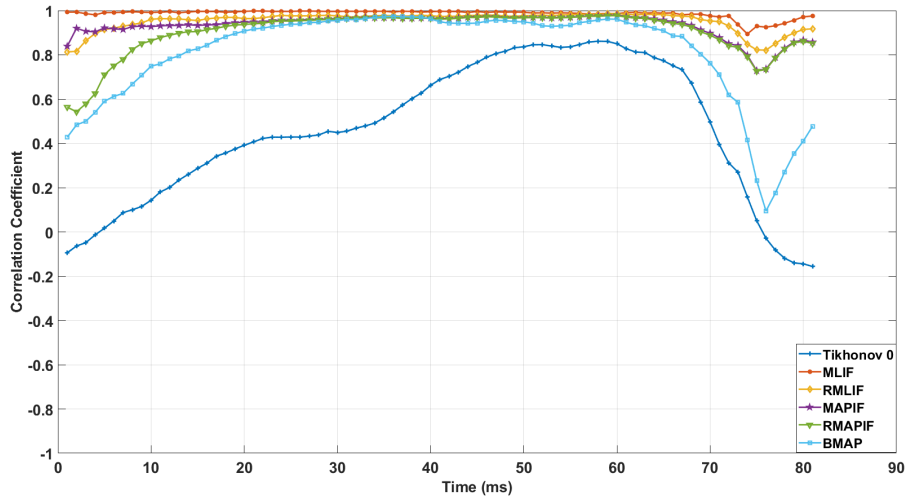
(b) Correlation coefficient vs time plot for scenario 1 under 15 dB SNR

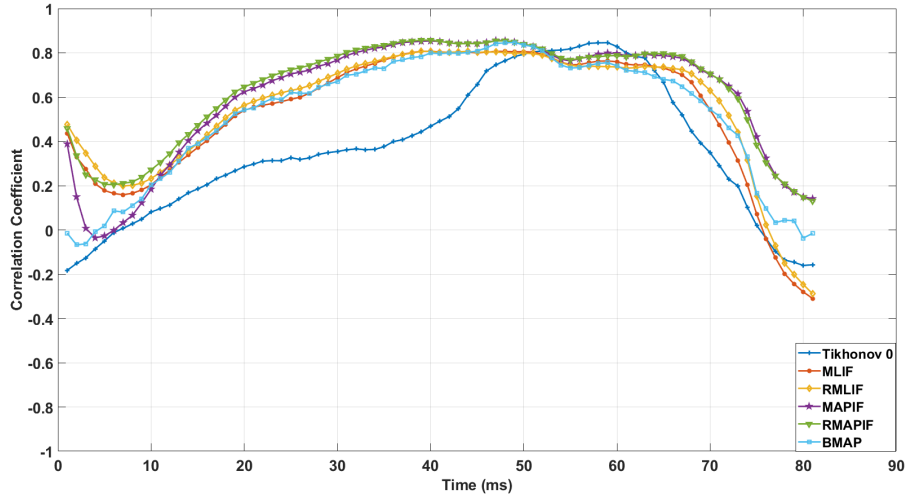Figure D.1: Correlation coefficient vs time plots for scenario 1
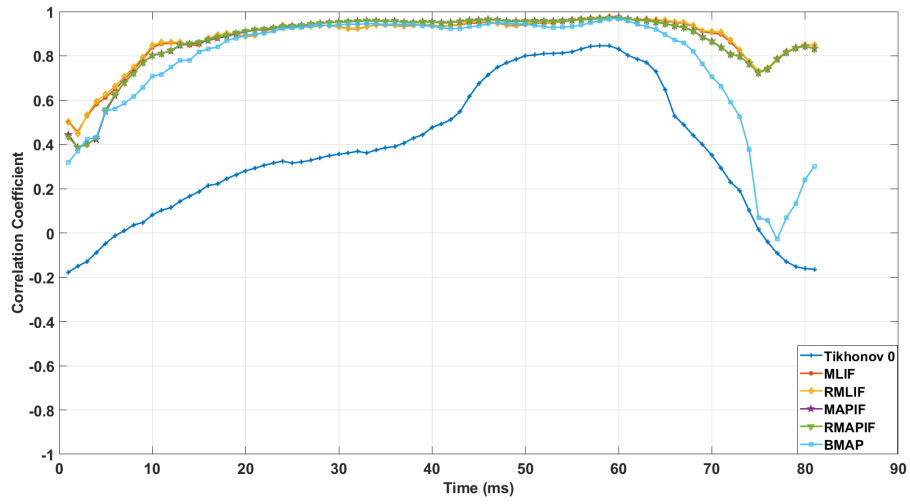
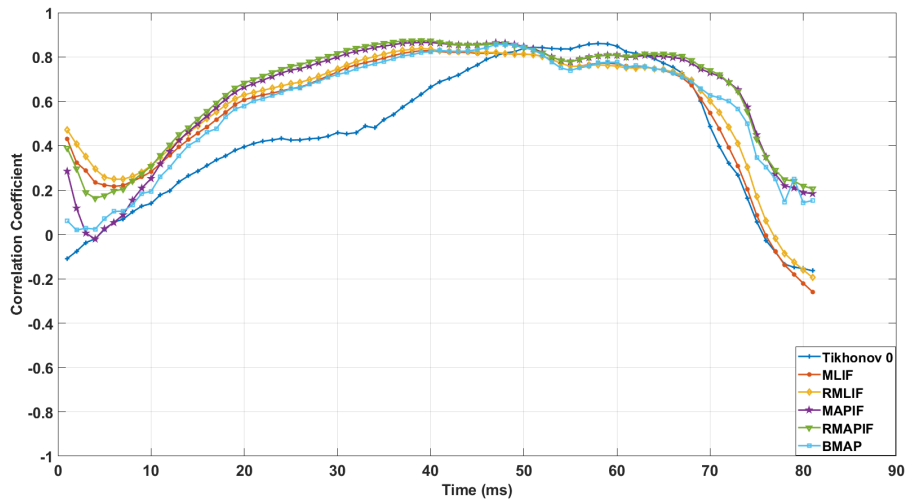(a) Correlation coefficient vs time plot for scenario 2 under 10 dB SNR
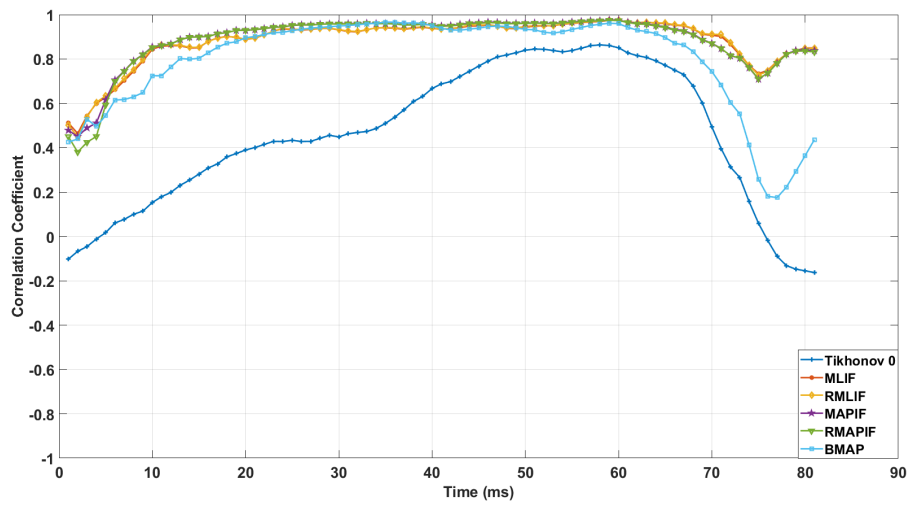
(b) Correlation coefficient vs time plot for scenario 2 under 15 dB SNR

Figure D.2: Correlation coefficient vs time plots for scenario 2

(a) Correlation coefficient vs time plot for scenario 3 under 10 dB SNR

(b) Correlation coefficient vs time plot for scenario 3 under 15 dB SNR

Figure D.3: Correlation coefficient vs time plots for scenario 3
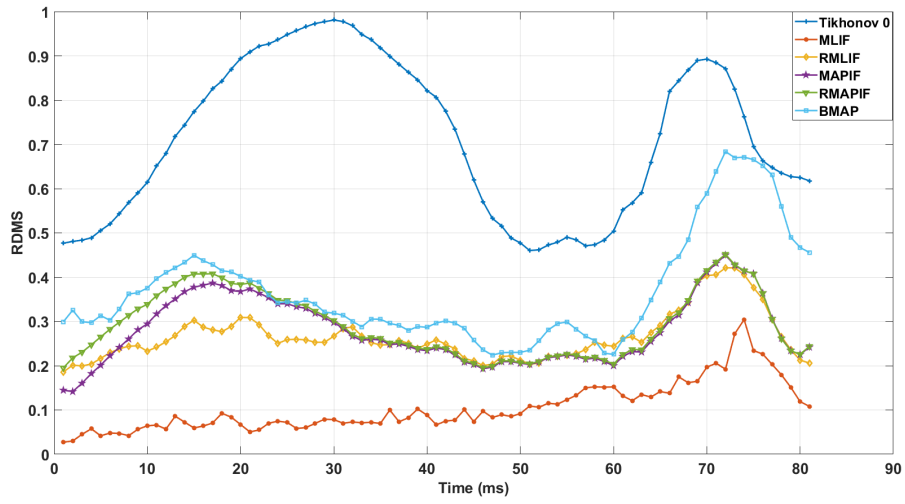
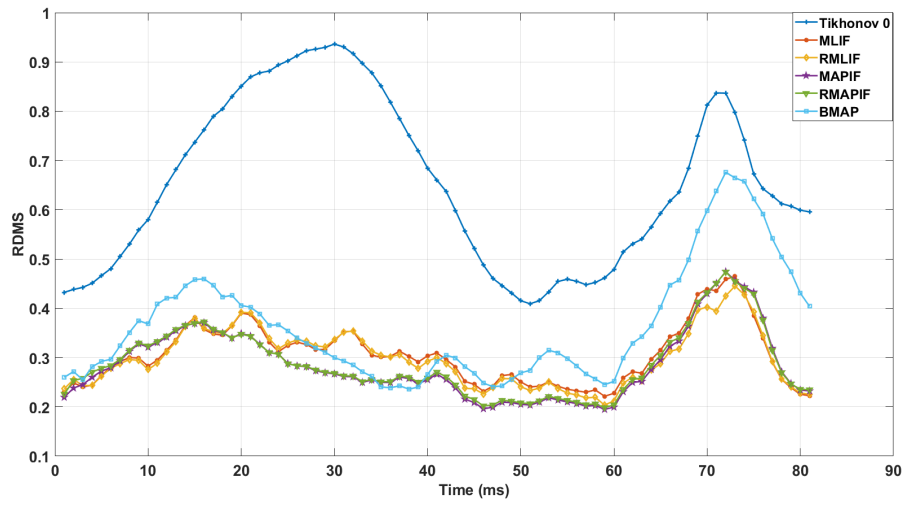(a) RDMS vs time plot for scenario 1 under 10 dB SNR
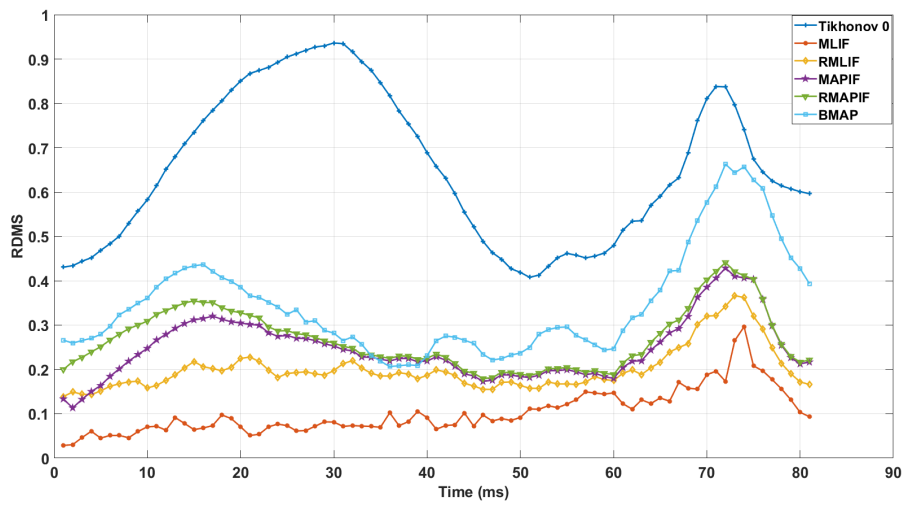
(b) RDMS vs time plot for scenario 1 under 15 dB SNR
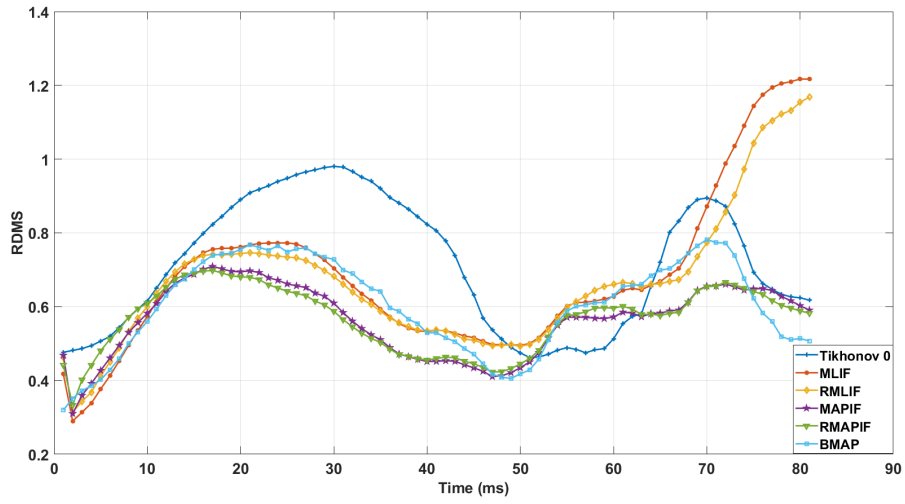
Figure D.4: RDMS vs time plots for scenario 1
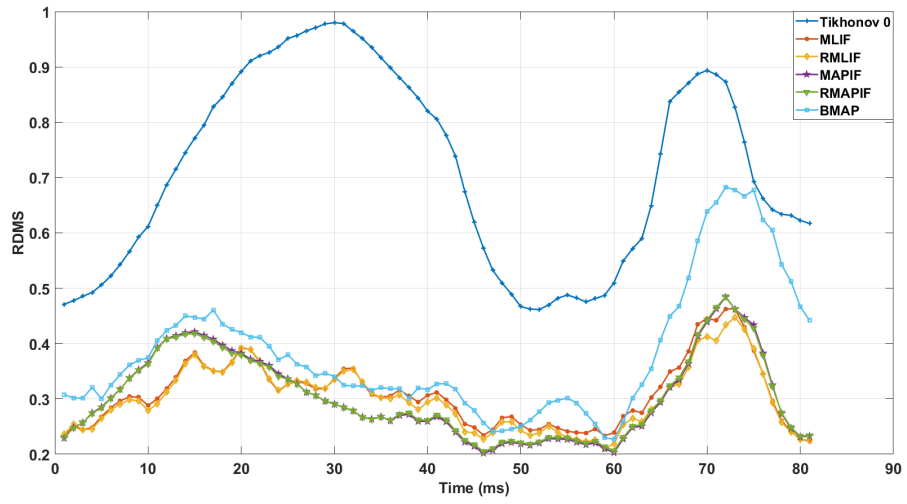
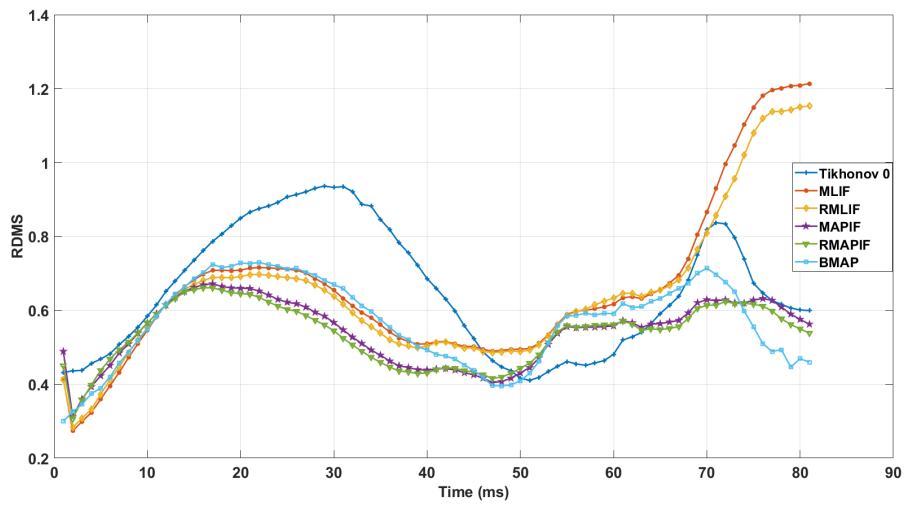(a) RDMS vs time plot for scenario 2 under 10 dB SNR

(b) RDMS vs time plot for scenario 2 under 15 dB SNR

Figure D.5: RDMS vs time plots for scenario 2

(a) RDMS vs time plot for scenario 3 under 10 dB SNR

(b) RDMS vs time plot for scenario 3 under 15 dB SNR

Figure D.6: RDMS vs time plots for scenario 3